

**ANALYSIS AND CHARACTERIZATION OF
HIGH-SPEED InGaAs/InP PIN PHOTODIODES**

Taner Döşl ođlu

B.S. Electrical Engineering,
and B.S. Physics
Bođaziđi University, Turkey, 1987

A dissertation submitted to the faculty of the
Oregon Graduate Institute of Science & Technology
in partial fulfillment of the requirements
for the degree of
Doctor of Philosophy
in
Electrical Engineering

April, 1992

This dissertation "Analysis and Characterization of High-Speed InGaAs/InP PIN Photodiodes" by Taner Döşlüoğlu has been examined and approved by the following Examination Committee:

Raj Solanki, Advisor
Associate Professor

V.S. Rao Gudimetla
Associate Professor

Reinhart Engelmann
Professor

H. Lee Van Nice
Tektronix, Inc.

ACKNOWLEDGEMENTS

I want to express my deepest thanks to my advisor, Dr. Raj Solanki for his encouragement and help. I have been able to focus on important aspects of the overall process due to his deep insight on all the topics of this dissertation research which extends to several fields of specialization.

I would like to thank to all the people in SSRL, Tektronix without whose help the fabrication of the devices would have been impossible. Special thanks to Dr. H. Lee Van Nice for his constant support during the fabrication of the devices and his helpful comments on this dissertation. I have received great help from Dr. Mihir Ravel in high-speed, Dr. Gary Goncher in electrical (DC), Steve Tabor in photoresponse measurements, and from Jeff Bacon in lithography. I would like to thank to Dr. Doug Jones for SIMS and XPS studies, Dr. Carolyn Drosd for Auger analysis, Bill Vetanen and Kurt Nordquist for metalization, and John Lyngdal for SEM micrographs.

I owe gratitude to Prof. John S. Blakemore, Dr. Dae Mann Kim, and Dr. Rao Gudimetla for what they have taught me and their interest in my research. I wish to thank Prof. Reinhart Engelmann for being my thesis committee member. Thanks also go to Dr. Uppili Sudarsan, Dr. Nyles Cody, Dr. John Abele, and Dr. Ravindra P. Joshi for their help in my research.

**I dedicate this dissertation
to my brother**

Table of Contents

ACKNOWLEDGEMENTS	iii
List of Tables	vii
List of Figures	viii
ABSTRACT	xi
1. INTRODUCTION	1
2. ORGANOMETALLIC VAPOR PHASE EPITAXY OF $\text{In}_{1-x}\text{Ga}_x\text{As}$	6
2.1 Introduction	6
2.2 Experimental	8
2.3 Gas Phase Reactions and Epilayer Composition	11
3. TRANSPORT PROPERTIES OF EPITAXIAL $\text{In}_{0.53}\text{Ga}_{0.47}\text{As}$	26
3.1 Introduction	26
3.2 Scattering Mechanisms	27
3.3 Characterization of InGaAs Epilayers	33
4. THE GENERALIZED STEADY STATE DIODE EQUATION: THE STATE EQUATIONS APPROACH	38
4.1 Introduction	38
4.2 Formulation of State Equations	40

4.3 Solution of State Equations	51
4.4 Computational	55
4.5 Conclusion	70
4.6 Appendix 4.1 List of Symbols	72
5. PIN DIODE AND THE STATE EQUATIONS FORMULATION	73
5.1 Introduction	73
5.2 Self-Consistent Solutions of Energy Bands and Carrier Distribution	74
5.3 Conclusion	86
6. FABRICATION AND CHARACTERIZATION OF PIN PHOTODIODES	87
6.1 Introduction	87
6.2 Experimental	89
6.3 Electrical DC Measurements	92
6.4 Spectral Response	103
6.5 High Speed Response	113
6.6 Conclusion	127
7. CONCLUSION	129
REFERENCES	133
VITA	147

List of Tables

2.1 Typical OMVPE growth parameters	10
2.2. Molar flows of the reactants	24
2.3. Measured and calculated x values in $\text{In}_{1-x}\text{Ga}_x\text{As}$	25
4.1. Material parameters of InGaAs and InP	57
6.1. Summary of device structures and DC measurements	93
6.2. Summary of responsivity and high speed measurements	115

List of Figures

2.1. TMI/TMG ratio versus the film composition x of $\text{In}_{1-x}\text{Ga}_x\text{As}$	13
2.2. Extent of depletion of group III precursors	20
2.3. Relative incorporation efficiency of In and Ga	21
3.1. Carrier concentration vs. temperature	32
3.2. Electron mobility vs. temperature (#46)	34
3.3. Electron mobility vs. temperature (#47)	35
4.1. Phase plot for the homojunction solutions	59
4.2 Calculated electric field: abrupt $p^+ - n$ InGaAs homojunction	60
4.3 Calculated band structure: abrupt $p^+ - n$ InGaAs homojunction	61
4.4 Calculated carrier concentrations: abrupt $p^+ - n$ InGaAs homojunction	62
4.5. Phase plot for the heterojunction solutions	64
4.6 Calculated electric field: abrupt $p^+ - n$ InP-InGaAs heterojunction	65
4.7 Calculated band structure: abrupt $p^+ - n$ InP-InGaAs heterojunction	66
4.8 Calculated carrier concentrations: $p^+ - n$ InP-InGaAs heterojunction	67
5.1. Band structure of InP/InGaAs/InP PIN grown with InP buffer	78
5.2. Band structure of InP/InGaAs/InP PIN grown without InP buffer	79
5.3. Calculated carrier concentration of PIN diode	80
5.4. Calculated electric field of PIN diode	81

5.5. Comparison of the capacitance-voltage measurements	84
6.1. Schematic diagram of PIN photodiode	94
6.2. Step response of the measurement setup	95
6.3. Dark current histograms of tile PIN-A	98
6.4. Dark current histograms of tile PIN-B	99
6.5. Dark current histograms of tile PIN-C	100
6.6. Dark current histograms of tile PIN-D	101
6.7. Dark current histograms of tile PIN-E	102
6.8. External responsivity of the photodiodes	105
6.9. Quantum efficiency surface of PIN-C-17 at 1300nm	106
6.10. Quantum efficiency surface of PIN-C-27 at 1300nm	107
6.11. Quantum efficiency surface of PIN-C-17 at 1550nm	108
6.12. Quantum efficiency surface of PIN-C-27 at 1550nm	109
6.13. Depletion width as a function of applied bias	112
6.14. Measured response of PIN-A-17 as a function of applied bias.	116
6.15. Measured response of PIN-B-17 as a function of applied bias.	117
6.16. Measured response of PIN-C-17 as a function of applied bias.	118
6.17. Sampling scope trace of the response of PIN-A-17	119
6.18. Measured and deconvolved response of PIN-A-17 at -5V	123

6.19. Measured and deconvolved response of PIN-A-17 at 0V	124
6.20. Calculated photoresponse of PIN-A-17	125
6.21. Occupancy factors of the conduction band valleys	128

ABSTRACT

ANALYSIS AND CHARACTERIZATION OF

HIGH-SPEED InGaAs/InP PIN PHOTODIODES

Taner Döşl ođlu, Ph.D.

Oregon Graduate Institute of Science and Technology, 1992

Supervising Professor: Raj Solanki

The fabrication of high-speed InGaAs/InP PIN photodiodes have been undertaken starting from the OMVPE epilayer growth all the way to the characterization of the fabricated devices. Various aspects of this complete process have been studied utilizing the mathematical tools of Linear Systems and Control Theory. Non-linearities in the incorporation efficiency of group III elements during the OMVPE growth due to gas phase reactions have been studied using a fourth order linear model and the results compared with the proposed chemical reactions. The role of various scattering mechanisms in determining the carrier concentration and mobility in the InGaAs layer is studied by the temperature dependence of Hall measurements.

One dimensional steady state diode equation is formulated as a five dimensional state equation using electric field, quasi-Fermi levels and the electron and hole currents

as the state variables. Self-consistent solutions have been obtained for the homojunction and the heterojunction case at thermal equilibrium using this formulation. This method is then used to calculate the electric field, carrier distribution and the band structure of the fabricated photodiodes at thermal equilibrium. The numerical solutions of two different PIN structures, one containing an undoped $0.1\mu\text{m}$ InP buffer layer and the other with InGaAs epilayer grown directly on top of the degenerate n^+ InP substrate are derived. InGaAs/InP PIN photodiodes have been fabricated with undoped InGaAs absorbing layers of thicknesses $0.2\mu\text{m}$, $0.5\mu\text{m}$, and $0.9\mu\text{m}$. The spectral response, and the impulse response of the devices having different absorbing layer thicknesses grown with and without an undoped InP buffer layer are compared.

CHAPTER 1

INTRODUCTION

Improvements in the speed of the optical fiber communications systems rely on the availability of high-speed low-noise lasers and photodetectors [1,2,3]. The focus of this research has been on fabrication of high-speed photoreceivers operating at 1300nm and 1550nm where the low-dispersion, low-loss windows appear in the transmission spectrum of optical fibers. $\text{In}_{0.53}\text{Ga}_{0.47}\text{As}$ (hereafter referred to as InGaAs) lattice-matched to InP is the most suitable material to be used in photodetectors at both 1300nm and 1550nm wavelengths due to its bandgap (0.75eV corresponding to 1650nm) and its high room temperature mobility [4]. Research in material growth and fabrication of InGaAs/InP based semiconductor devices has stemmed from the research on GaAs and has followed the same path during the initial development stages. However, as the technology developed, general research on III-V semiconductors has been divided into subcategories reflecting the unique properties and limitations of each alloy system. In GaAs reliable metal-semiconductor Schottky-barrier have been fabricated and the technology has been successfully applied to the large scale integrated MESFETs [5]. Early development of MESFET technology and extensive

characterization of this material[6] has been the driving force in the domination of GaAs in III-V device fabrication. The MESFET technology has also been successfully applied to the fabrication of metal-semiconductor-metal (MSM) photodiodes[7,8] which is an important step towards large scale integrated monolithic optoelectronic receivers [9] operating in the wavelength range of 400nm to 860nm.

Low barrier height of n-type InGaAs ($\approx 0.2\text{eV}$) [10], and the slow progress in the improvement of InP substrate quality, have hindered the attempts to duplicate the same technology in InGaAs/InP based optoelectronic receivers for longer wavelengths. Sufficient barrier height has been achieved on p-type InGaAs [11] and MSM photodetectors have been fabricated[12,13]. However, the transport properties are degraded due to p-type doping, and the high room temperature mobility is sacrificed in the process. Other efforts for enhancing the barrier height in InGaAs that has achieved some success include the use of Langmuir-Blodgett films exposed to an oxygen plasma in fabricating metal-insulator-semiconductor-insulator-metal (MISIM) photodetectors[14], and the application of photodeposited Cd[15]. Contrary to the developments in GaAs, performance of InGaAs/InP PIN photodetectors have surpassed the performance of MSM photodiodes as demonstrated in this work and reported in other publications [16,17,18]. Hence, the research on the development of integrated InGaAs/InP photoreceivers has concentrated in utilizing PIN structures. Improvements in the performance of advanced InGaAs/InP transistors are also very

encouraging. InGaAs/InP heterojunction bipolar transistors (HBTs) [19] and InAlAs/InGaAs high-electron mobility transistors (HEMTs) [20,21] have been fabricated with unity current gain cutoff frequencies (f_T) of 165GHz and 170GHz, respectively. However, the difficulties in the integration of these highly different device structures have slowed the development of high performance integrated photoreceivers operating at 1300nm and 1550nm. The complexity of integrating different structures monolithically have underlined the importance of studying all aspects of material growth and device fabrication as a whole.

The most important aspect of material growth that affects the performance of InGaAs/InP devices is the degree of lattice matching between the InP and $\text{In}_{1-x}\text{Ga}_x\text{As}$ determined by the GaAs fraction (x) in the solid solution. The measurement of lattice-parameter is best done non-destructively by x-ray double crystal diffraction (XRDCD) rocking curve analysis [22]. The non-destructive nature of XRDCD measurements is especially important in development of new device structures, where the epilayer quality in the final device structure can be determined before the lithographic processing. The advantages of characterizing the epilayers before electrical devices are fabricated are two fold. The first advantage is the ability to start the quality control process at the very beginning of production process. The quality control starts with the analysis of the substrates to be used in growth and is combined with the XRDCD data of the epilayers grown on these substrates. The second advantage is the information

obtained about the crystalline quality of the epilayers that form various parts of the semiconductor device. Development of satisfactory device models rely heavily on the accuracy of the values used for various material properties. In analyzing the measured device data and the validity of a given model, it is important to verify that the nominal values used in the model reflects the material properties of the grown epilayers. Determination of important material properties such as lattice distortion as a function of depth [23], interface grading [24], and background carrier concentration [25], from XRDCD measurements have been investigated utilizing the simulated results obtained from Takagi-Taupin formulation of dynamical theory of diffraction [26].

The various phases of technology development, namely material growth, material characterization, lithographic processing, measurement of the fabricated device properties, device modelling, and circuit integration pose significant challenges which require in depth studies and complicated solutions. Although the focus on each of these topics is essential, the interrelation between these fields of study is the key in integration of high performance devices based on III-V ternary alloys (i.e. InGaAs, InAlAs). The complexity of the relations between various parameters related to different phases of technology development demands the use of advanced mathematical tools in incorporating the physics that is involved. Important techniques like singular value decomposition, and Kalman filtering that are developed in signal processing and control theory can be utilized in incorporating non-linear functional relations and combining

various aspects of process modelling. Device models that can be used in simulating successfully integrated heterojunction devices with highly different structures have to be flexible in incorporating various aspects and formulations of material characterization.

In this thesis, key issues that have been studied during epilayer growth, material characterization, and device characterization of InGaAs/InP PIN photodiodes will be discussed, with special emphasis on the mathematical techniques used. In Chapter 2, a non-linear functional relation between the incorporation efficiency of group III elements in Organometallic Vapor Phase Epitaxy (OMVPE) of InGaAs lattice-matched to InP is discussed. In Chapter 3, the scattering mechanisms in two InGaAs epilayer films grown with and without an undoped InP buffer layer is compared. Due to the results of this study indicating improvements in the epilayer quality, the effects of incorporating a buffer layer has also been studied for the PIN structures and is discussed in Chapters 5 and 6. In Chapter 4, the state equations formulation of the one dimensional semiconductor equations is given, which allow the heterojunction to be easily incorporated into the solutions. In Chapter 5, the state equation formulation of the diode is employed for calculating the energy band profile and the carrier distribution in fabricated PIN structures. In Chapter 6, the performance of the fabricated PIN photodiodes that have different InGaAs absorbing layer thickness are compared and fundamental issues of device modelling are discussed.

CHAPTER 2

ORGANOMETALLIC VAPOR PHASE EPITAXY OF $\text{In}_{1-x}\text{Ga}_x\text{As}$

2.1 Introduction

Among the epilayer growth techniques used in III-V device fabrication OMVPE has been demonstrated to be most suitable technique for large scale manufacturing [27,28]. The composition of the epitaxial layer determines both the band gap and degree of lattice mismatch with respect to the substrate. Since the layer composition is critical in obtaining optimal device performance, establishing the relationship between the composition and the growth parameters is essential. We have examined this relationship for organometallic vapor phase epitaxy (OMVPE) of $\text{In}_{1-x}\text{Ga}_x\text{As}$ on InP and developed a simple model.

The control over the growth parameters is especially important when one grows lattice matched $\text{In}_{1-x}\text{Ga}_x\text{As}_{1-y}\text{P}_y$ epilayers with different x and y values in successive runs. The difficulty arises due to the differences in thermal properties of phosphine (PH_3) and arsine (AsH_3) [27]. AsH_3 decomposes at a lower temperature and hence the relationship between As and P incorporated in the epilayers and the partial pressures of AsH_3 and PH_3 is nonlinear as discussed in reference 27. Although not as severe as

in quaternary growth, a nonlinear relationship between the fraction of Ga in the film deposited and the gas phase precursor trimethylgallium (TMG) has been observed during $\text{In}_{1-x}\text{Ga}_x\text{As}$ growth [29,30]. This was thought to be due to side reactions between the hydrides and trimethylindium (TMI) and was minimized by modifying the reactor design and using newer indium sources.

The effects of growth temperature [31] and V/III ratio [32] on the electronic and optical properties of the $\text{In}_{1-x}\text{Ga}_x\text{As}$ layers have been reported. These studies have provided important information correlating properties of the epitaxial layers to the growth parameters. Our objective was to determine the relationship between flow rates and composition of the epilayers at different V/III ratios. We have correlated the gas flows to the epitaxial layer composition of $\text{In}_{1-x}\text{Ga}_x\text{As}$ and found the functional relation between x and the gas flows in a linear form. Using this functional relation we were able to routinely obtain lattice matching to better than 1.2×10^{-4} . This was achieved despite a severe depletion of TMI which manifests itself as high TMI/TMG ratio of 2.5 to obtain lattice matched $\text{In}_{1-x}\text{Ga}_x\text{As}$ where $x = 0.467$ (thermal decomposition temperature of TMI $\approx 270^\circ\text{C}$ and TMG $\approx 470^\circ\text{C}$).

2.2 Experimental

Lattice matched $\text{In}_{1-x}\text{Ga}_x\text{As}$ was grown on InP using a commercial horizontal, atmospheric pressure OMVPE reactor. The reactor chamber consists of a cylindrical quartz tube of diameter 5.5 cm, with a 4 cm \times 2.4 cm rectangular quartz tube inside it. A silicon carbide coated graphite susceptor (with an incline angle of 10°), sits about 40 cm. from the gas inlet. The total flow during InGaAs growth is 5.5 l/min. The linear velocity of the gasses are 9.5 cm/s, yielding a transit time of 4.2 s for the gasses to reach the susceptor. There is no cooling or heating of the quartz tubes. Prior to deposition, rectangular quartz tube and the susceptor are cleaned with aqua regia, rinsed with deionized water and dehydrated with methanol and ethanol, and loaded to the reactor and left overnight in the reactor with a continuous H_2 flow of $100\text{cm}^3/\text{min}$. Group III and group V sources used were TMG, TMI, and 10% AsH_3 and PH_3 in H_2 , and H_2 was the carrier gas for the organometallics. The TMG source cylinder was held at -15°C and TMI at 17°C . The substrates were etched with 1:1:5 $\text{H}_2\text{O}:\text{H}_2\text{O}_2:\text{H}_2\text{SO}_4$ bath for 5 min. at 40°C . After a thorough wash with deionized water for 5 min. the substrates were blown dry with nitrogen and immediately loaded into the reactor. The substrate temperature was raised to 700°C and maintained for 15 min under H_2 and PH_3 flow. After the preanneal, a $0.2\mu\text{m}$ thick undoped InP buffer layer was grown at 600°C . AsH_3 was introduced into the reactor and the flow stabilized, before PH_3 was turned off. Typical growth parameters are presented in Table 2.1. To calculate the

molar flow of organometallics, a saturated vapor pressure was assumed. The change in the weight of the organometallic bottles calculated using this assumption was consistent with the measured values.

The lattice mismatch between the epilayer and substrate were determined using an x-ray double crystal rocking curve diffractometer. A four crystal Si monochromator was used as the first crystal. The measurements were made with an x-ray spot size of $1 \times 3 \text{ mm}^2$.

The perpendicular and parallel lattice mismatch were calculated from asymmetric (115) and symmetric (004) reflections as described in [33]. Relaxed lattice mismatch was found using expression below and a Poisson's ratio ν of 0.36 [34].

$$\left(\frac{\Delta a}{a}\right)_{relax} = 0.47\left(\frac{\Delta a}{a}\right)_{\perp} + 0.53\left(\frac{\Delta a}{a}\right)_{\parallel} \quad (2-1)$$

The alloy composition was then obtained using the following expression [35].

$$\left(\frac{\Delta a}{a}\right)_{relax} = 0.03227 - 0.06907x \quad (2-2)$$

where x is the Ga fraction in $\text{In}_{1-x}\text{Ga}_x\text{As}$.

Table 2.1 Typical OMVPE growth parameters.

	InP	InGaAs
Growth Temp. (°C)	600	630
Growth rate ($\mu\text{m}/\text{min}$)	0.018	0.067
TMI (mol/min)	2.5×10^{-5}	2.5×10^{-5}
TMG (mol/min)	-	1.0×10^{-5}
PH_3 (mol/min)	2.0×10^{-5}	-
AsH_3 (mol/min)	-	1.2×10^{-3}
H_2 (l/min)	4	5

2.3 Gas Phase Reactions and Epilayer Composition

The OMVPE process is usually considered to be controlled by four fundamental aspects, (1) thermodynamics, (2) homogenous gas phase reactions, (3) mass transport and (4) surface kinetic processes [36]. The thermodynamic aspects of the OMVPE process, yielding information concerning the basic driving force for both the growth process itself and undesirable parasitic reactions occurring homogeneously in the vapor phase, has been extensively studied by several authors [36,37]. As pointed out the homogeneous gas phase reactions are important in the growth of indium containing compounds. After the group III alkyls and group V alkyls and/or hydrides are mixed, homogeneous gas phase reactions may occur to form additional compounds or adducts $(R_3III-VR'_3)$ which deposit on the reactor walls upstream from the substrate as a polymer $(RIII-VR')_n$ [36]. Recently a bimolecular alkyl elimination reaction has also been proposed to account for the loss of indium to the growth process in OMVPE growth of InGaAs on InP using TMG, TEI and AsH₃ [38]. Under commonly used conditions the growth rate of OMVPE is generally temperature independent and group III mass transport limited. The growth rate is controlled by the rate of arrival of growing species at the vapor-solid interface. It can be assumed that chemical equilibrium is established at the vapor-solid interface, because the rate of chemical reaction is considered sufficiently high compared to the arrival rate of the reactants. Hence, we treated the depletion of indium purely as a result of depletion of TMI in gas

phase and determined the significance of possible gas phase TMI elimination reactions.

A series of deposition runs were taken at different V/III ratios. The narrowest full width half maximum (FWHM) obtained from (004) reflection of a $3\mu\text{m}$ thick InGaAs film was 57 arcseconds. This sample had a lattice matching of better than 1.2×10^{-4} and the film was grown on a substrate with a FWHM of 20.5 arcseconds.

The Ga fraction in the film versus the TMI/TMG mole fraction ratio was first plotted as shown in Figure 2.1. Based on this data, the following functional relationship between x and the gas mole fractions was determined.

$$x = \frac{A}{\frac{\text{TMI}}{\text{TMG}} - B \times \text{AsH}_3} + C \times \text{TMG} + D \quad (2-3)$$

Our experimental results presented in Figure 2.1 show an inverse proportionality between x and TMI/TMG ratio. This is incorporated in the above equation as $x \propto 1 \div \text{TMI/TMG}$ with a proportionality constant A . At lower V/III ratios there was a decrease in the amount of TMI required to obtain lattice matching. This is most likely due to the prereaction between AsH_3 and TMI [29]. To account for this we included a first order correction factor as $B \times \text{AsH}_3$. The minus sign is chosen to indicate depletion with B being positive. When the TMG flow rates were raised there was a shift towards gallium rich composition. This is taken into consideration by including the term

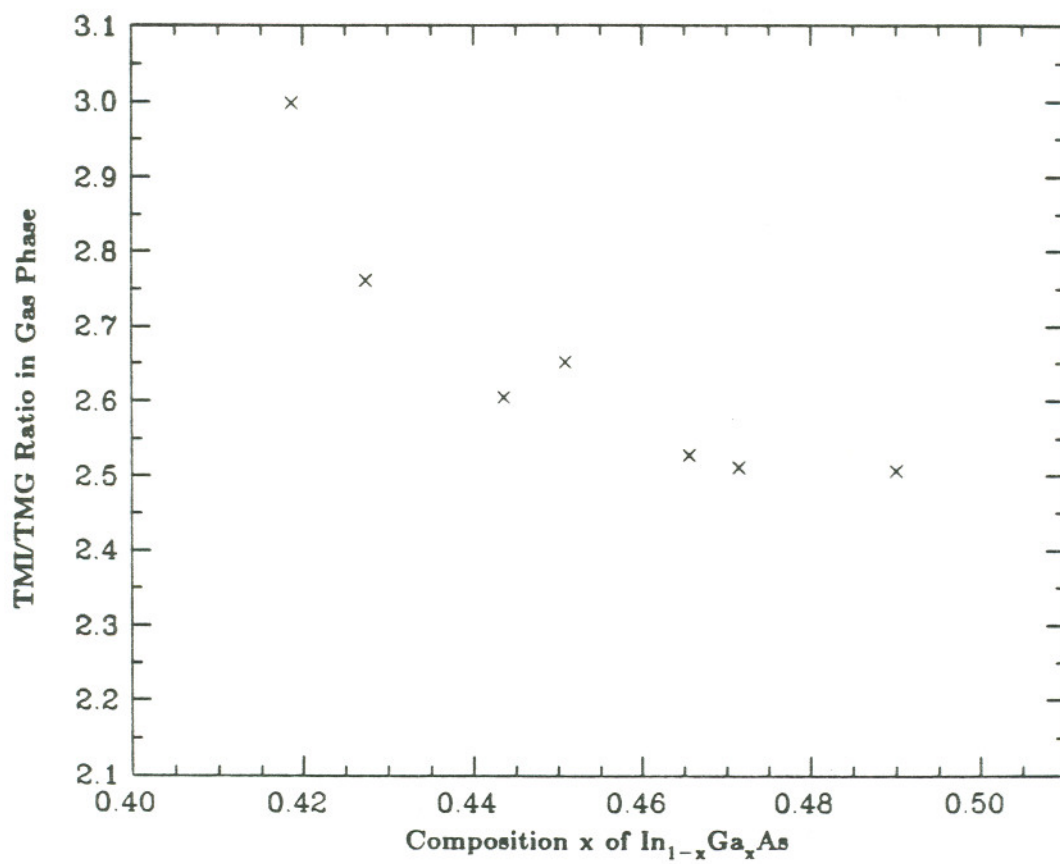


Figure 2.1. TMI/TMG ratio versus the film composition x of $\text{In}_{1-x}\text{Ga}_x\text{As}$.

$C \times TMG$. Since we are interested in the region near lattice matching we did not impose the restriction of $x \rightarrow 0$ as $TMG \rightarrow 0$. The constant D was included to compensate for higher order effects.

In the present analysis our objective was to use all the available data points and at the same time create a model where the least number of coefficients are utilized. In order to calculate the above parameters we required at least 4 data points. Since this model is based on empirical relationship more than 4 data points were used to statistically average out the error. To simplify the computation it was desirable to have a linear model. With a linear model the best estimate for the solution using Prony's method [39] was found by simply taking the pseudo inverse and solving the equation. This allowed us to use a large number of data points in finding the best estimate of the coefficients A to D .

We can rewrite eqn. 2.3 in a linear form as

$$x = \frac{B \times x \times AsH_3 \times TMG}{TMI} + C \times TMG \times \left(1 - \frac{B' \times AsH_3 \times TMG}{TMI}\right) \quad (2-4)$$

$$+ D \times \left(1 - \frac{B' \times AsH_3 \times TMG}{TMI}\right) + \frac{A \times TMG}{TMI}$$

In matrix notation this can be written as

$$x = Mw \quad (2-5)$$

where x is the vector formed by the x values calculated from (2-2), M is the matrix formed by the combination of the mole fractions as described in (2-4) and w is the vector containing the coefficients A to D . Using Prony's method and iteratively replacing B' with B we find the best estimate for the coefficients A,B,C and D yielding the minimum mean square error (MSE). This was obtained by taking the pseudo inverse of the matrix M and solving the linear simultaneous equations as below

$$w = (M^T M)^{-1} M^T x \quad (2-6)$$

where M^T is the transpose of the matrix M . The coefficients A to D of eqn. (2.4) calculated using (2-6) are $A=0.3468$, $B=197.3$ min/mol, $C=26550$ min/mol and $D=6.74 \times 10^{-2}$. Using these coefficients the mean square error (MSE) between the calculated and the given x values was found to be 6.85×10^{-5} .

Once the coefficients A,B,C and D are found it is simple to manipulate eqn. 2.3. One application of this model was the determination of the gas flows to grow lattice matched epilayers with different V/III ratios. The procedure used was as follows. First a convenient TMG flow rate was chosen. Then we determined the AsH_3 flow for the desired V/III ratio ($TMI \approx 2.5 \times TMG$). For fine tuning the TMI flow rate we rewrote eqn. 2.3 as

$$TMI = \frac{TMG}{x}(A+B \times x \times AsH_3 + C \times TMG + D) \quad (2-7)$$

TMI was used for fine tuning because its flow was in the mid scale of the mass flow controller (MFC), hence we could adjust the flow within 0.3% of the total TMI flow (better than the accuracy of the MFC which is 0.5%).

The prereaction between TEI and AsH₃ in atmospheric pressure OMVPE reactors has been previously investigated [40,41] and a model developed assuming a depletion reaction which is represented by

$$\frac{dp_{TEI}}{dt} = -K_1 p_{TEI(t)} p_{AsH_3} \quad (2-8)$$

where p_{TEI} and p_{AsH_3} are the partial pressures of TEI and AsH₃. Solving $p_{TEI(t)}$ in terms of the reactant partial pressures at the inlet of the reactor, it was shown that the ratio of In to Ga in the solid can be expressed in terms of partial pressures of the gases as given by equation (2.9).

$$\frac{1-x}{x} = K_2 \frac{P^{\circ}_{TEI}}{P^{\circ}_{TEG}} \frac{1 - \frac{P^{\circ}_{TEI}}{P^{\circ}_{AsH_3}}}{e^{[K_1(P^{\circ}_{AsH_3} - P^{\circ}_{TEI})] - \frac{P^{\circ}_{TEI}}{P^{\circ}_{AsH_3}}}} \quad (2-9)$$

where K_1 is a phenomenological constant which characterizes the rate constant of the prereaction and K_2 is the proportionality constant describing the relative transport and incorporation efficiency of In and Ga into the solid ternary compound. Using the above expression, with proper substitutions of TMI and TMG instead of TEI and TEG for our case, we calculated the coefficients K_1 and K_2 . The best fit of eqn. (2.9) to our data yielded $MSE_{\min} = 4.35 \times 10^{-4}$ between the calculated values and the data, with the parameters $K_1 = 28300 \text{ atm}^{-1}$, $K_2 = 0.460$.

We examined a two parameter linear model assuming the prereaction to be proportional to the AsH_3 partial pressure at the inlet of the reactor tube ($P^{\circ}_{AsH_3}$). In linear form this corresponds to

$$\frac{(1-x)}{x} = K_2 \frac{P^{\circ}_{TMI}}{P^{\circ}_{TMG}} [1 - K_1 P^{\circ}_{AsH_3}] \quad (2-10)$$

Using eqn. (2.6) we calculated the coefficients to be $K_1 = 24600^{-1} \text{ atm}^{-1}$, $K_2 = 0.513$.

These coefficients in eqn. 2.10 yielded a $MSE = 4.35 \times 10^{-4}$ between the given and calculated x values. The coefficients K_1 , K_2 and MSE are similar for both the two parameter models. This is due to the fact that both the models have the same number of independent coefficients to yield the best fit to the data. It is essential to define the coefficients based on the kinetic analysis of the homogeneous reaction. However, for the purpose of obtaining a curve fit to the data and using the model to calculate the required gas flows, the linear model seems more suitable. It can easily be manipulated whereas it is not obvious to find an explicit relation for TMI in terms of x , TMG and AsH_3 from equation (2.9).

We also examined the possibility of a bimolecular alkyl elimination reaction similar to that of TEI [15]. The bimolecular reaction for decomposition of the alkyl to a polymer is given as,

$$\frac{dp_{add}}{dt} = -k(P_{add})^2 \quad (2-11)$$

$$k = Ae^{-\left(\frac{E_a}{k_b T}\right)} \quad (2-12)$$

where P_{add} is the adduct partial pressure and is proportional to the TMI partial pressure and k is the reaction rate constant. The reaction rate constant k is expressed in eqn. (2.12) in terms of the Arrhenius equation. A is normally referred to as the

pre-exponential factor and E_a is the activation energy of the process. With all other factors constant, the amount of indium species lost to depletion will be proportional to the square of the inlet partial pressure. Hence, for low indium partial pressures an upper limit of depletion is given by Agnello and Gandhi [38] as

$$\Delta \frac{(1-x)}{x} = \left(\frac{D_{TMI}}{D_{TMG}} \right)^{1/2} K_2 \frac{(P_{TMI})^2}{P_{TMG}} \quad (2-13)$$

The ratio of diffusion coefficients D_{TMI} to D_{TMG} can be taken as unity for a first order approximation. The extent of depletion in the solid as a function of the square of the TMI pressure is plotted in Figure 2.2 for four different TMG flows. The data can be approximated by a straight line. However, the decrease in the depletion of indium with decreasing TMG partial pressure is also apparent as we indicated earlier.

The equilibrium constant K_2 can be written in terms of forward and reverse reaction rate constants as

$$K_2 = \frac{k_f}{k_r} \quad (2-14)$$

The Gibbs free energy of the reaction can then be calculated in terms of the equilibrium constant by equation 2-15

$$K_2 = e^{\frac{\Delta G}{kT}} \quad (2-15)$$

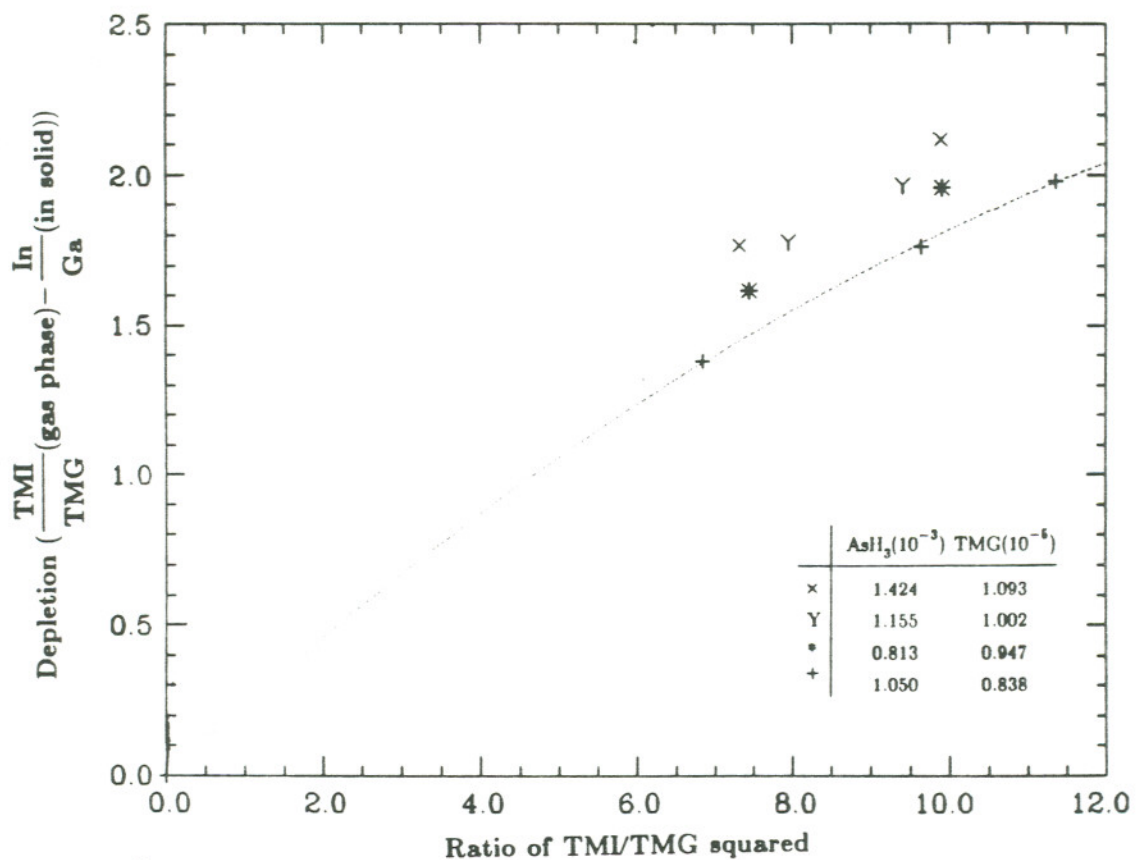


Figure 2.2. Extent of depletion of group III precursors $\Delta[(1-x)/x]$, as a function of the square of the ratio of TMI to TMG in gas phase.

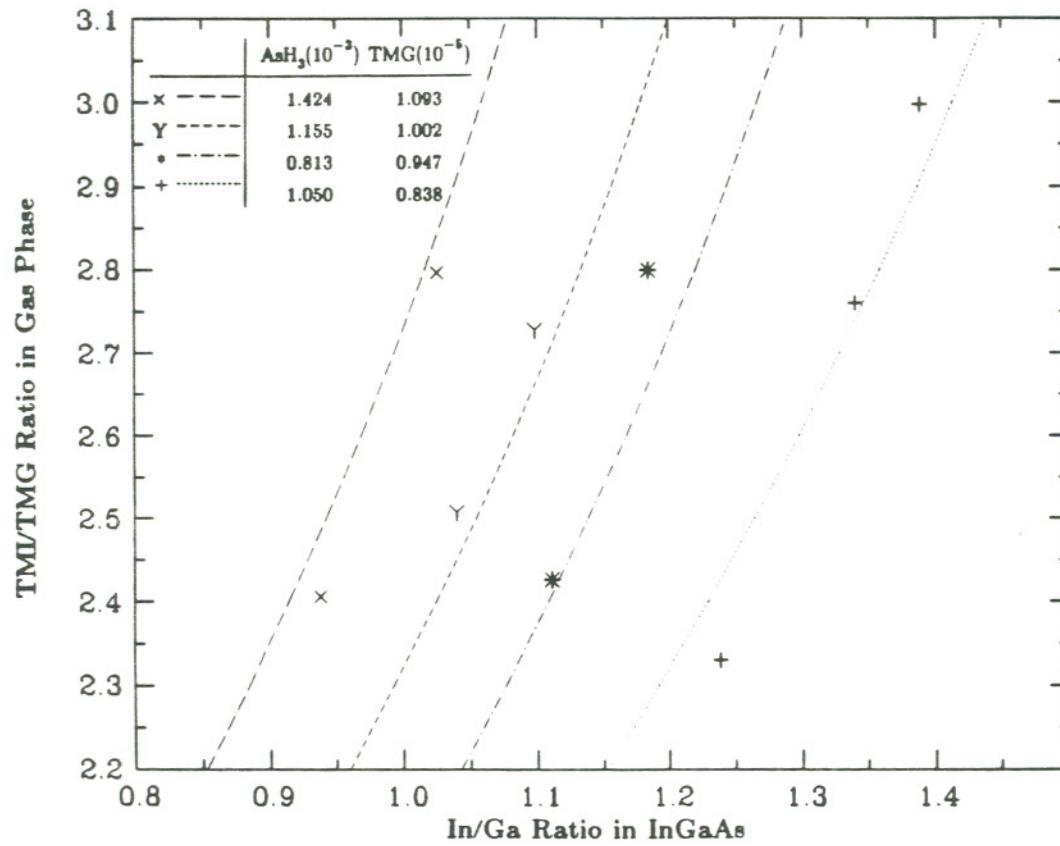


Figure 2.3. Relative incorporation efficiency of In and Ga. Ratio of TMI/TMG in gas phase versus In/Ga ratio in the epilayers. Curves were obtained using the 4 parameter model. Individual points are the experimental values.

The bimolecular alkyl elimination depletion reaction of indium can also be written in linear form in terms of the partial pressure of the reactants at the inlet of the reactor tube as,

$$\frac{(1-x)}{x} = A \times \frac{P^{\circ}_{TMI}}{P^{\circ}_{TMG}} (1 + B \times P^{\circ}_{TMI}) \quad (2-16)$$

Using eqn. (2-16) we calculated the coefficients $A=0.512$ and $B=-1.90 \times 10^6 \text{ atm}^{-1}$ with a $\text{MSE}=4.69 \times 10^{-4}$. The coefficient B in eqn. (2.17) and K_1 in eqn. (2.10) represent the equilibrium constant and can be used in calculating the Gibbs free energy (ΔG) of the assumed reactions. We obtained $\Delta G_{\text{TMI-TMI}}=-8.6 \text{ kcal/mole}$ and $\Delta G_{\text{TMI-AsH}_3}=-6 \text{ kcal/mole}$. The gas phase depletion of TMI can also be represented in a 3 parameter linear model as a combination of both the bimolecular alkyl elimination reaction and adduct formation as

$$\frac{(1-x)}{x} = A \times \frac{P^{\circ}_{TMI}}{P^{\circ}_{TMG}} (1 + B \times P^{\circ}_{TMI} + C \times P^{\circ}_{\text{AsH}_3}) \quad (2-17)$$

The coefficients that give the minimum MSE using eqn. (2-17) are calculated to be $A=0.501$, $B=-1.75 \times 10^4 \text{ atm}^{-1}$, $C=-9.92 \times 10^5 \text{ atm}^{-1}$ with a $\text{MSE}=4.25 \times 10^{-4}$.

The gas phase depletion of TMI we have observed in our data may be a result

of either bimolecular alkyl elimination reaction of TMI molecule or the prereaction between TMI and AsH_3 . The MSE obtained by fitting eqn. (2.10) and eqn. (2.16) are very similar and a better fit is obtained when both the reactions are taken into account in eqn. (2.17). The empirical relation given in eqn. (2.3) still yields an order of magnitude lower MSE between the measured and calculated values. In Figure 2.3 we have plotted the TMI/TMG ratio versus x for various TMG and AsH_3 flows calculated using our 4 parameter empirical model as well as experimental data. There is a strong relation between the TMG molar flow and the change in the TMI/TMG ratio required to obtain lattice matching. In the 4 parameter model, coefficient C determines the first order correction due to changes in the TMG molar flow. In Figure 2.3 the shift in the data points due to change in the TMG molar flow is in agreement with the curves drawn for the same conditions using eqn. (2.3). The molar flows of the reactants at the inlet of the reactor chamber are given in Table 2.2. The corresponding x values (Ga fraction in the solid) for these conditions using all the models considered are given in Table 2.3. The empirical model with 4 parameters yielded the best fit to the data. We have utilized this model to obtain lattice matching with as few runs as possible and make better predictions for the runs to follow.

Table 2.2. Molar flows of the reactants.

#	Molar Flows (mole/min)		
	TMG(10^{-5})	TMI(10^{-5})	AsH ₃ (10^{-3})
1	1.002	2.511	1.155
2	0.8377	2.511	1.082
3	0.8377	2.313	1.021
4	0.9105	2.371	1.131
5	0.9469	2.511	1.155
6	0.9469	2.379	1.155
7	0.9469	2.394	1.155
8	0.9469	2.143	0.407
9	0.9469	2.143	0.610
10	0.9469	1.988	0.610
11	0.9469	2.401	1.159
12*	0.9469	2.438	1.163
13	0.9469	2.298	0.813
14	1.093	3.056	1.424
15	1.002	2.732	1.159
16	0.8377	1.952	1.049
17	0.9469	2.651	0.813
18	1.093	2.629	1.428

* Optimum lattice-matching condition.

Table 2.3. Measured and calculated x values in $\text{In}_{1-x}\text{Ga}_x\text{As}$.

	Expt. x	Calculated x values			
#		4 Coeff. Model	2 Coeff. Model(AsH_3) & Model from [17]	2 Coeff. Model(TMI)	3 Coeff. Model
1	0.4901	0.4859	0.4783	0.4789	0.4805
2	0.4186	0.4147	0.4313	0.4349	0.4343
3	0.4274	0.4255	0.4497	0.4469	0.4503
4	0.4436	0.4538	0.4681	0.4653	0.4684
5	0.4509	0.4610	0.4643	0.4649	0.4666
6	0.4714	0.4707	0.4780	0.4744	0.4782
7	0.4656	0.4693	0.4764	0.4733	0.4768
8	0.4554	0.4769	0.4772	0.4963	0.4812
9	0.4956	0.4815	0.4845	0.4955	0.4866
10	0.5065	0.4948	0.5033	0.5095	0.5030
11	0.4778	0.4700	0.4758	0.4728	0.4763
12	0.4672	0.4668	0.4642	0.4565	0.4601
13	0.4737	0.4720	0.4688	0.4688	0.4658
14	0.4937	0.4952	0.4506	0.4498	0.4520
15	0.4765	0.4725	0.4494	0.4491	0.4490
16	0.4469	0.4526	0.4861	0.4702	0.4769
17	0.4569	0.4506	0.4332	0.4418	0.4345
18	0.5160	0.5202	0.4886	0.4770	0.4846

CHAPTER 3

TRANSPORT PROPERTIES OF EPITAXIAL $\text{In}_{0.53}\text{Ga}_{0.47}\text{As}$

3.1 Introduction

The performance of semiconductor electronic devices depends heavily on low and high-field electron transport properties of the materials in which they are fabricated. In alloy semiconductors there are several scattering mechanisms, such as alloy scattering that play an important role in determination of carrier transport [42,43]. Important material parameters, including the degree of alloy scattering and ionized donor and acceptor concentrations, can be obtained from the measurements of the temperature dependence of mobility. These parameters can then be used in electron transport calculations by either the iterative [44] or the Monte Carlo technique [45,46] to predict the device parameters [47].

To compare the effects of various scattering mechanisms on the mobility over a given temperature range, Mathiessen's rule can be used to combine the mobility limits imposed by different scattering mechanisms. Although some error is involved [44] in using Mathiessen's rule, we have chosen this simple analytical technique since it allows clear graphical displays of the mobility associated with each individual scattering

mechanism. This technique is used to examine the scattering mechanisms in samples of different material parameters. In our calculations we have considered optical phonon [48,49], alloy disorder scattering [42,43], and Brooks-Herring formulation of ionized impurity scattering [50] as the major scattering mechanisms affecting the mobility in the temperature range of 40K to 300K. Another scattering mechanism that has been incorporated in our mobility calculations, together with the alloy disorder scattering, is space charge scattering [51]. Space charge scattering is due to the large regions of space charge caused by the inhomogeneity in ternary and quaternary alloys, and has $T^{-1/2}$ temperature dependence: the same as in alloy disorder scattering, but with a different proportionality upon the electron effective mass. For our calculations, we have chosen not to make separate explicit allowances for other less significant scattering mechanisms such as piezoelectric [52], deformation potential [53] and neutral impurity scattering[54].

3.2 Scattering Mechanisms

The mobility limit imposed by various scattering mechanisms can be determined from the temperature dependence of mobility. It is important to determine the degree of alloy disorder and ionized-impurity scattering to correctly estimate the purity of the InGaAs epilayers. The temperature dependent free carrier concentration must be analyzed in conjunction with the ionized-impurity scattering to determine the role of

acceptor compensation versus the alloy disorder scattering in these materials in studying the difference of 77K mobility among different samples. The limit imposed on the mobility of electrons by various scattering mechanisms were calculated as described below.

The contribution of polar optical phonon scattering was calculated using the expression below [48,49,4]

$$\mu_{PO} = 2.6 \times 10^{51} \left(\frac{T}{300} \right)^{1/2} \left(\frac{e}{e^*} \right)^2 \left(\frac{m_o}{m^*} \right)^{3/2} M \Omega \theta (e^z - 1) G(z) \quad (3-1)$$

where the mobility limit μ_{PO} is in square centimeters per volt-second, e^* is the Callan effective charge, M is the reduced mass of the cell in kilograms, Ω is the volume of the primitive cell, θ is the polar phonon temperature, and z is θ/T , where T is the absolute temperature in kelvin. The parameter values for GaAs and InAs are taken from [4]. Linear interpolation is used in determining the parameter values for InGaAs. $G(z)$ is the screening factor given by [48,49]. We have used the numerical values of $G(z)$ given in [49] in our calculations with a fourth order interpolation for the points in between. The value of the electron effective mass m^* was taken from [55].

The limit imposed on the mobility by ionized-impurity scattering (μ_{II}) was calculated according to Brooks-Herring formula as below [50];

$$\mu_H = 3.28 \times 10^{15} \frac{k_s^2 T^{3/2}}{\left(\frac{m^*}{m_o}\right)^{1/2} N_i} \left(\ln(1+b) - \frac{b}{1+b}\right)^{-1} \quad (3-2)$$

where

$$b = \frac{1.29 \times 10^{14} k_s m^* T^2}{m_o n}$$

and

$$N_i = n + N_A$$

where n is the electron density from the Hall measurements, k_s is the static dielectric constant and N_D and N_A are the density of donors and acceptors, respectively. The donor and acceptor concentrations were estimated from the free carrier concentration data plotted in figure 3.1. Two different types of donor flaws contribute to the free electron concentration (n_o) in the temperature range considered as can be seen from the data. In the case of two donor flaws with effective compensating flaws of density N_A , the free electron concentration can be written as [56]

$$n_o = N_{d1}[1 - P_e(E_{d1})] + N_{d2}[1 - P_e(E_{d2})] - N_A \quad (3-3)$$

where

$$P_e(E_d) = \frac{1}{1 + \beta e^{\left[\frac{E_d - E_F}{k_o T}\right]}}$$

$P_e(E_d)$ is the occupancy factor of the donor flaw with ionization energy E_d , β is the spin degeneracy weighting factor, N_{d1} and N_{d2} are the concentrations of the donor flaws with ionization energies E_{d1} and E_{d2} . For a semiconductor with relatively strong compensation of primary flaws the free electron concentration can be written for each donor flaw as [56]

$$n_o \approx \frac{(N_d - N_a)}{1 + \left(\frac{N_a}{\beta N_c}\right) e^{\left(\frac{E_d}{k_o T}\right)}} \quad (3-4)$$

The asymptotic lines in figure 3.1 were obtained using eqn. 3-4 using donor flaw densities discussed in section 3.3.

Two scattering mechanisms that are important in the temperature range considered are the space charge scattering and alloy disorder scattering. We used these scattering mechanisms to determine the degree of inhomogeneity and disorder in the epilayers. Both the scattering mechanisms have the same temperature dependence,

hence it is not possible to isolate the effect of alloy disorder scattering from the temperature dependence of the electron mobility. However, the degree of alloy scattering can be determined by high pressure measurements due to the difference in effective mass dependence. We calculated the limit imposed on the mobility by the space charge scattering (μ_{SC}) [51] and the alloy disorder scattering (μ_{AL}) [42,43] using equation 3.5 and 3.6 respectively, as described in [4]. Thus,

$$\mu_{SC} = \frac{10^4 e}{\sqrt{2} N_s A k^{1/2}} m^{*-1/2} T^{-1/2} \quad (3-5)$$

where N_s is the density of space charge scattering regions, A is their effective scattering cross-sectional area, k is the Boltzmann constant, and m^* is the effective mass of the conduction band electron. For comparison,

$$\mu_{AL} = \frac{8 \times 10^4 \sqrt{2} h^4}{3 \pi \Omega e k^{1/2} S(\alpha) (\Delta U)^2} m^{*-5/2} T^{-1/2} \quad (3-6)$$

where $S(\alpha)$ refers to the degree of randomness, being unity when there is total disorder. ΔU is called the alloy scattering potential and is a measure of the magnitude of the fluctuations caused by the atomic distribution variations, and Ω is the volume of the primitive cell.

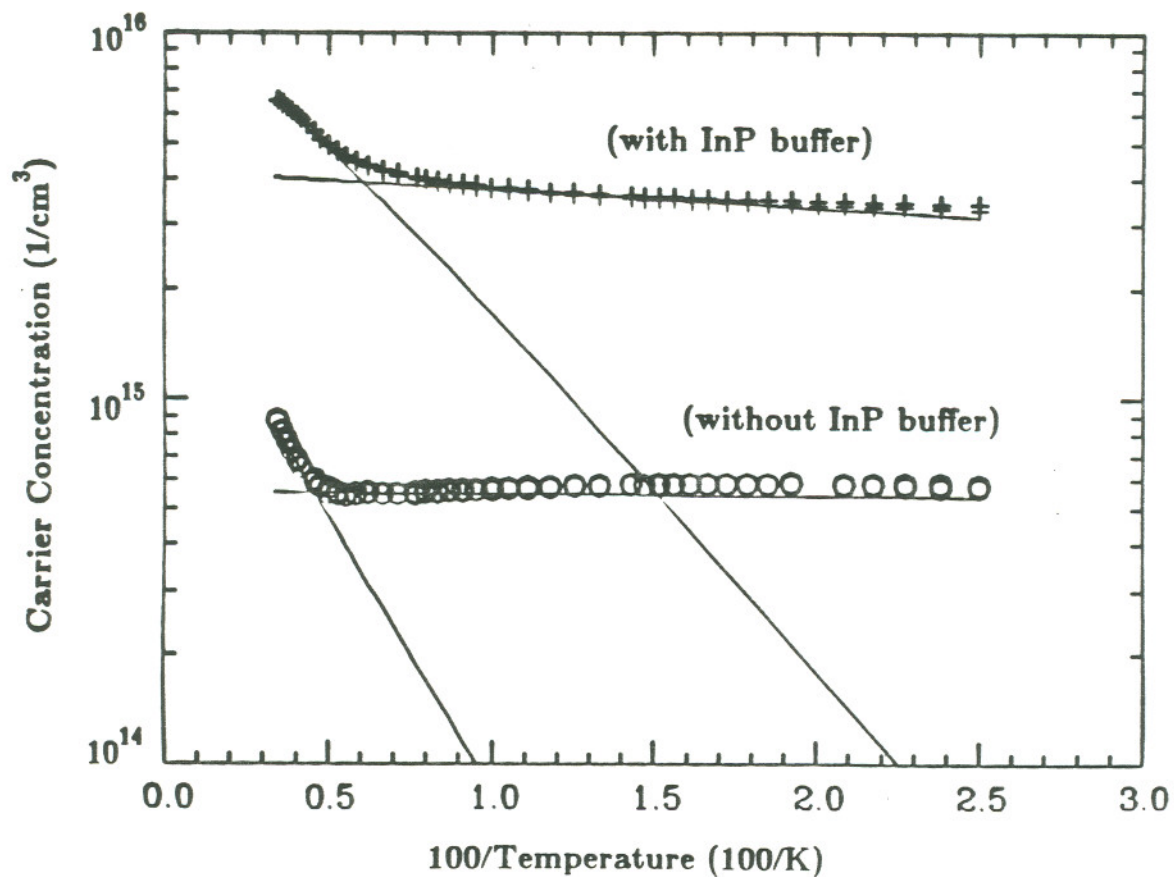


Figure 3.1. Carrier concentration vs. temperature for the InGaAs epilayers grown with (type A) and without (type B) InP buffer layer. The asymptotic lines are drawn using eqn. 3.4. Each curve represents data with magnetic fields of 3 and 5 kG.

3.3 Characterization of InGaAs Epilayers

The InGaAs epilayers were grown in an atmospheric pressure organometallic vapor phase epitaxy (OMVPE) reactor as described in Chapter 2. The substrates were (100)-oriented Fe-doped semi-insulating (SI) InP. Two types of undoped InGaAs epilayer samples were prepared. In type A samples, an undoped $0.2\mu\text{m}$ thick InP buffer layer was grown between the InGaAs epilayer and the InP substrate. In type B samples, the undoped InGaAs epilayer was grown directly on the InP substrate. The van der Pauw method was used for Hall measurements at 3kG and 5kG magnetic field, over the temperature range 40K to 300K.

The mobility limits imposed by various scattering mechanisms combined by using Mathiessen's rule, and the experimentally measured mobility, are plotted in figures 3.2 and 3.3, for InGaAs samples #46 and #47 respectively. Sample #46 is representative of InGaAs samples grown on an InP buffer layer (type A), and sample #47 is a representative sample without any buffer layer (type B). Both the samples are lattice matched to InP to better than 5×10^{-4} as determined by X-ray double crystal rocking curve analysis. The full width at half maximum (FWHM) of the symmetrical (004) reflection of both samples were also similar. The carrier concentration is dictated by the shallow donor flaw up to 200K for both samples. The slope indicates (see Figure 3.1) an ionization energy of 1 meV for sample #46 and 0.15meV for sample #47 with concentrations $1 \times 10^{16} \text{ cm}^{-3}$ and $8 \times 10^{15} \text{ cm}^{-3}$, respectively. These very low activation

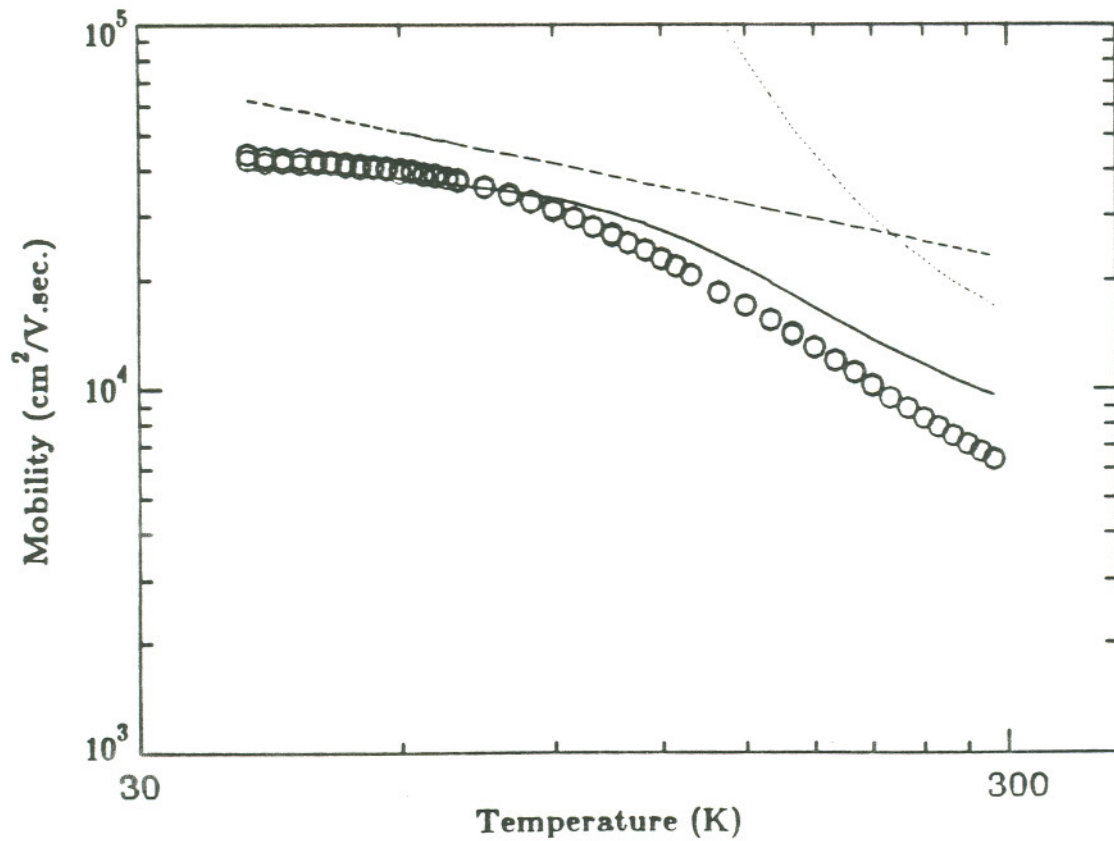


Figure 3.2. Electron mobility vs. temperature (#46) for a typical InGaAs epilayer grown with $0.2\mu\text{m}$ InP buffer layer. The limits imposed on the mobility by alloy disorder (dashed line) and optical phonon scattering (dotted line) are drawn as asymptotic lines, together with the combined mobility calculated using Mathiessen's rule. Ionized impurity scattering is not significant for this sample.

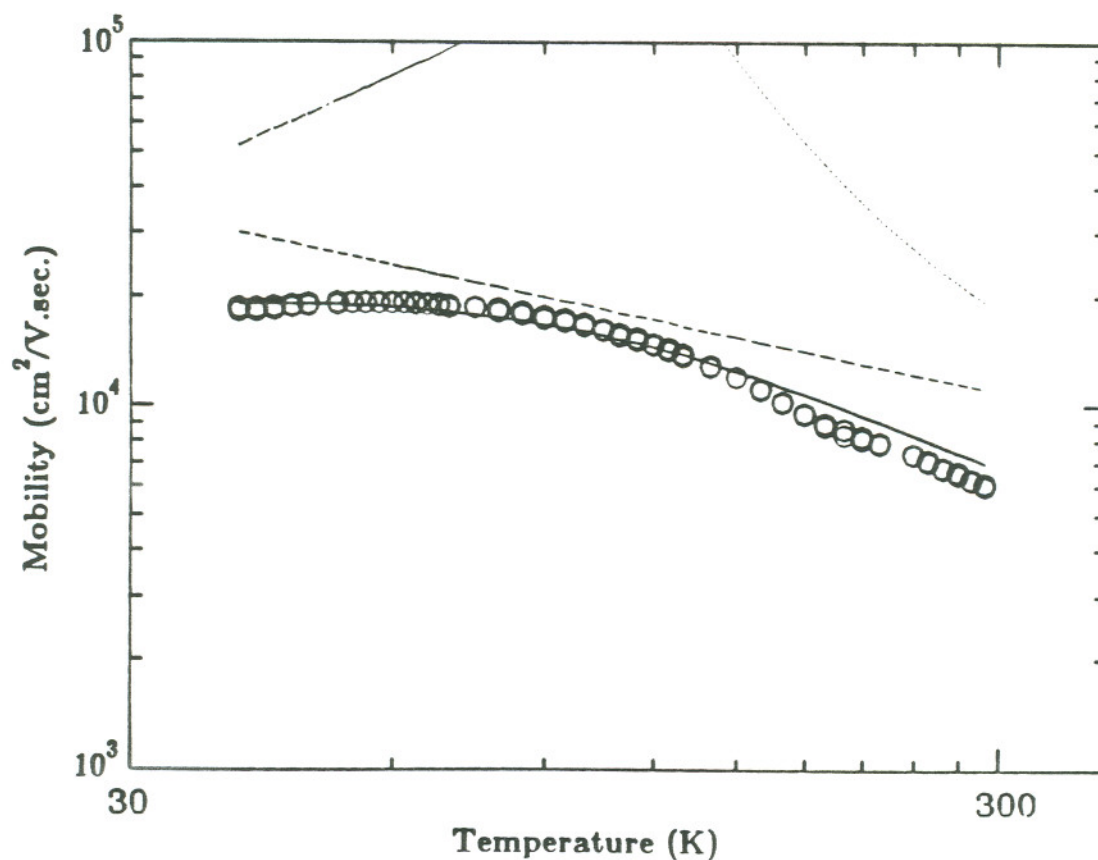


Figure 3.3. Electron mobility vs. temperature (#47) for a typical InGaAs epilayer grown without the InP buffer layer. The limit imposed on the mobility by ionized-impurity (dashed-dotted line), alloy disorder (dashed line) and optical phonon scattering (dotted line) are drawn as asymptotic lines, together with the combined mobility calculated using Mathiessen's rule.

energies show that, as expected, the shallow donor states have been appreciably broadened by impurity banding [56].

At higher temperatures a deeper level donor with a concentration of $3 \times 10^{16} \text{ cm}^{-3}$ becomes dominant. The ionization energy of the deeper level donor is 20 meV and 30 meV for samples #46 and #47, respectively. We used the same compensating acceptor concentration in the whole temperature range assuming that there is a dominant deep level acceptor. The fit to the carrier concentration data yielded acceptor concentration of $6 \times 10^{13} \text{ cm}^{-3}$ and $5 \times 10^{14} \text{ cm}^{-3}$ for samples #46 and #47, respectively. The degree of disorder as determined by $S(\alpha)$ was two times larger for sample #47 than sample #46. The improvement in the quality of heteroepitaxy by growing a buffer homoepitaxial layer is well known. The improvement of the alloy disorder by a factor of two seems to agree with these observations. However, the increase in acceptor impurity concentration by an order of magnitude can not be explained on the basis of improvement in epilayer quality.

Recently it was suggested by Eguchi et. al. that a thin conductive layer at the InGaAs-InP heterojunction was the cause of higher carrier concentration observed in a sample grown on an InP buffer layer [57]. However, the degree of ionized-impurity scattering in our samples grown without any InP buffer layer indicates that the concentration of donor impurities in these samples is as high as in InGaAs epilayers grown on top of an InP buffer layer. Although the free carrier concentration of sample

#47 is quite low (as shown in figure 3.1), the poor low temperature mobility agrees with our analysis that this is a result of heavy compensation rather than high purity of this sample. Any impurities coming from the gas sources would also be present in sample #46, yet this does not show any significant ionized impurity scattering at temperatures as low as 40K. One explanation is the out-diffusion of deep level impurities from the Fe doped InP substrate, which are presumably stopped by the 0.2 μ m undoped InP buffer of sample #46. The polaron data on these samples is consistent with this interpretation. In type A samples (with InP buffer layer), the slope of doping concentration profile versus the depth extending from the InP/InGaAs interface was steep. Whereas in type B samples the slope had a low gradient and penetrated deep into the InGaAs layer. A deep level defect originating from the substrate epilayer interface may also be the cause of higher compensation observed in the InGaAs epilayers grown directly on the SI InP substrate.

In summary, we have examined the low-field electron transport in InGaAs grown on SI InP substrates, with and without an InP buffer layer. It is found that InGaAs epilayers grown directly on SI InP substrates have inferior electron transport properties due to enhanced scattering. This is believed to be caused by high acceptor compensation by the out-diffusion of Fe from the SI InP substrate.

CHAPTER 4
THE GENERALIZED STEADY STATE DIODE EQUATION:
THE STATE EQUATIONS APPROACH

4.1 Introduction

Computer simulation of semiconductor (SC) devices is being used extensively in the microelectronics industry. Commercial software packages, such as PISCES, have been developed for silicon based devices. However, development of software for simulating non-silicon devices has been slow. Even in the case of silicon, computer codes have been written based on assumptions which limits the use of these programs. For example, the high-degeneracy and high injection regimes have been omitted in most of the available computer codes due to the immense computational requirements. We present below our initial results of a theory developed for solving a generalized diode equation that can be used for silicon and non-silicon materials.

The general approach in simulating the SC devices is either by decoupling the equations and finding a consistent solution by iterative techniques or by creating a large piecewise linear matrix [58,59]. Even in the case of a simple pn junction, due to the immense computational requirements in obtaining solutions, abrupt space-charge

edge (ASCE) approximation and Boltzman statistics is used together with the assumption of fully ionized impurities. The failure of ASCE approximation has been previously shown for one sided abrupt junctions [60,61,62]. Although the temperature dependence of occupancy of impurities has been properly incorporated to the device simulations [63] to account for impurity freeze-out, the occupancy statistics have to be incorporated in the spatial calculations also, in a generalized diode equation. The occupancy statistics play a crucial role especially in the solution of heterojunctions, where the "built-in" potential of the junction is comparable to the bandgap of the narrow bandgap material. In addition, a better approximation of the Fermi-Dirac (F-D) integral (rather than the first term of a power series expansion, see equation 4-33) has to be used in calculating the charges in the "depleted" region. Numerical approximations for the Fermi-Dirac integral(s) are outlined in an extensive review article [64].

In this chapter the diode equation is written in the form of a five-dimensional state equation with the implication of using space as the independent variable instead of time. The non-causality in space has to be considered in choosing the origin and the boundary conditions. A multistep numerical integration algorithm is used for simultaneously solving these first order differential equations. The solutions for both the homojunction and heterojunction in thermal equilibrium is discussed for the case of abrupt doping profile. The non-equilibrium conditions are incorporated in the state

equations by defining the quasi Fermi levels of holes and electrons and the electric field as three dependent variables. Continuity equations are then incorporated by adding the electron and hole current as the two other dependent variables. Using these five variables the diode equation is reduced to a five-dimensional nonlinear state equation of the form $\hat{e}' = f(\hat{e}, \hat{u}, x)$. The state vector \hat{e} contains electric field, quasi-Fermi levels and the currents, and the input vector \hat{u} contains the other spatially dependent variables. Note that \hat{u} appears redundant since we have specified $f(\hat{e}, \hat{u}, x)$ to be non-linear. However, it will be meaningful when we write the Jacobian of the system in the matrix form of $\delta\hat{e}' = A\delta\hat{e} + B\delta\hat{u}$.

4.2 Formulation of State Equations

In this section we have outlined the equations used in formulating the diode equations in the form of state equations. The summary of the widely known equations governing the physics of the semiconductor devices is included for the sake of completeness.

The basic equations that describe the semiconductor-device operation has been previously classified in three groups: Maxwell equations, current density equations, and continuity equations [65,66,67]. For steady state conditions in the absence of magnetic field the equations that govern the behavior of carriers in a device structure

are then given by; (see p. 72 for the list of symbols)

$$\nabla \cdot E = \frac{\rho(x)}{\epsilon} \quad (4-1)$$

$$J_n = q\mu_n nE + qD_n \nabla n \quad (4-2)$$

$$J_p = q\mu_p pE - qD_p \nabla p \quad (4-3)$$

$$\nabla \cdot J_n = -q(G_n - U_n) \quad (4-4)$$

$$\nabla \cdot J_p = q(G_p - U_p) \quad (4-5)$$

The displacement vector is also related to the intrinsic Fermi level (ϕ_i) yielding the Poisson equation.

$$\nabla \phi_i = -E \quad (4-6)$$

$$\nabla^2 \phi_i = -\frac{\rho(x)}{\epsilon} \quad (4-7)$$

The electron density in the conduction band and hole density in the valence band is given by (steady state equilibrium statistics is assumed) [66,68];

$$n = \int_{E_c}^{\infty} f(E)g(E)dE = N_c \mathcal{F}_{1/2}(\eta_n) \quad (4-8)$$

$$p = \int_{-\infty}^{E_v} f(E)g(E)dE = N_v \mathcal{F}_{1/2}\left(-\eta_p - \frac{E_g}{kT}\right) \quad (4-9)$$

where

$$\eta_n = \frac{\phi_n - E_c}{kT} \quad (4-10)$$

$$\eta_p = \frac{\phi_p - E_c}{kT} \quad (4-11)$$

The correction for non-parabolic bands can also be incorporated into equation 4-8 and 4-9 including $\mathcal{F}_{3/2}$ [68]. For simplicity we will limit our discussion to the parabolic bands. The variable η will be chosen as the dependent variable of the state equations. For heterojunctions η will have to be displaced by the electron affinity of the material to assure continuity across the junction. We will discuss the extension of the equations to heterojunctions after we have formulated the state equations for the homojunction. The diode equations will first be formulated in thermal equilibrium (η_n

$= \eta_p$) and then the non-equilibrium conditions will be incorporated. In thermal equilibrium the Fermi level is the same for both holes and electrons, hence the state vector consists of two variables: the electric field and the Fermi level. The equations to be solved are then;

$$\frac{\partial E}{\partial x} = \frac{q}{e} [N_v \mathcal{F}_{1/2}(-\eta - \frac{E_g}{kT}) - N_c \mathcal{F}_{1/2}(\eta) + N_D^+ - N_A^-] \quad (4-12)$$

$$\frac{\partial \eta}{\partial x} = -\frac{1}{kT} \frac{\partial E_c}{\partial x} = -\frac{qE}{kT} \quad (4-13)$$

where N_D^+ , N_A^- are the ionized donor and acceptor concentrations respectively. At this point the occupancy statistics for the impurities has not been incorporated in the equations, however the formulation used will be discussed with the results of the heterojunction. An extensive discussion on the occupancy of multilevel impurities in a semiconductor can be found in reference 68. Note that the state equations do not involve the current density equations in thermal equilibrium. The validity of this omission can be shown by inserting equation 4-8 into equation 4-2 and using the

properties of derivative of F-D integral as given below [68]

$$\frac{\partial}{\partial \eta} \mathcal{F}_j(\eta) = \mathcal{F}_{j-1}(\eta) \quad (4-14)$$

$$\nabla n = \left(\frac{\partial n}{\partial E_c} \right) \nabla E_c = -\frac{\nabla E_c}{kT} N_c \mathcal{F}_{-1/2}(\eta) \quad (4-15)$$

In thermal equilibrium equation 4-2 can then be rewritten as

$$\frac{D_n}{\mu_n} = \frac{kT}{q} \left[\frac{\mathcal{F}_{1/2}(\eta)}{\mathcal{F}_{-1/2}(\eta)} \right] \quad (4-16)$$

For the non-degenerate case the term in bracket reduces to unity yielding the Einstein relation. For the degenerate case this term corrects for the use of Boltzman distribution in defining the diffusion coefficient in a degenerate semiconductor where the electron energies can be higher than a few kT above the conduction band.

In typical semiconductor device calculations the potential values at the boundaries are already given as the applied voltage. Hence the Poisson equation has the Dirichlet boundary conditions. Specifying the electric field at the boundaries is another choice which is known as the Neumann boundary conditions. However a solution to the Poisson equation does not exist with both conditions specified [69]. Since the charge density is a function of the potential given by the F-D integrals, a unique solution of

equation 4-7 determines both the electric field and the charge density in the device. Equations 4-2 and 4-3 are then overspecification of the problem if the device is in thermal equilibrium. The need to overspecify the problem arises from the fact that Fermi statistics can not be easily incorporated into the Poisson equation. Hence the current density equations are used to correct the solution for charge neutrality. In thermal equilibrium ($J_n=J_p=0$) equations 4-2 and 4-3 are merely a special case (non-degenerate) of the general solution.

In the case of thermal non-equilibrium the Fermi level for electrons and holes is no longer a single variable. However the current density of the carriers is related to the gradient of the quasi-Fermi levels as given below. The validity of these equations and further elaboration can be found in reference 66.

$$J_n = n\mu_n \nabla\phi_n \quad (4-17)$$

$$J_p = p\mu_p \nabla\phi_p \quad (4-18)$$

Inserting the above equations into equation 4-10 and 4-11 the relation between the derivative of the state variable η , the electric field and currents is obtained.

The continuity equation is already a first order differential equation. We need to rewrite this as a function of quasi-Fermi level in order to use it in the state

equations. In steady state the general form of continuity equations can be written as [66];

$$\frac{\partial J_n}{\partial x} = -G_E + \frac{n-n_o}{\tau_n} \quad (4-19)$$

$$\frac{\partial J_p}{\partial x} = G_E - \frac{p-p_o}{\tau_p} \quad (4-20)$$

where G_E is the generation rate of carriers due to external stimulation, n_o and p_o are the carrier concentrations in thermal equilibrium, and τ_n , τ_p are the electron and hole lifetimes respectively. The actual formulation of the carrier lifetime depends on the recombination process considered. We will assume that the carrier lifetime is independent of the Fermi level and the current. However, carrier lifetime given as a function of position or any of the state variables can be incorporated into the state equations. The equilibrium carrier concentrations p_o and n_o are determined by the state variable η which is the solution of equations 4-12 and 4-13 (the thermal equilibrium solution). We will limit our discussion of formulation of non-equilibrium carrier concentrations to the case of non-degenerate equilibrium conditions. The case where the equilibrium conditions are also degenerate has to be solved numerically using the solutions of the equilibrium concentrations as given variables (note that they will not appear in the state vector but will rather be considered in the input vector \hat{u}).

For the case of non-degeneracy in thermal equilibrium we can use the equations given below [68];

$$\frac{np}{n_o p_o} = \exp(\eta_n - \eta_p) \quad (4-21)$$

$$n_o p_o = n_i^2 = (p - p_e)(n - n_e) \quad (4-22)$$

where n_i is the intrinsic carrier concentration, and p_e , n_e are excess holes and electrons, respectively. The dependence of the pn product on the impurity concentration can also be incorporated using the formulation given in reference 70. The above equations reduce to a quadratic equation when relation between the excess electrons and holes are given (which will depend on the process considered). Considering band-to-band generation recombination ($n_e = p_e$) the quadratic equation can be written as;

$$n_e^2 - n_e [N_c \mathcal{F}_{1/2}(\eta_n) + N_v \mathcal{F}_{1/2}(-\eta_p - \frac{E_g}{kT})] + n_i^2 \exp(\eta_n - \eta_p) = n_i^2 \quad (4-23)$$

Alternatively, Shockley-Read-Hall (SRH) recombination model can be used to obtain

the generation-recombination rate (U) through a single impurity level to be used in equations 4-4 and 4-5 [71].

$$U = \frac{1}{\tau} \frac{pn - n_i^2}{p + n + 2n_i} \quad (4-24)$$

Since the n and p can be obtained from the quasi-Fermi levels the formulations above are used in formulating the state equations in terms of the excess carriers (or generation-recombination rate for SRH model) as a function of quasi-Fermi levels. Other mechanisms and generation due to external stimulation are accounted for in the input vector \hat{u} (embedded in the term G_E). Hence the generalized state equations for the homojunction diode are written as given below.

$$\frac{\partial E}{\partial x} = \frac{q}{e} [N_v \mathcal{F}_{1/2}(-\eta_p - \frac{E_g}{kT}) - N_c \mathcal{F}_{1/2}(\eta_n) + N_D^+ - N_A^-] \quad (4-25)$$

$$\frac{\partial \eta_n}{\partial x} = \frac{1}{kT} [-qE + \frac{J_n}{\mu_n N_c \mathcal{F}_{1/2}(\eta_n)}] \quad (4-26)$$

$$\frac{\partial \eta_p}{\partial x} = \frac{1}{kT} [-qE + \frac{J_p}{\mu_p N_v \mathcal{F}_{1/2}(-\eta_p - \frac{E_g}{kT})}] \quad (4-27)$$

$$\frac{\partial J_n}{\partial x} = \frac{q n_c(\eta_n, \eta_p)}{\tau_n} - qG_E \quad (4-28)$$

$$\frac{\partial J_p}{\partial x} = -\frac{q p_c(\eta_n, \eta_p)}{\tau_p} + qG_E \quad (4-29)$$

In vector notation these equations are written in compact form as $\hat{e}' = f(\hat{e}, \hat{u}, x)$, which is the general notation used for specifying non-linear state equations. The matrix formulation of these equations (piecewise local linearization) and the Jacobian of the system will be given in the next section.

The definition of the state variable η has to be modified for heterojunctions. The vacuum level has to be taken as the reference energy level for the quasi-Fermi levels to ensure the continuity of the state variable η . This is done by incorporating the electron affinity of the material in the definition as given below.

$$\eta_n = \frac{\phi_n - E_c - \theta}{kT} \quad (4-30)$$

where θ is the electron affinity of the material. The formulation for holes is similar. This definition of the state variable can be incorporated into equations 4.25-29 by changing the term involving the F-D integrals as given below.

$$\mathcal{F}_{1/2}(\eta_n) \rightarrow \mathcal{F}_{1/2}\left(\eta_n + \frac{\theta}{kT}\right) \quad (4-31)$$

$$\mathcal{F}_{1/2}\left(-\eta_p - \frac{E_g}{kT}\right) \rightarrow \mathcal{F}_{1/2}\left(-\eta_p - \frac{E_g + \theta}{kT}\right) \quad (4-32)$$

Choosing the displacement vector D instead of electric field as the state variable is also necessary since electric field is discontinuous across the heterojunction. Hence these equations can be generalized to accommodate the heterojunctions as well. For abrupt junctions (this is also the case for abrupt doping profiles) some of the functions on the right hand side of the above expressions will be discontinuous resulting in discontinuity of the first derivative of the related state variable. Note that across the heterojunction the mobilities and the effective density of states in the conduction and the valence bands will be different. In solving these functions numerically the points at which there is a discontinuity should be considered as the boundaries to achieve stability in computations. However since the state variables are chosen to be continuous, the

boundary conditions for the equations on both side of the junction will be the same. For graded junctions (both in doping and bandgap) the numerical solutions can be obtained by linearly varying the material dependent parameters across the junction and reducing the step size to obtain linearly varying derivative of the state vector.

For the existence and uniqueness of the solution, the state transition function $f(\hat{e}, \hat{u}, x)$ has to be both continuous and continuously differentiable (at least piecewise). By expressing the spatially varying constants in the diode equations with error functions the existence and uniqueness of the solution will be guaranteed. The abrupt junctions can be approximated as steeply graded junctions. This will also make the solutions compatible with the more realistic case of diffused junctions in which the doping profile is already expressed with an error function. Alternatively, the abrupt junction can also be solved as two independent initial value problems with the same initial conditions. In the next section we will discuss the solution of the non-linear state equations defining the diode.

4.3 Solution of State Equations

The diode state equations can be represented as a lattice structure with the state vector as the weights of the adaptive finite impulse response (FIR) filter. The discussion of modelling systems with unknown responses by the use of adaptive FIR filters can be found in reference 72. The equations have to be linearized to some extent in order

to define each lattice as a matrix of constant coefficients. The linearization of the diode equations require the linearization of the F-D integral. For the semiconductor where the Fermi level is within the bandgap the F-D integral always has a negative argument. Hence we can use the power series given below for evaluating the F-D integral [64].

$$\mathcal{F}(\eta) = \sum_{r=1}^{\infty} \frac{(-1)^{r+1} e^{\eta}}{r^{j+1}} \quad (4-33)$$

The generalized linearization of the diode equations can be achieved by using the powers of exponentials as the state variables. In this approach the number of equations will increase depending on the number of terms used from the series given above. Of course this will introduce redundant equations in the formulation, hence the matrix obtained, has to be reduced before a solution is attempted. The reduction of the matrix can easily be done by using the singular value decomposition [73].

Linearization can be illustrated for the case where the spatial gradient of the currents can be neglected (i.e. high carrier lifetime and absence of external excitation). In that case the continuity equations are decoupled from the state equations reducing the dimension of the state vector to three. The 3x3 state transition matrix is shown below using only the first exponential of the power series (non-degenerate approximation). The diode equation is written as $\hat{e}' = A\hat{e} + \hat{u}$. Note that the transfer matrix (A) involves the electric field hence it is still not linearized and it is rank deficient. However the Taylor

$$A = \begin{bmatrix} 0 & -\frac{q}{e}N_c & \frac{q}{e}N_v e^{-\frac{E_f}{kT}} \\ 0 & -\frac{qE}{kT} & 0 \\ 0 & 0 & \frac{qE}{kT} \end{bmatrix}, \hat{u} = \begin{bmatrix} N_D^+ - N_A^- \\ \frac{J_n}{kT\mu_n N_c} \\ \frac{-J_p}{kT\mu_p N_v} \end{bmatrix}, \hat{e} = \begin{bmatrix} E \\ e^{\eta_n} \\ e^{-\eta_p} \end{bmatrix} \quad (4-34)$$

series expansion of this set of equations yields a linear matrix (linear in terms of the partial derivatives) since the higher order derivatives are zero. For constant current and impurity concentration the Jacobian of the state transition matrix (A') is then obtained by Taylor series expansion as ($\delta\hat{e}' = A'\delta\hat{e}$) [74];

$$A' = \begin{bmatrix} 0 & -\frac{q}{e}N_c & \frac{q}{e}N_v e^{-\frac{E_f}{kT}} \\ -\frac{qe^{\eta_n}}{kT} & -\frac{qE}{kT} & 0 \\ \frac{qe^{-\eta_p}}{kT} & 0 & \frac{qE}{kT} \end{bmatrix}, \delta\hat{e} = \begin{bmatrix} \delta E \\ \delta e^{\eta_n} \\ \delta e^{-\eta_p} \end{bmatrix} \quad (4-35)$$

The Jacobian matrix is useful in obtaining the proper variation of the state variables with respect to each other. In the iterative methods this matrix will be used to obtain the initial variation of the other two state variables when a solution is being searched for in one dimension. A lattice structure based on equation 4-34 and 4-35 can be used as the basis for the adaptive filter for which the response is to be found. The solution

of the problem through such a lattice structure will be faster and more efficient. However, we have chosen a multistep dynamical integration technique to obtain numerical solution which allows more control over the solution at every step so as to keep the data in the form of meaningful physical quantities. The Jacobian matrix obtained above is still used to extend the one dimensional search algorithms for the proper initial conditions to three dimensions. Also the Jacobian would be required (to avoid numerical difference approximations) when a backward differentiation method is applied to the problem.

In solving the diode equations for given initial conditions the absence of causality in space (for steady state solutions) has to be taken into account. The problem has to be defined in such a way as to specify the "input" at the origin and keep it constant. This can be achieved in abrupt junctions by choosing the junction as the origin and solving the n side and the p side separately and matching the initial conditions of both sides. For linearly graded junctions a backward differentiation predictor-corrector technique can be used. A discussion on numerical methods for solving state equations can be found in reference 75. The state space approach [76] and the non-homogeneous vector matrix difference equation is discussed in reference 77 and 74.

The validity of the solutions obtained by numerical integration of the given state equations depends on two main factors. First one is the exact (or with a given accuracy as in the case of approximation of the F-D Integrals) formulation of the physics of the

problem in the state transition function. Secondly, the meaningful initial conditions that can be explained in terms of physics. Using the state transition function as formulated in equations 4-25 through 4-29, the initial conditions were chosen so as to extract a given number of charges from each side that corresponds to the initial value of the electric field (hence satisfying equation 4-1). The solution of the given structure is approached by increasing the absolute value of the electric field in small increments and finding the potential to be applied to each side to achieve the corresponding depletion of carriers. The solution is found when the band structure coincides at the origin. For the heterojunctions the solution is found when the vacuum level coincides. To speed the convergence and yet achieve stability (keeping the integration within a physically meaningful region at all steps) the Newton-Raphson algorithm is combined with a damped feedback loop iteratively determining the value of the initial electric field. The system stability and the rate of convergence is studied by the use of phase plots in the case of thermal equilibrium.

4.4 Computational

The computations were carried out on the CRAY-YMP at National Center for Supercomputer Applications (NCSA), University of Illinois at Urbana-Champaign (UIUC). The numerical integration was done using the DEABM subroutine from DEPAC library which is a variable order ordinary differential equation solver based on

the Adams-Bashforth method [78]. The results obtained for homojunctions and heterojunctions in thermal equilibrium are discussed below. The material parameters of InGaAs (lattice-matched to InP) and InP used in the numerical calculations are given in Table 4.1. The InGaAs-InP material system which is of great interest in optical communications applications is chosen due to our interest in modelling the devices we have fabricated. The fabrication and the properties of these devices will be discussed in Chapter 6. The solution for the homojunction and heterojunction is obtained for thermal equilibrium. The complete state equations 4.25-29 are used with the initial conditions specified for thermal equilibrium to demonstrate the downward compatibility of these equations and the methodology used. The results presented below are given as the initial evaluation of the competency of the methodology outlined in this paper. The solutions are obtained assuming single level traps in the material (uncompensated material). In the simulation of a "real" structure the compensation and the fixed interface charges have to be accounted for. These can be directly incorporated into the solutions by defining the ionized impurities as a function of space and quasi-Fermi levels. We have incorporated the occupancy statistics in the formulation for the solution of heterojunction problem where the Fermi level on the n type InGaAs was too high for assuming the donors to be completely ionized, as discussed below.

Table 4.1. Material parameters of InGaAs and InP used in the computer simulations. (The tabulated values are calculated at room temperature)

Parameters	InGaAs	InP
E_g (eV)	0.75	1.35
ΔE_c {InGaAs-InP} (eV)	-	0.22
N_c (cm ⁻³)	2.08×10^{17}	5.89×10^{17}
N_v (cm ⁻³)	1.20×10^{19}	1.97×10^{19}
ϵ (pF/cm)	1.22	1.09
Θ (eV)	4.62	4.4

For the homojunction case a narrow bandgap material InGaAs is used to emphasize the effect of free carriers in the "depleted" region. The phase plot of the successive calculations are plotted in figure 4.1. The thick lines correspond to the initial integration. The successive integration paths fall on the same line on the phase plot and the program converges to the final solution in a very stable manner. The electric field, band structure, and free carrier concentrations as a function of position are given in figures 4.2,3, and 4 respectively. The band structure and the carrier concentrations are obtained from the state variable η using equations 4-8 through 4-11. Figure 4.4 shows the high concentration of holes on the "n" side of the junction. Note that the hole concentration across the metallurgical junction is higher than the total donor concentration. The effect of the high hole concentration on the gradient of the electric field is clearly seen in figure 4.2 at the vortex of the triangle. The ASCE approximation results in a linear gradient of the electric field yielding the well-known triangular form given in many text books on semiconductor devices. The failure of the ASCE approximation has been previously discussed in reference 60. The omission of free carriers in the "depleted" region results in miscalculation of the depletion width, electric field, and the junction capacitance. This effect is even more significant in narrow bandgap semiconductor devices.

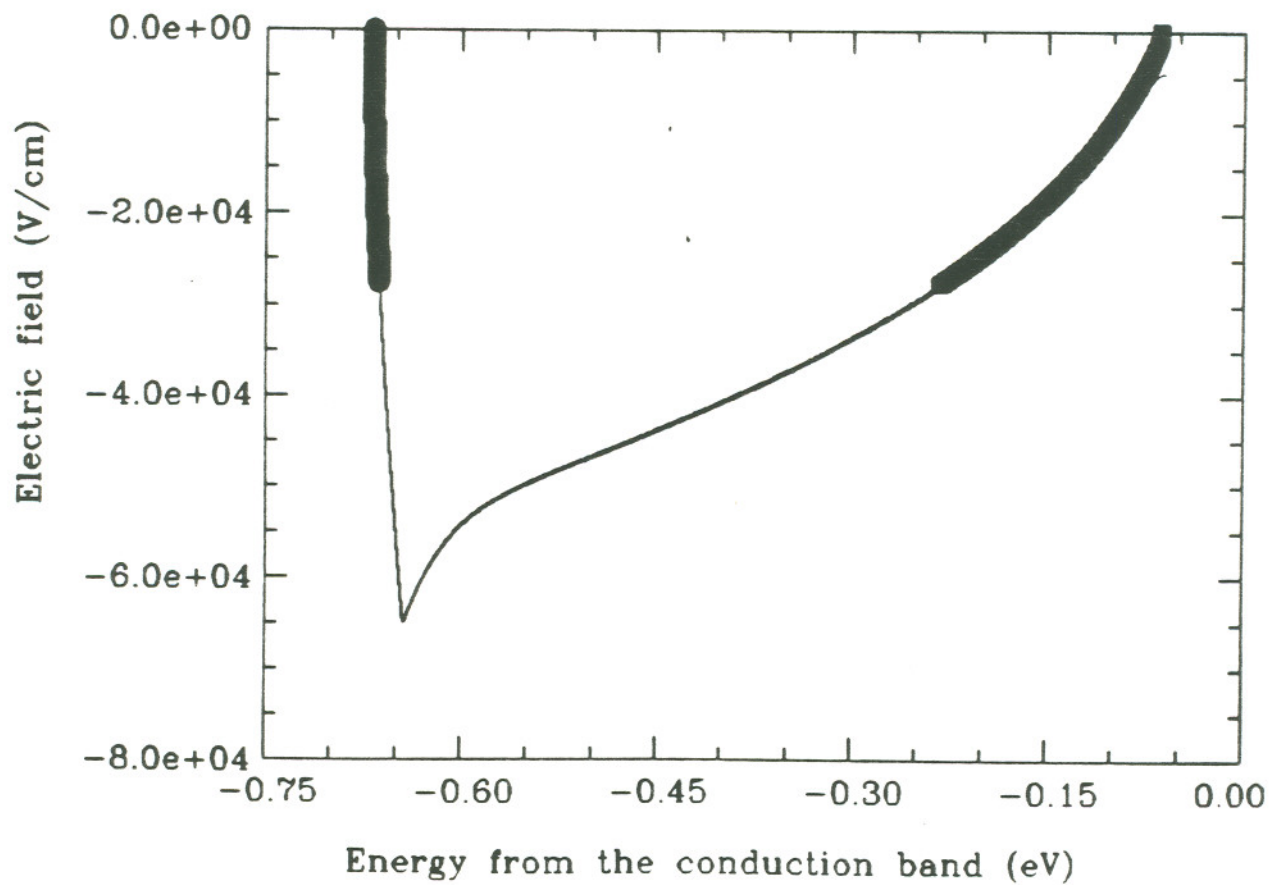


Figure 4.1. Phase plot for the solutions of the abrupt p⁺-n InGaAs homojunction at thermal equilibrium. The thick lines correspond to the initial integration path. Ten successive steps follow the same line till both sides converge at a point.

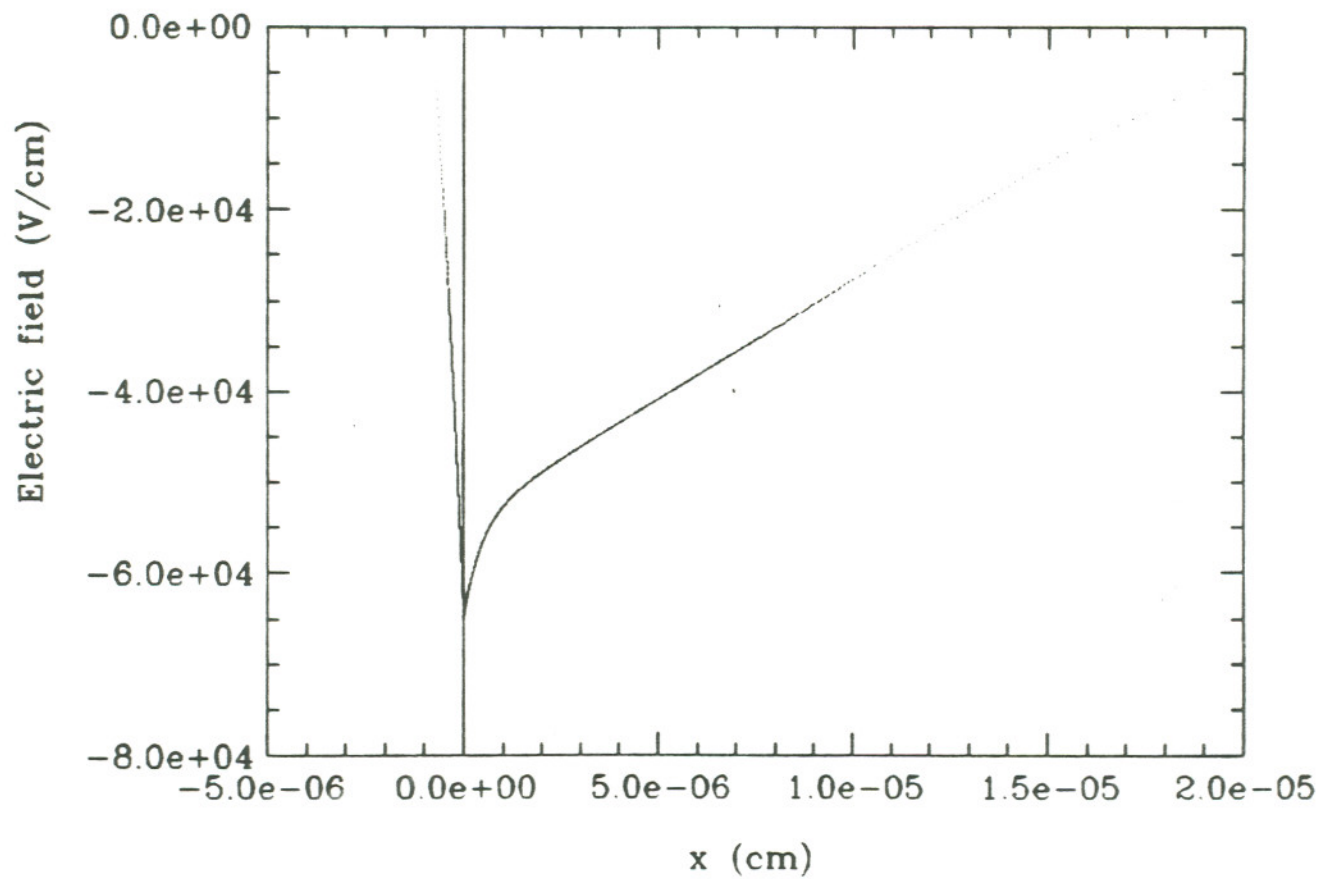


Figure 4.2 Calculated electric field of the abrupt p^+ -n InGaAs homojunction for the doping concentrations given in figure 4.4.

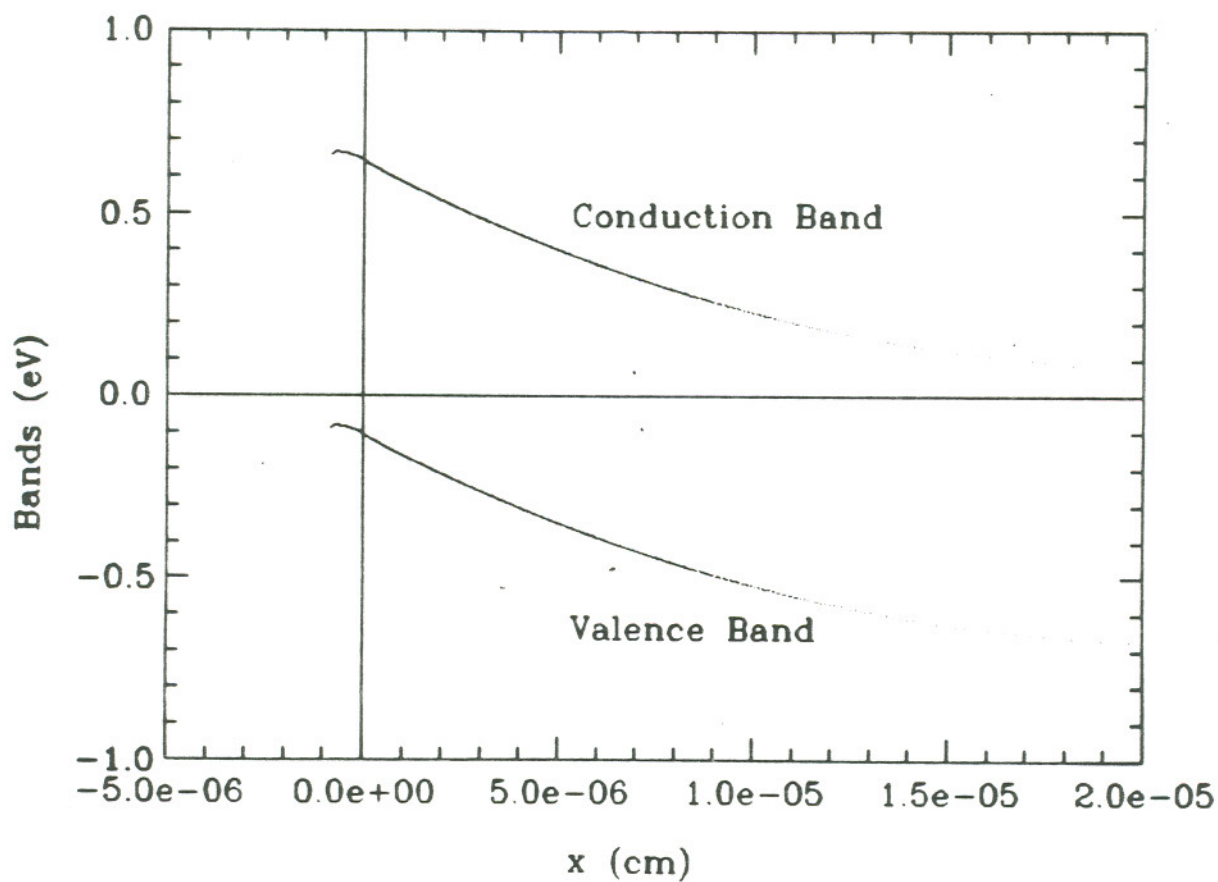


Figure 4.3 Calculated band structure of the abrupt p⁺-n InGaAs homojunction for the doping concentrations given in figure 4.4. The displacement of the conduction and the valence band are given with respect to the fermi level taken to be zero.

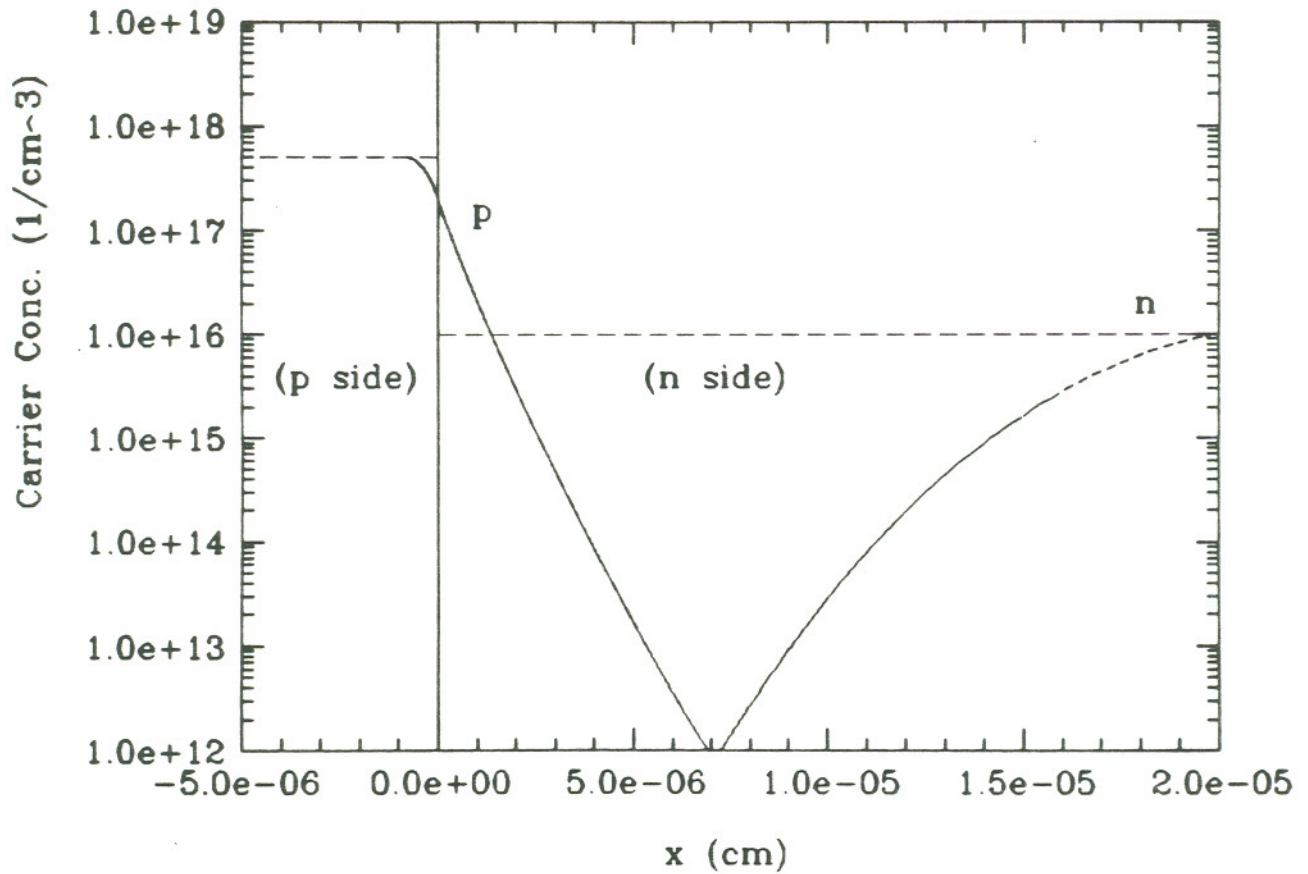


Figure 4.4 Calculated carrier concentrations of the abrupt p⁺-n InGaAs homojunction as function of position. The junction is at the origin, and the acceptor and the donor concentrations are shown as dashed lines ($N_D = 1 \times 10^{16} \text{ cm}^{-3}$, and $N_A = 5 \times 10^{17} \text{ cm}^{-3}$).

For the heterojunction case we have calculated p^+n InP-InGaAs junction. The heavy doping is specified on the wide bandgap InP side to emphasize the need to use the exact F-D integral in the equations as will be apparent in discussing the results. Phase plots of successive steps in finding the correct electric field at the origin is plotted in figure 4.5. The system response is not as stable as the homojunction however the last two integration paths do fall on top of each other and the desired value of the conduction band discontinuity is reached while the charge neutrality is satisfied. The stability of the system can be improved by increasing the damping on the feedback loop at the cost of increased computations. We would like to reiterate the fact that the feedback loop is used only in estimating the initial values and do not interfere with the integration of the state equations. Hence the error coefficients and corrections are calculated on the basis of validity of physical quantities. The damping is used to compensate for the errors involved in estimating the initial conditions (i.e. ASCE approximation). The phase plot is used to study the path of integration for given initial values. Once the initial values are found the diode equation is solved in a single integration step. A higher damping coefficient was used for the heterojunction due to unavailability of accurate approximations for the initial conditions.

The solutions obtained from the final integration step are given in terms of electric field, band structure, and free carrier concentrations in figures 4.6, 4.7 and 4.8 respectively. It can be seen in figure 4.7 that the narrow bandgap InGaAs is driven by

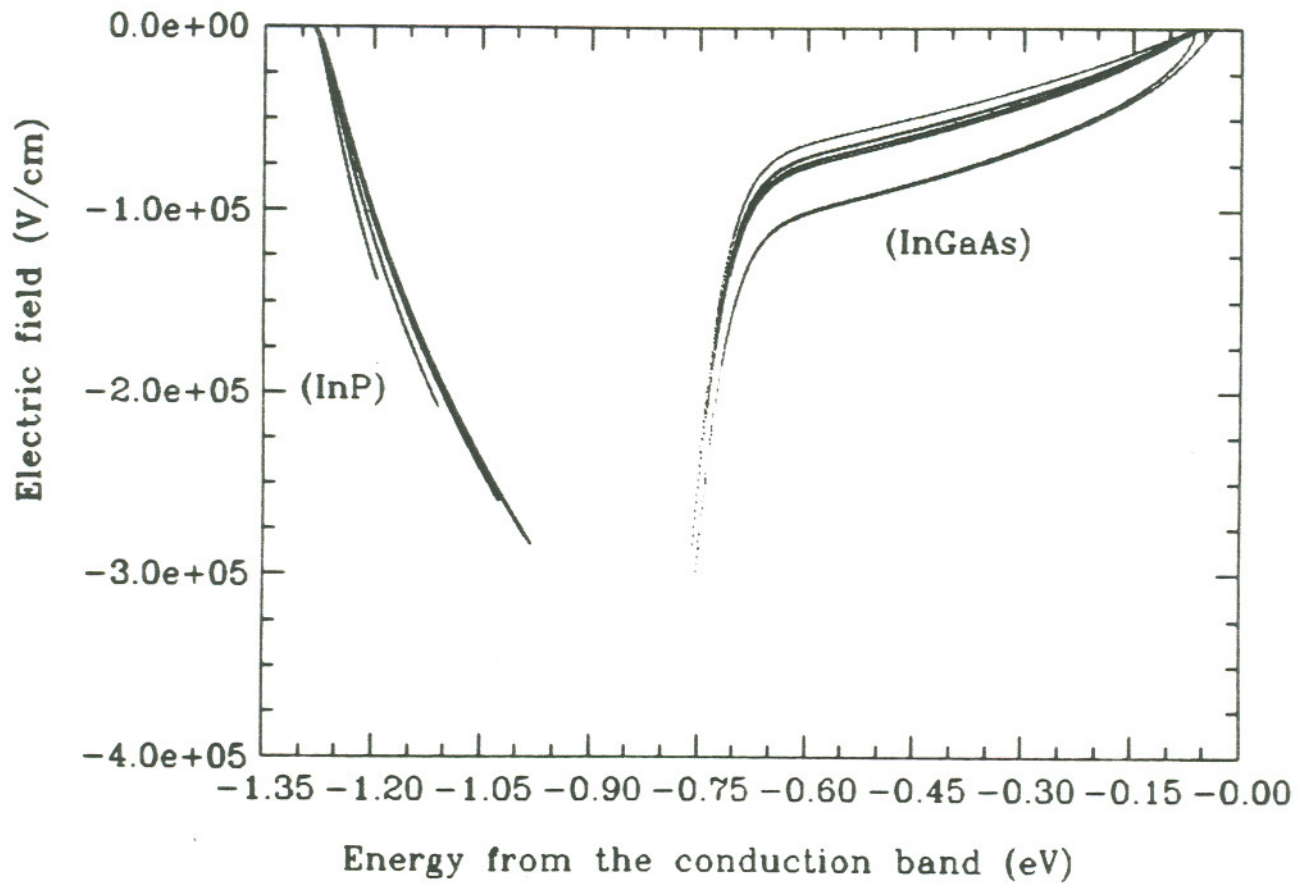


Figure 4.5. Phase plot for the solutions of the abrupt p⁺-n InP-InGaAs heterojunction at thermal equilibrium. Integration paths of fifteen successive steps with increasing initial value of the electric field is plotted. The gap between the two sets of lines correspond to the conduction band discontinuity.

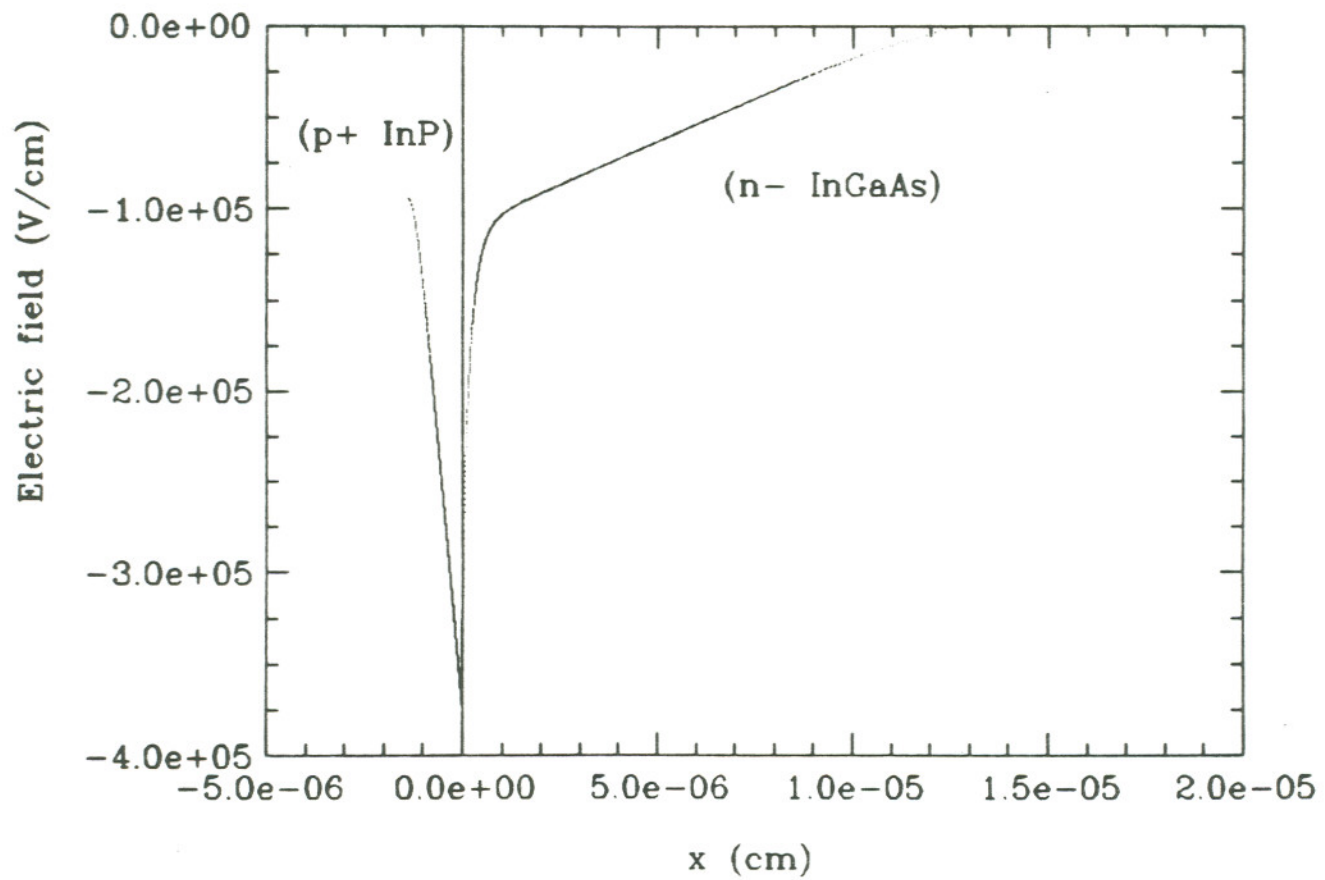


Figure 4.6 Calculated electric field of the abrupt p⁺-n InP-InGaAs heterojunction for the doping concentrations given in figure 4.8.

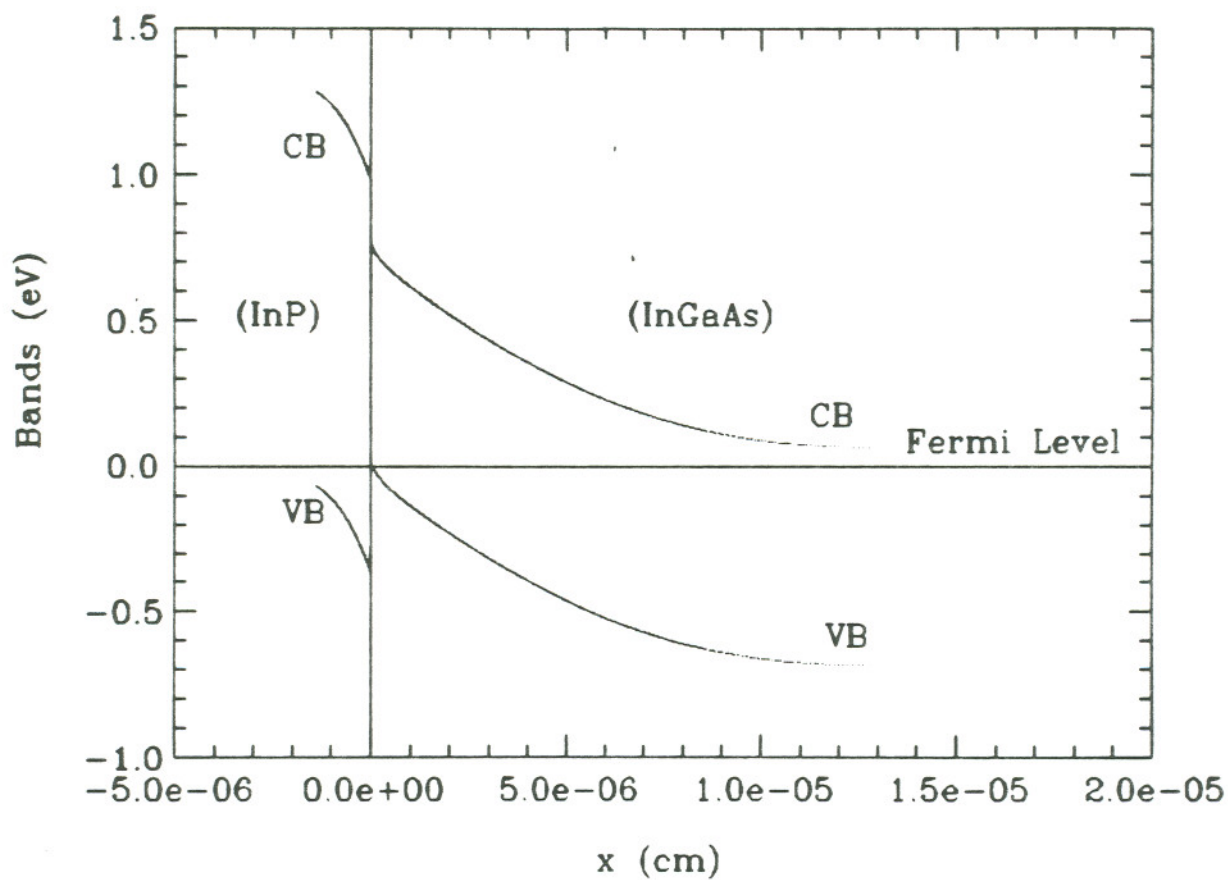


Figure 4.7 Calculated band structure of the abrupt p^+n InP-InGaAs heterojunction the doping concentrations given in figure 4.8. The displacement of the conduction and the valence band are given with respect to the fermi level taken to be zero.

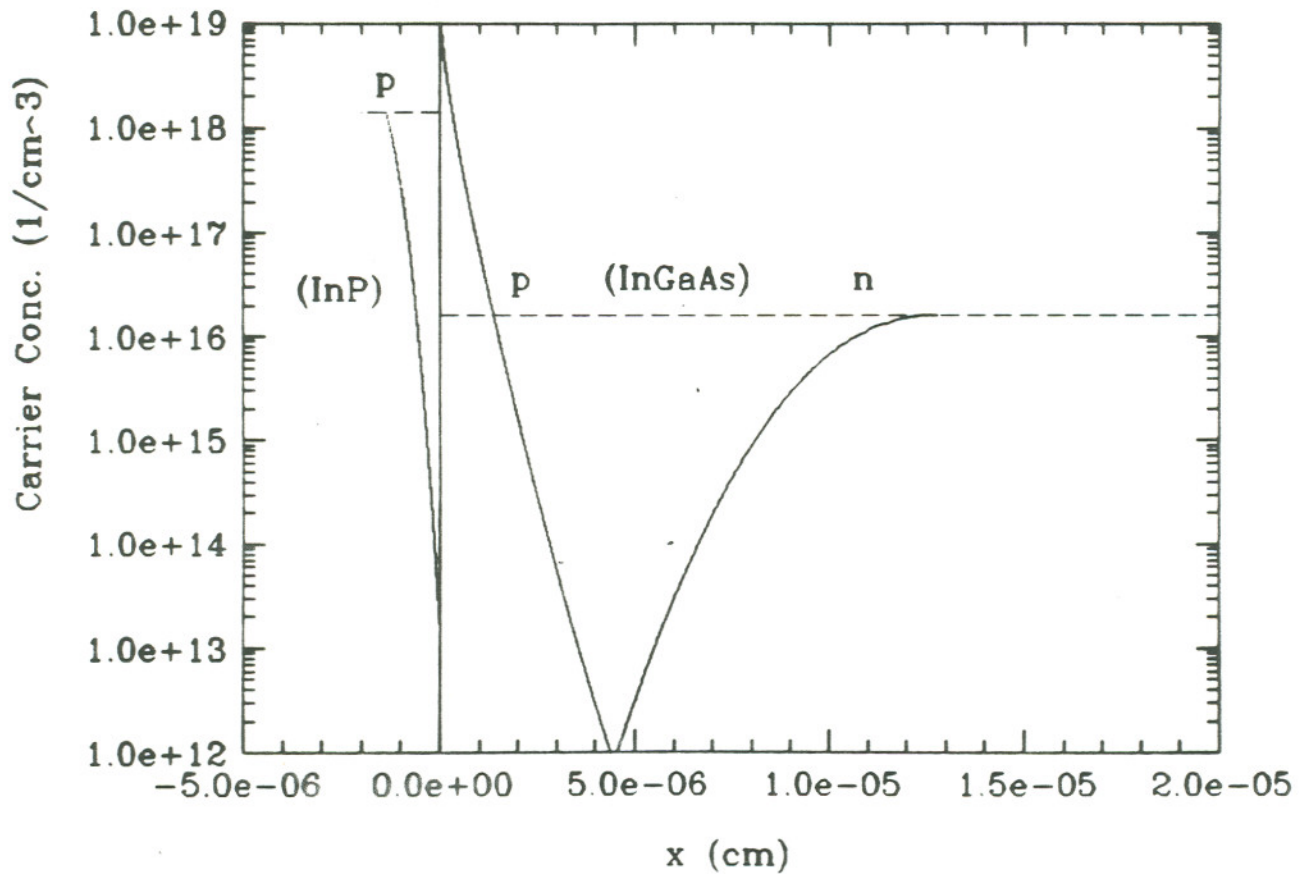


Figure 4.8 Calculated carrier concentrations of the abrupt p⁺-n InP-InGaAs heterojunction as function of position. The junction is at the origin, and the acceptor and the donor concentrations are shown as dashed lines ($N_D = 1.8 \times 10^{16} \text{ cm}^{-3}$, and $N_A = 1.5 \times 10^{18} \text{ cm}^{-3}$).

a high electric field to accommodate a built-in potential close to its bandgap. Close to the origin the use of exact F-D Integral is essential in accurately calculating the hole concentration on the "n-type" InGaAs side where the Fermi level is within a few kT of the valence band. The electric field calculated for the heterojunction is given in figure 4.6. Note that maximum electric field at the metallurgical junction is much higher than the electric field that would be obtained from a typical homojunction of InGaAs. The high electric field results in the state variable η to rapidly approach zero (corresponding to Fermi level coinciding with the conduction band). Hence even for a shallow donor complete ionization approximation will not hold. The solutions plotted in figures 4.6 through 4.8 are obtained by assuming a shallow donor level 1 kT below the conduction band (in reality the donor ionization energy will be slightly higher than this for the available dopants in this material) and calculating occupancy of donors as a function of Fermi level. The ionized donors in equation 4-25 are calculated as [68];

$$N_D^+ = N_D \frac{\beta \exp(-\eta_n - \frac{E_d}{kT})}{1 + \beta \exp(-\eta_n - \frac{E_d}{kT})} \quad (4-36)$$

where β is the spin degeneracy weighting factor (taken as unity in the calculations for simplicity), E_d is the donor ionization energy, and N_D is the total donor concentration.

We emphasize the need to use occupancy statistics especially in this problem where the solution can not otherwise be obtained. On the InP side the ionized acceptor concentration was assumed to be constant. Since we have defined the problem with Dirichlet boundary conditions the integration terminates as η reaches the boundary value. The effect of omitting the occupancy statistics on the InP side is then clearly seen in figure 4.6 as the non-zero electric field at the end where the potential has reached its boundary condition.

Another interesting point that can be seen in the figures 4.7 and 4.8 is that the discontinuity and the "bending" of the valence band is consistent with the high concentration of holes on the InGaAs side of the junction accumulated due to the potential barrier. The band structure of InP-InGaAs heterojunction plotted in figure 4.7 resembles more of field effect transistor than a diode with a depleted space charge region.

The realization of the diode equations in the form of state equations and the solution technique that we have outlined offers flexibility in the type of equations that can be incorporated into the basic equations. And for a given initial condition the solution is uniquely determined. The validity of initial conditions obtained from other methods can be instantly checked by studying the integration path on the phase plot. The results we have given in this section is for the purpose of demonstrating the technique. We believe the results are still significant, especially in the case of the

heterojunction, where the continuity of the displacement vector (D), the continuity of the energy of the vacuum level, and charge neutrality are simultaneously solved.

4.5 Conclusions

We have outlined a technique for solving the diode equations as a set of state equations. The set of first order differential equations are then solved simultaneously as a non-linear dynamic system allowing important physical equations to be incorporated into the solutions. The incorporation of Fermi-Dirac statistics, and the occupancy considerations of the impurities are demonstrated in solving a hypothetical InGaAs-InP junction using the actual material parameters. The functional relation between the electron and hole quasi-Fermi levels are written explicitly in the equations. The solution of the diode equation with the applied bias can be obtained using this technique without having to use the Boltzman statistics and ASCE approximation. To obtain the solution for the diode equation as a function of applied bias, this technique has to be coupled with the five dimensional search algorithms (i.e steepest descent, least mean squares) used in adaptive filtering applications [72]. There is extensive literature on developing methods for solving dynamic non-linear systems (i.e. for speech recognition, Seismic signal analysis and image processing). This formulation of the diode equations will enable the physics of semiconductor statistics to be incorporated in the semiconductor device calculations using the methods developed in general to

solve non-linear non-causal systems. We believe in the long run adaptive signal processing will be the key element in analyzing the semiconductor devices.

The integration of the state equations using numerical techniques requires very little computation, however the validity of the solution crucially depends on the correct initial conditions. Hence without an efficient multidimensional search algorithm the integration has to be carried out numerous times. Work is under way in defining the state transition matrix as a lattice block (each block represent a solution in space) with feedback from the other lattices in correcting the initial value. The technique developed will be applied in calculating the current voltage and capacitance voltage characteristics of a diode.

4.6 Appendix 4.1 List of Symbols

D	: displacement vector
D_n	: diffusion coefficient for electrons
D_p	: diffusion coefficient for holes
E	: electric field
E_c	: energy at the conduction band edge
E_g	: energy gap
E_v	: energy at the valence band edge
ϵ	: dielectric constant
$f(E)$: the probability of occupancy of a given state with energy E
\mathcal{F}_j	: The Fermi-Dirac integral of order j
$g(E)$: density of states with energy E
G_n	: electron generation rate
G_p	: hole generation rate
J_n	: electron current density
J_p	: hole current density
k	: Boltzman constant
μ_n	: electron mobility
μ_p	: hole mobility
N_c	: effective density of states in the conduction band
N_v	: effective density of states in the valence band
n	: free electron concentration
p	: free hole concentration
q	: electronic charge
ρ	: total charge density
Θ	: electron affinity
U_n	: SRH generation-recombination rate for electrons
U_p	: SRH generation-recombination rate for holes
ϕ_i	: intrinsic Fermi level
ϕ_n	: quasi-Fermi level for electrons
ϕ_p	: quasi-Fermi level for holes

CHAPTER 5

PIN DIODE AND THE STATE EQUATIONS FORMULATION

5.1 Introduction

In InGaAs/InP double-heterojunction PIN devices the electric field across the undoped InGaAs layer is a very important variable. In most commonly used design calculations of these devices the electric field is taken to be linearly varying through out the InGaAs layer [2]. A self-consistent solution of the carrier distribution and the electric field has not been incorporated into the heterojunction device calculations. This is mostly due to difficulties in incorporating the conduction band discontinuity into the semiconductor equations as discussed in chapter 4. The heterojunction has to be studied taking into consideration the epilayer growth and related material issues, as well as the effects of the band discontinuity on the device simulations. The equations obtained with approximations suitable for a homojunction (i.e. abrupt space charge approximation) can not be extended to these devices by simply using different dielectric constants across the heterojunction. The Poisson equation and the current continuity equations have to be solved simultaneously without the abrupt space charge approximation. The model developed in chapter 4 to examine the band structure and carrier concentration

is applied to PIN diode in this chapter. In these p-i-n devices the typical dopant concentrations ($\approx 5 \times 10^{18} \text{ cm}^{-3}$) used on the n and p side requires the use of equations appropriate for degenerate conditions.

5.2 Self-Consistent Solutions of Energy Bands and Carrier Distribution

The state equations approach formulated in chapter 4 is used in obtaining the numerical solutions for the PIN diode. We have combined this method with state estimation techniques to obtain the solutions in a single iteration. The diode equations in thermal equilibrium are written as vector state equations;

$$\vec{e} = f(\vec{e}, x) \quad (5-1)$$

$$f(\vec{e}, x) = \begin{bmatrix} \frac{q}{e} \{ N_D \mathcal{F}_{1/2}(-\eta - \frac{E_g + \theta}{kT}) - N_A \mathcal{F}_{1/2}(\eta + \frac{\theta}{kT}) + N_D^+ - N_A^- \} \\ -\frac{qE}{kT} \end{bmatrix}, \quad \vec{e} = \begin{bmatrix} E \\ \eta \end{bmatrix} \quad (5-2)$$

where

$$\eta = \frac{\phi - E_c - \theta}{kT} \quad (5-3)$$

and N_D^+ , N_A^- are the ionized donor and acceptor concentrations respectively. E_c is the conduction band energy and ϕ is the Fermi energy. $\mathcal{F}_{1/2}$ is the half order Fermi-Dirac integral. θ is the difference between the electron affinities, the exact formulation is

discussed in reference 79. The conduction band discontinuity is taken to be 0.22eV consistent with experimental measurements [80]. The results for the PIN diode were obtained by solving the state equations for each junction separately and combining the solutions. The validity of the solutions is iteratively checked by integrating a cubic-spline [81] fit of the derivatives of the state variables (given by equations 5-1 and 5-2) starting from the boundaries, and comparing it with the state variables obtained. Hence the charge neutrality condition and current density equations are solved simultaneously. The state equations were integrated using Differential Equation Solver with Adams-Bashforth multi-step (DEABM) numerical integration algorithm [78]. The "velocity" error (error in the derivative of the variables) of integration is corrected by applying Extended Kalman Filtering (EKF) to the perturbation of the state variable. Extensive discussion on EKF and its application to non-linear dynamical systems can be found in references 82 and 83. We have used the DEABM as the predictor equation. The integration of the derivatives from the boundary values is taken as the measurement. EKF gain matrix is calculated using the Jacobian of the state transition matrix (measurement matrix) and is given in equation 5-4.

$$F_x = \begin{bmatrix} 0 & -\frac{q}{e} N_c \mathcal{F}_{-1/2}(\eta_n) & \frac{q}{e} N_v \mathcal{F}_{-1/2}(-\eta_p - \frac{E_g}{kT}) & 0 \\ -\frac{q}{kT} & \frac{J_n N_c \mathcal{F}_{-1/2}(\eta_n)}{n^2 \mu_n kT} & 0 & \frac{1}{n \mu_n kT} \\ \frac{q}{kT} & 0 & \frac{(J - J_n) N_v \mathcal{F}_{-1/2}(-\eta_p - \frac{E_g}{kT})}{p^2 \mu_p kT} & \frac{-1}{p \mu_p kT} \\ 0 & \frac{q p_o}{\tau_n (p + n + 2 p_o n_o)} & \frac{q n_o}{\tau_n (p + n + 2 p_o n_o)} & 0 \end{bmatrix} \hat{e} = \begin{bmatrix} E \\ \eta_n \\ \eta_p \\ J_n \end{bmatrix} \quad (5-4)$$

where F_x is the measurement matrix, \hat{e} is the state vector. Note that at thermal equilibrium ($J = J_n = 0$, $\eta_n = \eta_p$) the rank of the matrix F_x is reduced to two. The error in estimated solution is the difference between the integration of the previously calculated derivatives consistent with the boundary conditions and the value obtained from the perturbation state variable using the measurement matrix. One should note that the prediction is based on the complete state equation but the EKF is applied to the perturbation of the state variable. The predictor equation and the corrector equation are given below. The notation of reference 82 is used and $\hat{e}(k+1|k)$ is the predicted value of the state variable at $x(k+1)$ and $\tilde{e}(k+1)$ is the error in the prediction of the state variable (namely, the difference between the "measured" value and the DEABM integration).

$$\hat{e}(k+1|k) = \hat{e}(k|k) + \int_{x(k)}^{x(k+1)} f(\hat{e}, x) dx \quad (5-5)$$

$$\hat{e}(k+1|k+1) = \hat{e}(k+1|k) + K(k+1; *) \tilde{e}(k+1) \quad (5-6)$$

$K()$ is the standard EKF gain matrix calculated iteratively from the measurement matrix and error in the measurement. A normally distributed white noise is introduced in the calculation of the EKF gain matrix. This noise helps in eliminating the cumulative errors in integration and ensures the non-singularity of the measurement matrix. The minimum noise that has to be introduced to any calculation depends on the machine epsilon and the value of the variable.

The use of EKF is essential for simultaneous multi-dimensional correction of the calculated state vector. The solutions for a junction are obtained by starting with a small perturbation of the state vector and consistently integrating till the boundary conditions at the junction is obtained on both sides. The solutions and the spatial span of integration is then checked with respect to the device geometry and the position of the other junction.

Solutions obtained for devices with $0.5\mu\text{m}$ thick InGaAs absorbing layers grown with and without undoped InP buffer layers are discussed below. The band structures obtained from the simulations are shown in figures 5.1 and 5.2. In both cases the

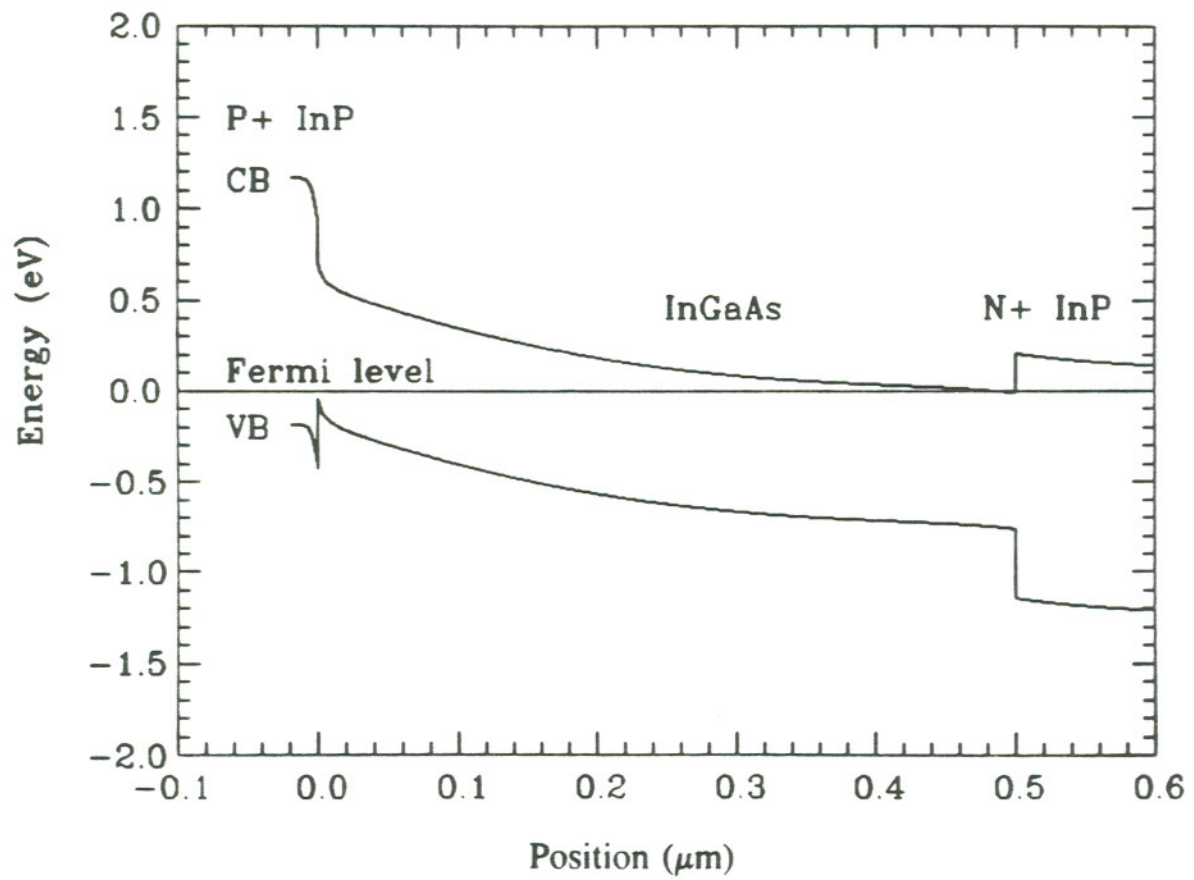


Figure 5.1. Band structure of InP/InGaAs/InP PIN diode grown with InP buffer. The Fermi level is chosen as zero energy value and the top junction is chosen as the origin.

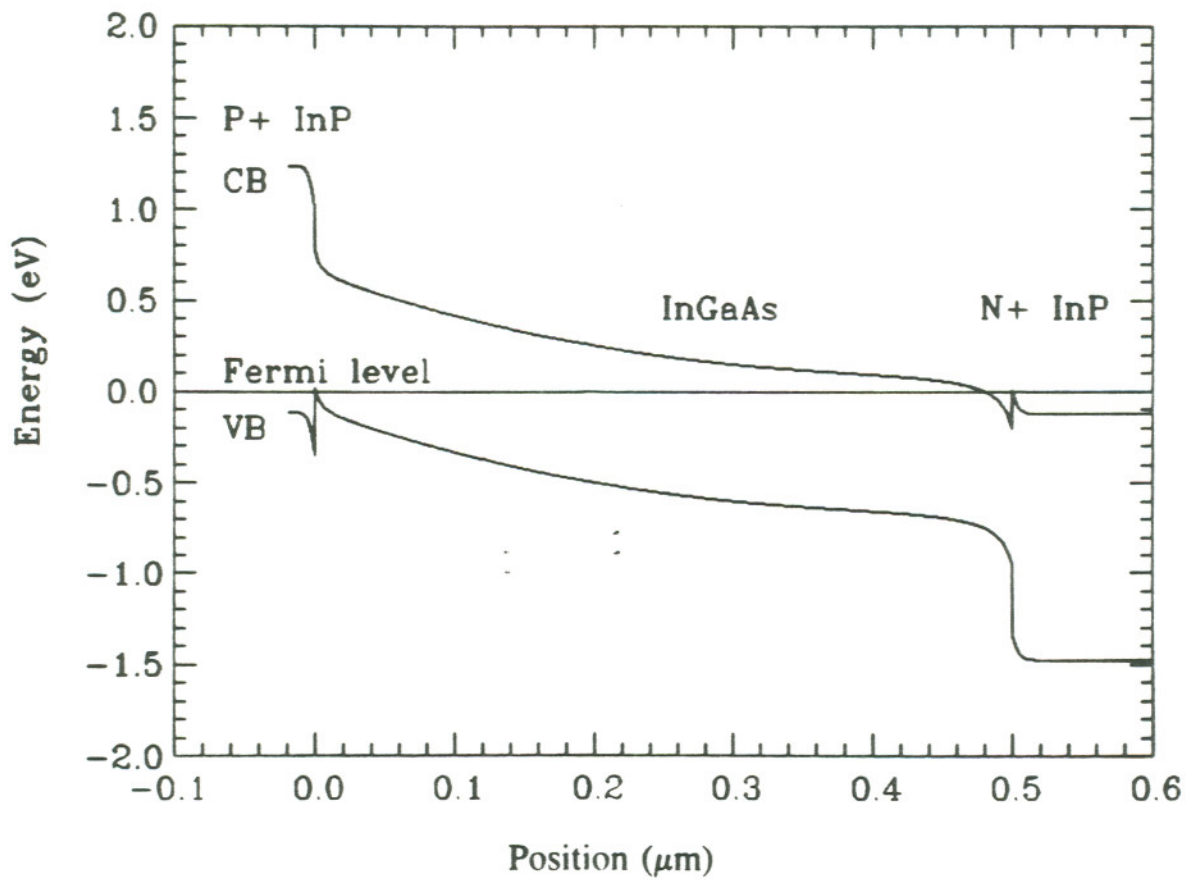


Figure 5.2. Band structure of InP/InGaAs/InP PIN diode grown without an InP buffer. The Fermi level is chosen as zero energy value and the top junction is chosen as the origin.

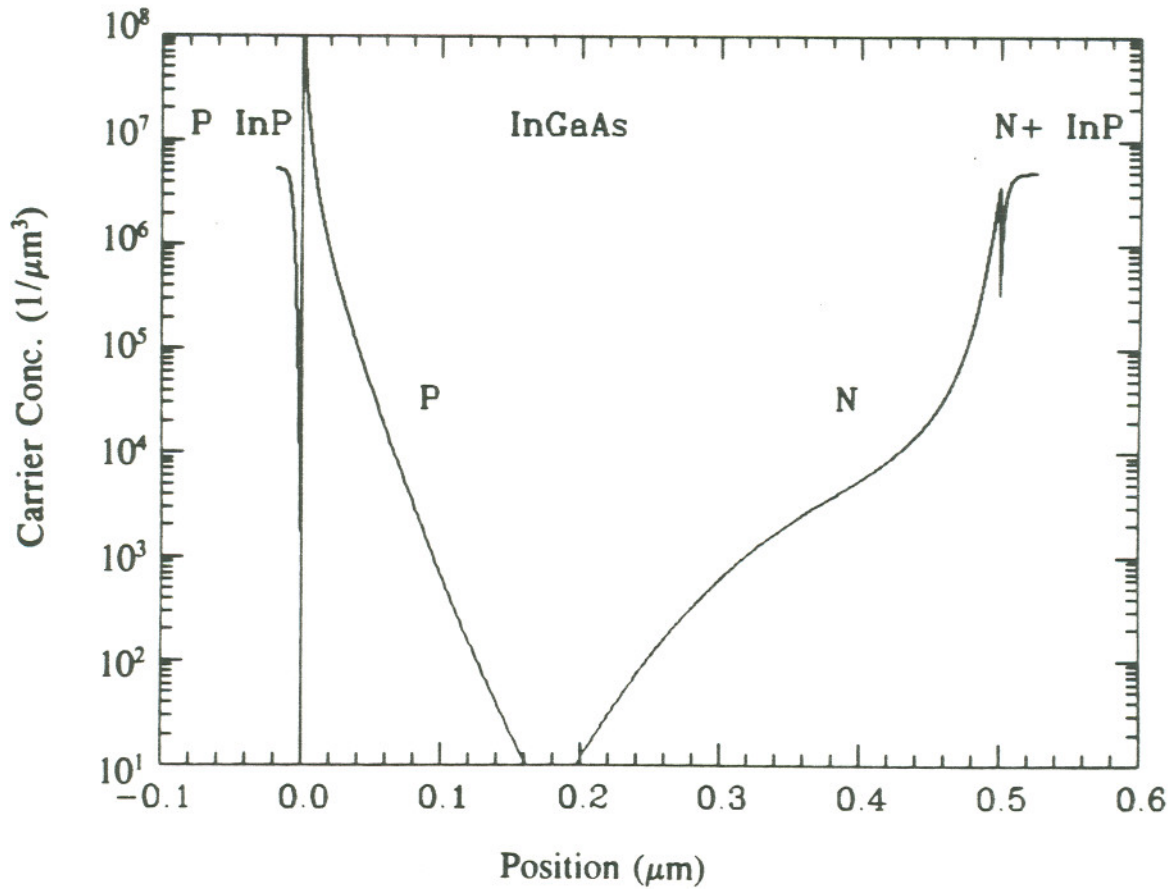


Figure 5.3. Calculated carrier concentration of PIN diode grown without an InP buffer layer consistent with the band structure given in figure 5.2. The donor and acceptor concentrations in the top and bottom InP layers are $5 \times 10^6 \text{ cm}^{-3}$. The InGaAs layer is unintentionally doped with $N_D = 2 \times 10^4 \text{ cm}^{-3}$.

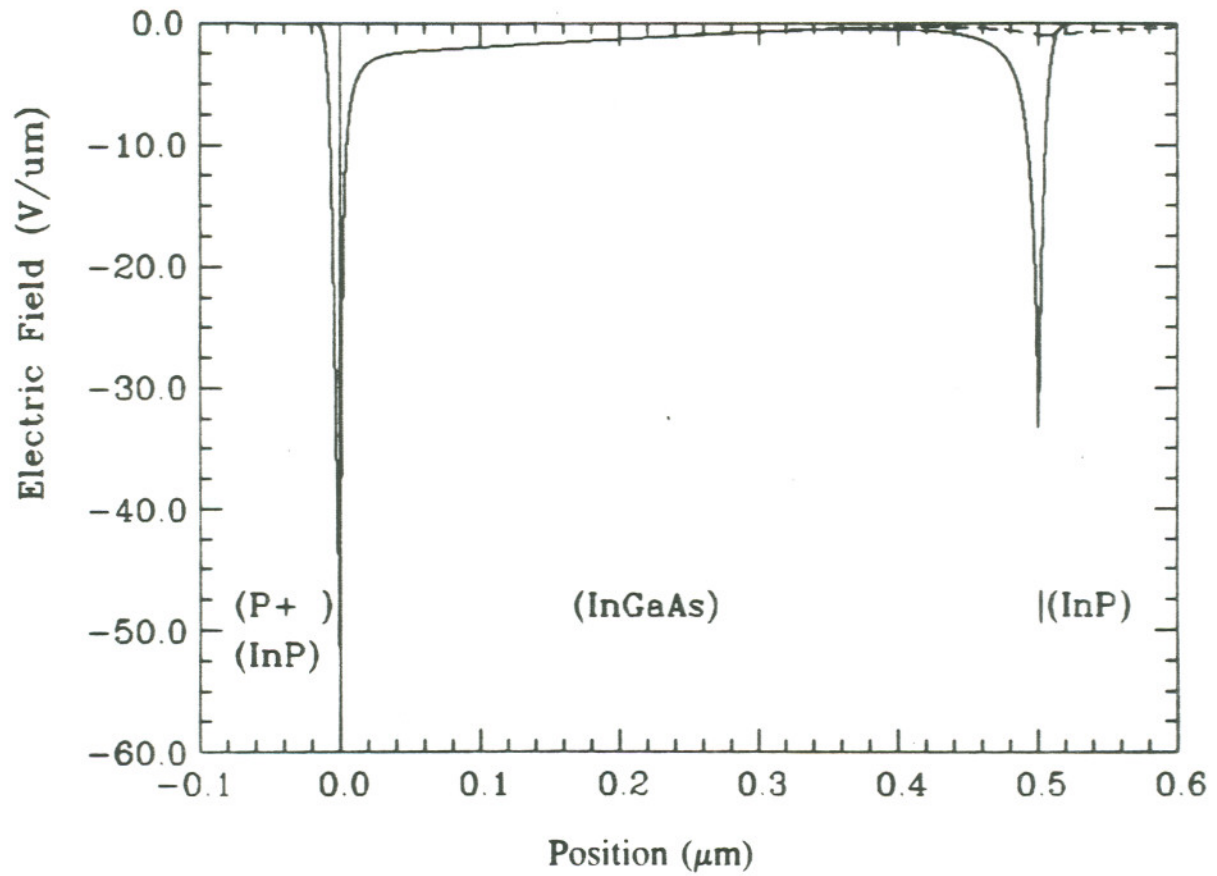


Figure 5.4. Calculated electric field of PIN diode grown with an undoped InP buffer layer (dashed line), and without a buffer layer (solid line).

InGaAs layer near the top heterojunction is driven into degeneracy to accommodate a built-in potential close to its bandgap. This is enhanced due to larger bandgap on the InP side, and resulting built-in potential and electric field is significantly larger than the solutions that can be obtained for a InGaAs homojunction. It is essential to use Fermi-Dirac integral in the solutions instead of Boltzmann statistics in this region. The hole concentration on the InGaAs side of the junction is significantly larger than the concentration of any donor states that exist in these unintentionally doped epilayers. The accumulation of holes at the junction due to valence band discontinuity is clearly seen in figure 5.3. This results in the high gradient of the electric field (figure 5.4) and reduces the zero bias depletion width. It is clear that to obtain a self-consistent solution the free carrier density in the "depleted" region has to be incorporated into the solutions. The peak value of the electric field and the extent of the electric field into the InGaAs layer are significantly different than the results that are given in literature where the Poisson equation was solved using fully depleted space charge approximation. It is important to note that it is not only the peak value of the electric field at the junction that is effected by the free carriers in the InGaAs layer. Since the overall built-in potential is constant, determined by the impurity concentrations in the P and N InP on both sides, the integration of the electric field across the whole structure is predetermined. Hence an increase in the value of the peak electric field results in reduced electric field across the InGaAs layer. This will effect the value of the drift

velocity across the InGaAs layer. If a bias condition is chosen so as to operate the device at higher fields with constant saturated drift velocity, the miscalculation of the electric field could shift the operation to the peak drift velocity region, resulting in instabilities.

The comparison of the calculated results obtained for p-i-n diodes grown with and without the InP buffer layer also provides some important insight. The electric field at the InGaAs/InP n-n isotype heterojunction calculated for the devices grown without an InP buffer layer is almost as high as the top junction due to degeneracy of the n⁺ InP substrate and the conduction band discontinuity. For these devices the capacitance of the n-n⁺ junction will have to be considered. At zero bias the capacitance across the isotype heterojunction can be the major contributing capacitance since the depletion width is extremely short across this one sided (n-n⁺) isotype heterojunction. The measured capacitances are plotted in figure 5.5 as a function of reverse bias for devices with 0.9 μ m InGaAs layer thickness. At low biases the capacitance of the device grown without the buffer layer is higher. Since the capacitances converge to the same value as the InGaAs layer fully depletes, this higher zero bias capacitance can be attributed to the capacitance at the n-n⁺ junction.

The nominal dark current values of the fabricated devices grown with and without buffer layer was also compared. Larger number of devices grown without the InP buffer layer yielded a high dark current compared to similar devices grown with

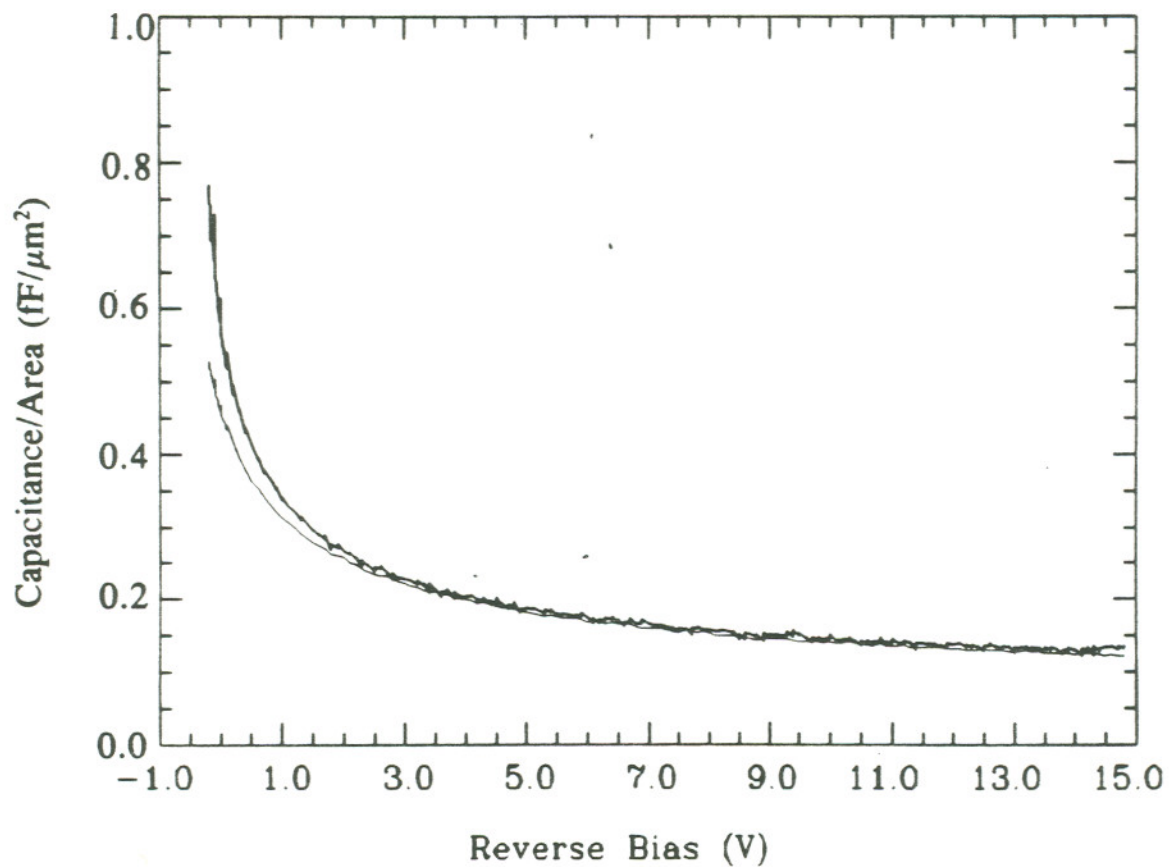


Figure 5.5. Comparison of the capacitance-voltage measurements of the photodiodes with $0.9\mu\text{m}$ InGaAs layer thickness grown with (narrow line) and without (thick line) InP buffer layer. The bias voltage starts at $+0.2\text{V}$ (forward bias) and extends to -15V (reverse bias).

the undoped InP buffer. Although the nominal values of the dark current showed this trend, the variance in the data was too great to statistically confirm this hypothesis. The cause of this variance is most likely the variations in device processing. The process and the data will be discussed in chapter 6. There are several factors that can contribute to the dark current related to material issues. The improvement in the epilayer quality by the use of buffer layer would result in reduced trap density in the InGaAs layer yielding higher minority carrier lifetime. The diffusion of donor impurities from the InP substrate is also reduced by the buffer layer. Another factor that can be considered in light of the simulations presented in this paper is the effect of the high electric field observed at the isotype heterojunction for the devices grown without the InP buffer layer. The high peak value of the electric field combined with the high gradient of the electric field due to accumulation of carriers on the InGaAs side of both the heterojunctions results in a depletion width significantly smaller than the one that can be calculated from the fully depleted space charge approximation. Hence the standard formulation of the dark current with the generation-recombination current (as the major contributing mechanism) derived from the abrupt space charge approximation will yield a lower estimate of the minority carrier lifetime and interface trap density. Although a reasonable agreement with the measurements would be obtained using these variables as fitting parameters, the characterization of these double-heterojunction devices using current-voltage, capacitance-voltage measurements should take into account the

accumulation of carriers due to band discontinuities, which significantly reduces the calculated depletion width and the electric field in the InGaAs layer.

5.3 Conclusion

In summary, we have developed a self-consistent model based on state equations, to calculate the carrier density and band structure in thermal equilibrium of an InGaAs/InP p-i-n detector. The results indicate that the current equations have to be coupled with the Poisson equation in calculating the electric field and the depletion width which forms the basis of any equation used for characterization of these devices by current and capacitance measurements. In future work these calculations will be extended to incorporate bias conditions.

CHAPTER 6

FABRICATION AND CHARACTERIZATION OF PIN PHOTODIODES

6.1 Introduction

High-speed photodetectors are essential components of broad bandwidth optical communication and ultrafast measurement equipment. In the InGaAs/InP material system, PIN photodiodes have been reported with measured impulse response full width at half maximum (FWHM) of 16-17 ps [17,16]. Crawford et.al. have measured 16 ps FWHM on a photodetector with 0.2 μm absorbing layer and 17% quantum efficiency at 1300nm. Recently, Wey et.al. reported a double-heterostructure PIN photodiode with graded band-gap superlattices at the heterointerfaces with a measured 5.0 ps FWHM pulse width and 31% quantum efficiency at 1300nm [18]. This device had a 0.2 μm InGaAs absorbing layer to reduce the transit time and 25 μm^2 device area to reduce the junction capacitance. In this 25 μm^2 device, all of top area was used for metal contact to achieve low series resistance, hence these devices were backside illuminated. For applications that do not require 3dB electrical bandwidths higher than 50GHz, front side illumination reduces the complexity of packaging and offers higher degree of freedom in monolithic integration. We have grown InGaAs/InP structures and fabricated front

side illuminated PIN photodetectors. In this chapter, several parameters related to epilayer growth and device fabrication that affect the measured impulse response and photoresponse are discussed.

In double heterostructure PIN photodiodes the thickness of the InGaAs absorbing layer determines the compromise between the 3dB bandwidth and quantum efficiency. A first order calculation of the tradeoff can be obtained considering the transit time of the carriers and the capacitance of the device [2]. As the device diameter and absorption layer thickness decrease to achieve higher bandwidths the actual form of the spatial photoresponse becomes important. The quantum efficiency of a device has to be considered together with the tolerance in spatial misalignment and core diameter of an optical fiber which is used as an optical source. Under typical bias conditions electric field values in excess of 50kV/cm result in the InGaAs region. Due to intervalley scattering in this material, more than 50% of the electrons are transferred to the L valley in subpicosecond time scale as determined from the Monte Carlo electron transport simulations. This poses an important question regarding the value of "conduction band" discontinuity to be used in device calculations at high electric field bias conditions. Even without the complication of occupancy of the L valley, the band discontinuity (both for the valence band and Γ valley) across the heterojunctions results in accumulation of carriers and a high gradient of the electric field on the InGaAs side of both the heterojunctions as discussed in chapter 5. In order to develop an accurate

model for these devices, it is important to study the relationship between the device performance and basic design parameters such as the InGaAs absorbing layer thickness and the doping profile across the heterojunctions. In this chapter, the photoresponse and optical impulse response measurements are reported as a function of bias and absorbing layer thickness. The results of devices grown with and without an undoped InP buffer layer are also examined.

6.2 Experimental

The InGaAs/InP heterostructures used for this investigation were grown by atmospheric pressure organometallic vapor phase epitaxy (OMVPE) on (100) sulphur doped InP substrates ($n \approx 5 \times 10^{18} \text{ cm}^{-3}$). The epitaxial structure consisted of a 100 nm undoped InP buffer layer (which was omitted for half the samples) followed by an undoped InGaAs absorbing layer (with thicknesses of $0.2 \mu\text{m}$, $0.5 \mu\text{m}$, and $0.9 \mu\text{m}$), a $1.5 \mu\text{m}$ p-type InP layer ($5 \times 10^{18} \text{ cm}^{-3}$), and a 100 nm p-type InGaAs contact layer ($4 \times 10^{19} \text{ cm}^{-3}$). Magnesium was used as a p-type dopant. X-ray Double-Crystal Diffraction (XRDCD) measurement of the complete structure yielded a single diffraction peak with nominal FWHM of 60 arcseconds for the (004) reflection indicating lattice mismatch of less than 150ppm. The absence of any significant tail in the XRDCD peak of these structures have indicated low-defect density at the interfaces. In the early test structures a significant tail on the XRDCD peak had been observed and

the correlation between the observed tail and the defect density originating from the interfaces have been verified by cross-sectional transmission electron microscopy. The tail of the XRDCD peak has been eliminated by optimizing the gas switching procedure during the OMVPE growth. Details of the OMVPE growth are described in chapter 2. Hall measurements have shown the unintentionally doped InGaAs epilayer to be n-type with a carrier concentration of less than $4 \times 10^{15} \text{ cm}^{-3}$ at 300K as discussed in chapter 3. Devices were fabricated on five different tiles taken from the same substrate and grown under identical growth conditions in consecutive runs. The device structures are summarized in Table 6.1 listed in the order the epilayers were grown. The devices will be referred to as PIN-(A-E) followed by the nominal measured diameter of the particular mesa (i.e. PIN-A-17, corresponding to a device fabricated on tile PIN-A with $17\mu\text{m}$ mesa diameter).

Tiles were processed simultaneously in a single fabrication run. The mesas were defined by Br:MeOH (1% Br₂ by weight) etching. The pattern on the mask included two different diameters; $20\mu\text{m}$ and $30\mu\text{m}$. The mesa diameters were $17\mu\text{m}$ and $27\mu\text{m}$ respectively, for the devices with thick undoped InGaAs layer as determined by the mesa etching time. The mesas were then coated with polyimide for passivation. The polyimide was patterned by reactive ion etching for contacting the top surface of the device and depositing metal on the substrate as ground. A ring shaped metal structure was defined by e-beam evaporation and lift-off at the top of the mesa allowing front

side illumination. A Si_3N_4 antireflection coating was then deposited. A TiPt/Au layer was evaporated to form the microstrip and the bonding pad on the polyimide. The dies were bonded to a coplanar waveguide substrate for high speed optical pulse measurements. Cross-sectional schematic diagram of the fabricated photodiodes is given in figure 6.1.

The capacitance-voltage (CV) and current-voltage (IV) measurements were recorded by Keithley-590 and Keithley-536 units interfaced with a Macintosh computer. The spectral response was measured from 600nm to 1700nm using Newport's model 780 lamp as the source. The grating used in the monochromator was 1180grooves/mm for wavelengths 600-780nm and 590grooves/mm upto 1700nm. A 830nm high pass filter was added at 840nm. The output was coupled to a $50\mu\text{m}$ core single mode fiber aligned approximately $25\mu\text{m}$ above the photodetector. The output power was calibrated using a Si detector from 600-1020nm and a Ge detector for longer wavelengths. The setup used for spatial photoresponse scans is discussed in reference 84. The impulse response of the fabricated photodetectors was recorded using a Tektronix CSA803 communication signal analyzer and a Tektronix SD30 sampling head. Electrical contact was made to the detectors using a TNP-9615 Tektronix microwave probe. The bias was applied through Wiltron bias tee K-250 connected to the probe by Wiltron cable K-101M. The optical pulse source was $1.3\mu\text{m}$ distributed feedback laser diode [85] with 3.8ps FWHM compressed pulses. Output laser pulse was split and fed into a photo-

detector used for generating the trigger signal. The details and characterization of the optical pulse source used in these measurements are discussed in reference 86. The sampling period was 512ps, for 512 points, averaged 1024 times. The combined rise time of the microwave probe and sampling head was estimated to be 14.4 ± 0.4 ps from the derivative of the electrical step response of the measurement setup [87] given in figure 6.2 for two different calibration step generators.

6.3 Electrical DC Measurements

The average values of the dark current are given in Table 6.1 for overall comparison of the devices. The lowest dark currents measured were 0.2nA at -10V bias in PIN-C-27. The structures that were grown with an undoped InP buffer layer yielded larger number of devices with low dark currents compared to the structures with identical absorbing layer thicknesses grown without the buffer. The spatial distribution of the measured dark current values did not show any particular trend for the tiles having different InGaAs layer thicknesses. The measured dark currents of the devices were compared at a bias voltage that corresponds to the electric field value of 30kV/cm. At this bias condition one major mechanism that contributes to the dark current is expected to be generation-recombination in the depleted InGaAs layer. In this comparison, the lowest device yield (rejection value chosen as 10nA) was observed for the tile with 0.5 μ m thick InGaAs absorbing layer grown without the InP buffer

Table 6.1. Summary of device structures and DC measurements listed in the order the epilayers were grown using OMVPE.

Device Run	InGaAs Thick. (μm)	InP Buff	Capacitance ($\text{fF}/\mu\text{m}^2$)		Dark Current (nA) at 30kV/cm.	
			{ 27 μm diam. } 0(V) Depleted		(#:number of devices) 17 μm (#)	27 μm (#)
PIN-A	0.5	w	0.48	0.20	$3.3 \pm 2.5(17)$	$5.6 \pm 1.1(24)$
PIN-D	0.5	w/o	0.67	0.23	$36. \pm 20.(17)$	$17. \pm 9.0(16)$
PIN-B	0.2	w/o	1.40	0.84	$1.1 \pm 0.9(18)$	$2.1 \pm 0.7(25)$
PIN-C	0.9	w	0.46	0.12	$1.8 \pm 0.6(18)$	$1.3 \pm 0.8(13)$
PIN-E	0.9	w/o	0.59	0.13	$1.7 \pm 1.4(6)$	$1.3 \pm 0.6(14)$

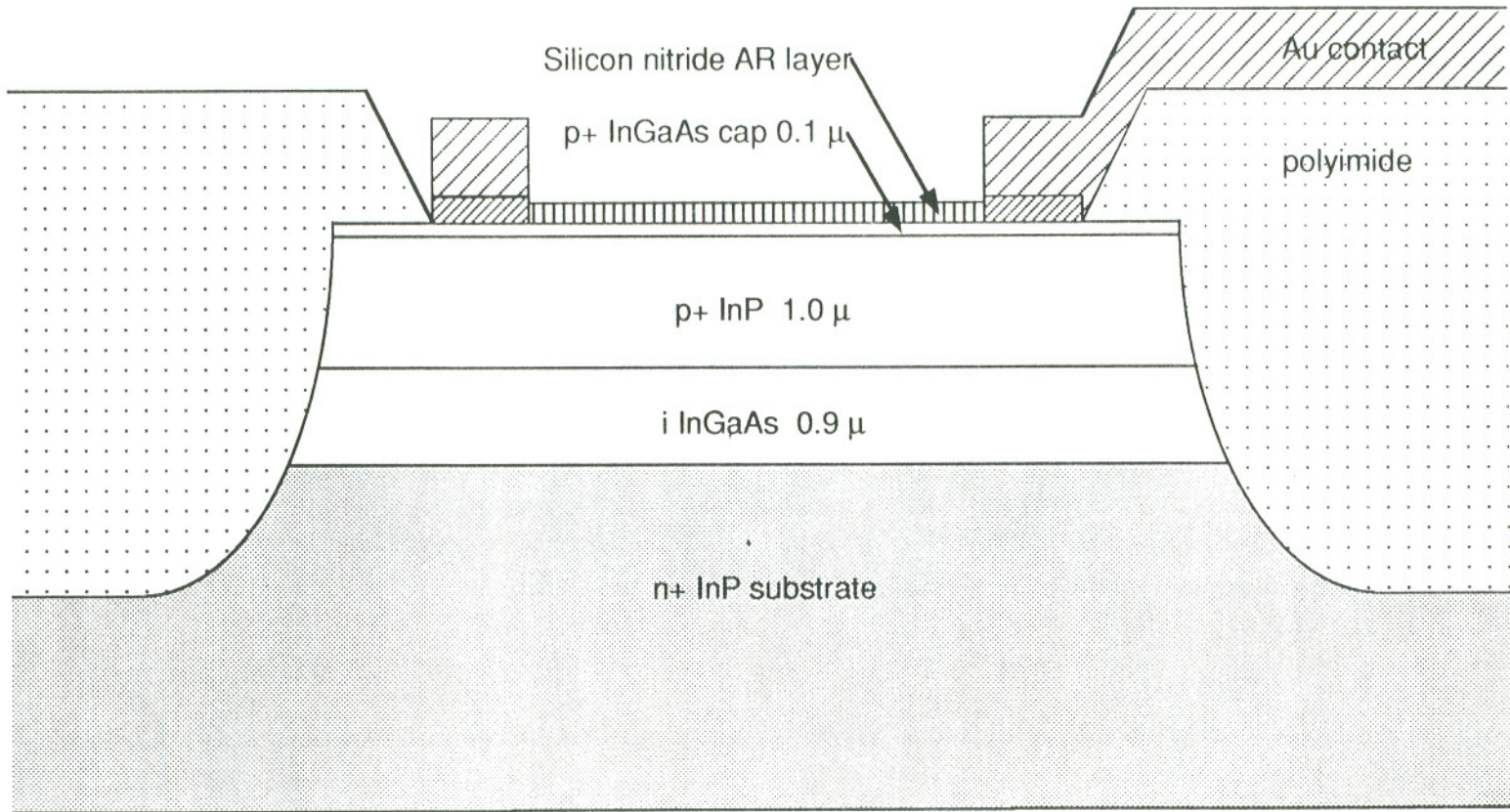


Figure 6.1. Schematic diagram of PIN photodiode. The epilayer thicknesses correspond to PIN-E.

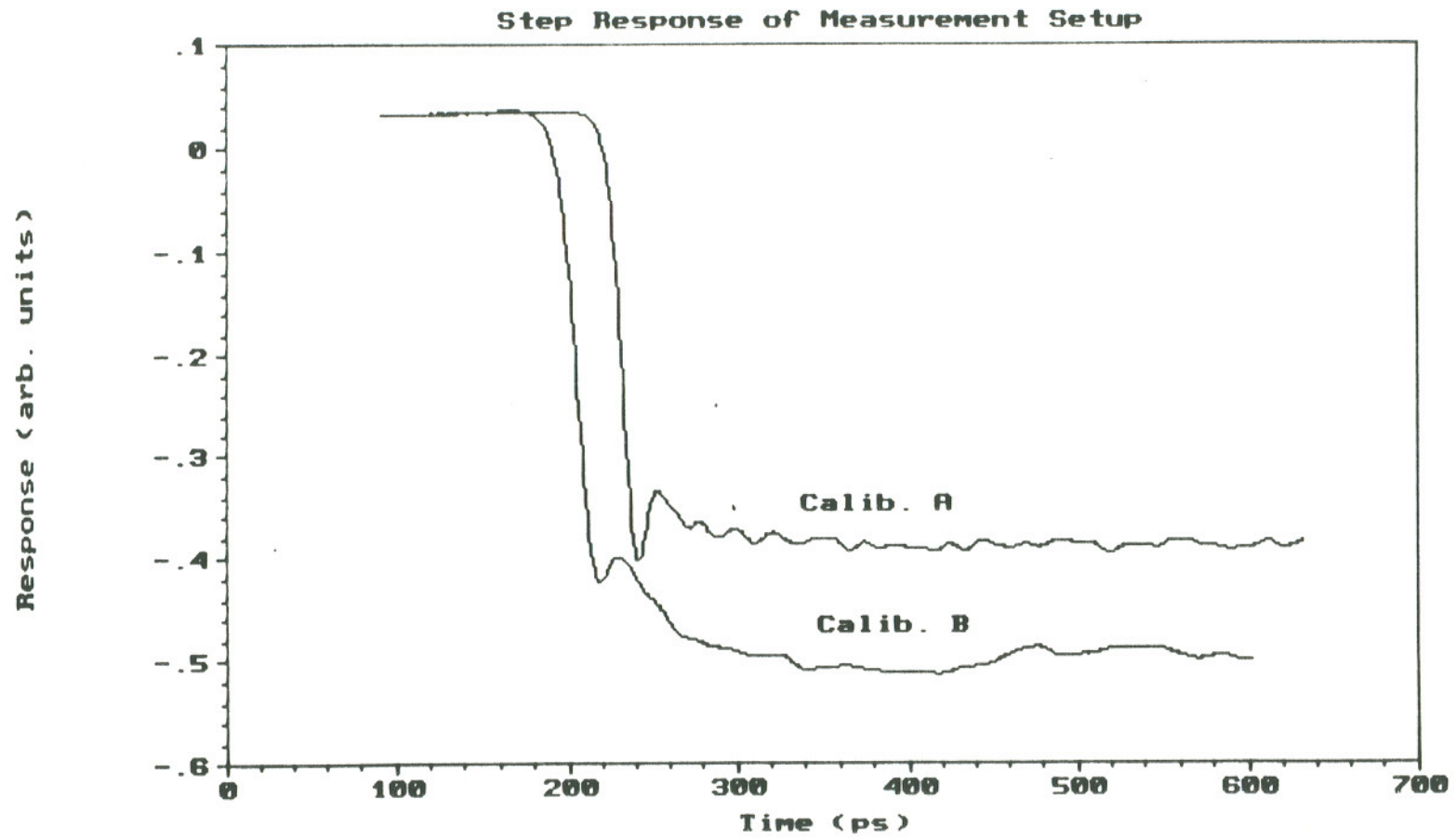


Figure 6.2. Step response of the measurement setup obtained by using two different calibration step generators [87].

layer (PIN-D). The histograms of the dark currents are plotted in figures 6.3-7.6. One distinctive feature of dark current values of PIN-D which was also observed in PIN-E is that a large number of devices with $17\mu\text{m}$ diameters had higher dark currents compared with $27\mu\text{m}$ diameter devices. Since the opposite relation is expected it is important to compare this trend in wafers grown with an InP buffer layer (PIN-A and PIN-C). The value of the dark current when the InGaAs layer is depleted depends on two main factors. The first one is the generation-recombination in the intrinsic layer and at the interfaces. The second source of dark current is the surface current through the mesa walls. The relative contribution of these two mechanisms can be estimated by comparing devices with different diameters since the first one is proportional to the area and the second one is proportional to the circumference of the fabricated mesas. The dark current histograms of PIN-A gives some insight on this matter. The histogram of $27\mu\text{m}$ devices indicate a lognormal distribution as would be expected in most process related random variables. Since a similar distribution is expected from $17\mu\text{m}$ diameter devices, the distribution of the $17\mu\text{m}$ devices can be interpreted as superposition of two lognormal distributions. Although, the large variance in the data prevents one to statistically confirm this hypothesis, the increase in the variation of dark current values from 20% (PIN-A-27) to 76% (PIN-A-17) supports this possibility. To determine the major cause of anomalous distributions and high values of dark current observed in $17\mu\text{m}$ devices, both the material parameters and the process related issues should be

considered. The epilayers have been characterized by XRDCD rocking curve analysis to be of high quality. This is also confirmed by the overall performance of the fabricated devices. The spatial variations (non-uniformity) in the epilayer quality can be considered but is very unlikely, since the non-uniformities due to growth conditions would effect the devices regardless of the diameter. Another distinctive feature of the spatial variations in the epilayer quality due to OMVPE growth is that the non-uniformity would increase gradually either in horizontal or vertical direction with respect to the gas flows. This is inconsistent with the spatial distribution of the devices with high dark currents that we have observed. Hence the variations of the dark current values of these devices are probably due to variations in lithography process. The large sample variance of dark currents given in Table 6.1 independent of device diameter also indicate that the lithography process is the most significant factor in achieving low dark currents in PIN mesa photodetectors. One important aspect in the fabrication of mesa photodetectors related to the dark current is the passivation of the mesa walls. The reduction of the dark current in InGaAs/InP mesa devices by passivation of InGaAs with $\text{H}_2\text{SO}_4:\text{H}_2\text{O}_2:\text{H}_2\text{O}$ (1:1:X) (Caro's etch) has already been reported [88]. Since in actual device fabrication this step is followed by further processing, a comprehensive study on the combination of treatments used in device processing is essential to understand the chemistry of the passivated InGaAs surface. Such an investigation was undertaken where an x-ray photoelectron spectroscopy (XPS) analysis was used to

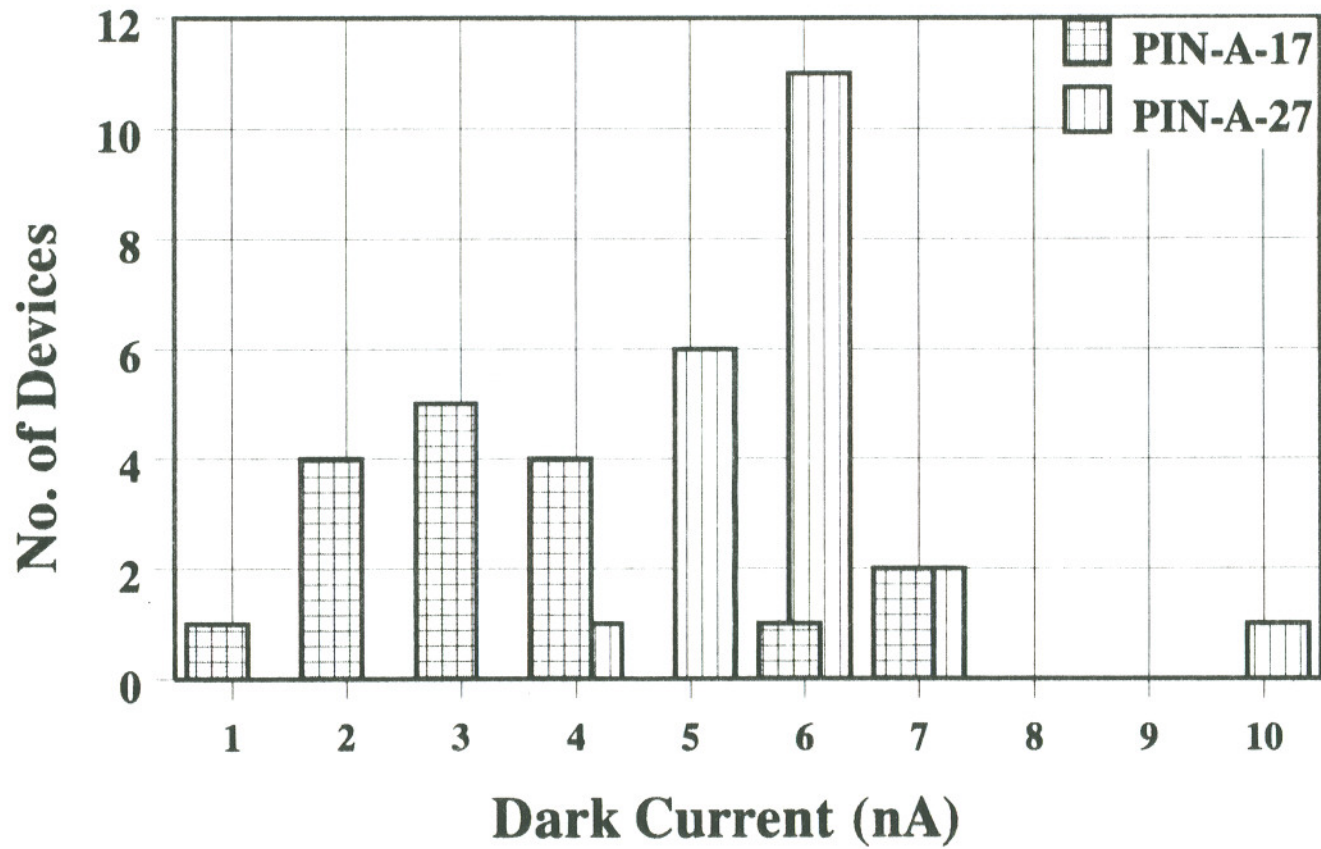


Figure 6.3. Dark current histograms of tile PIN-A measured at 30kV/cm.

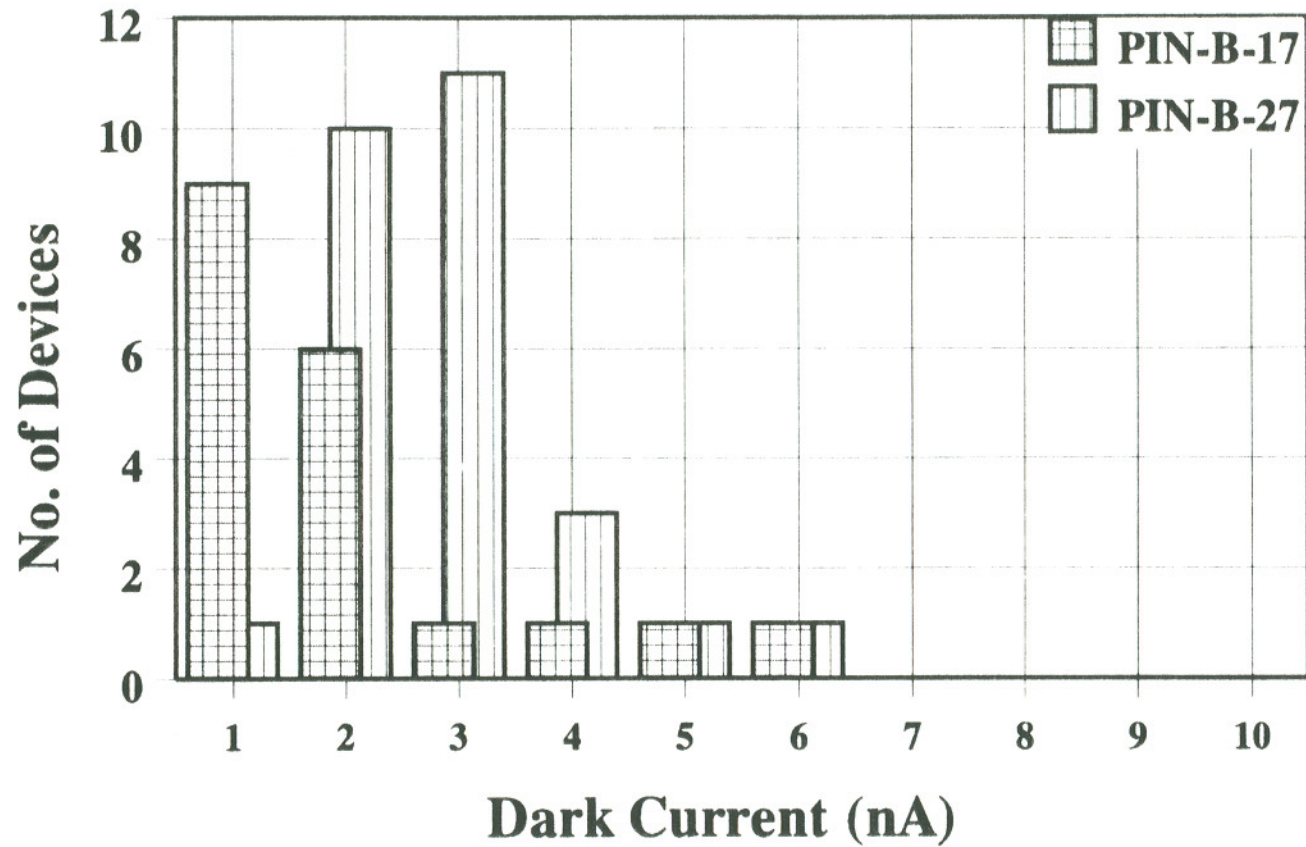


Figure 6.4. Dark current histograms of tile PIN-B measured at 30kV/cm.

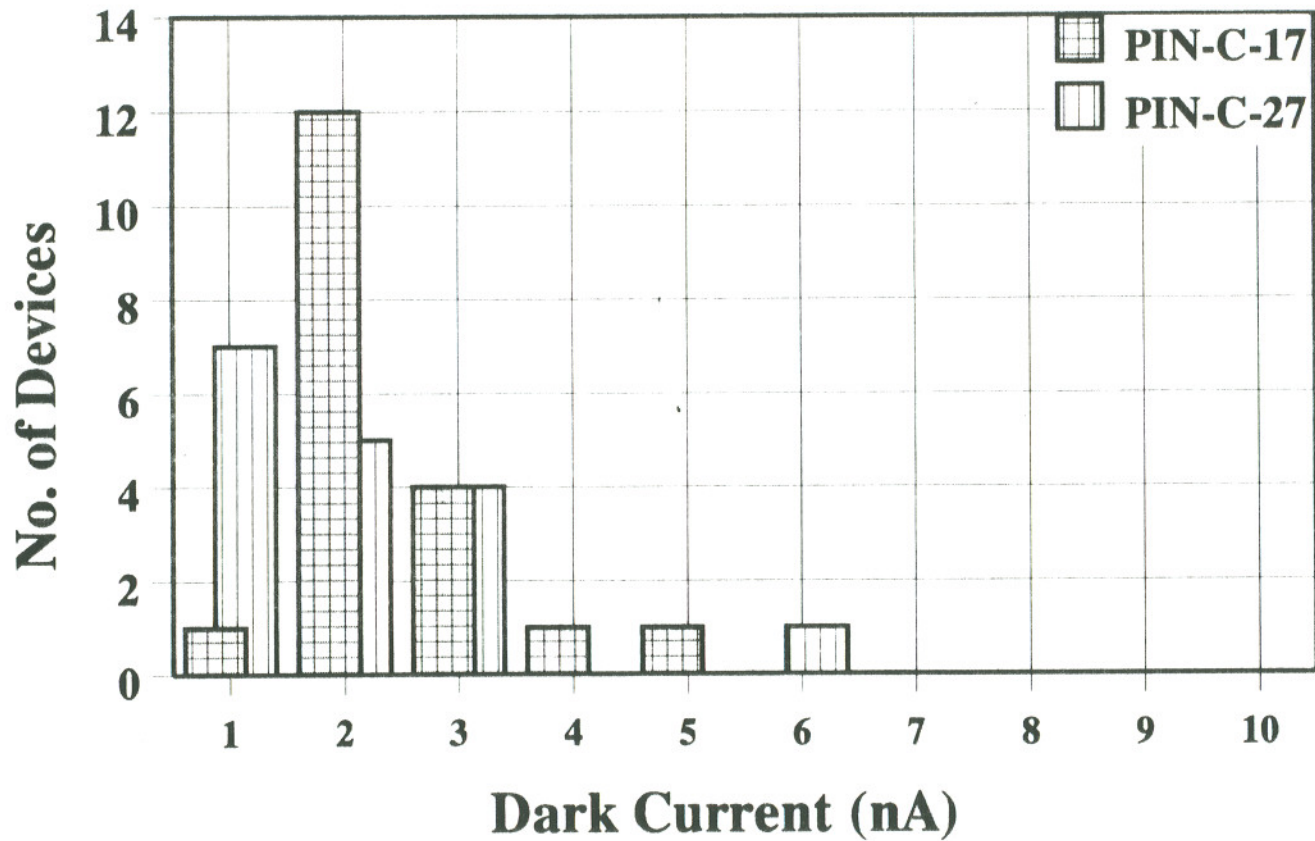


Figure 6.5. Dark current histograms of tile PIN-C measured at 30kV/cm.

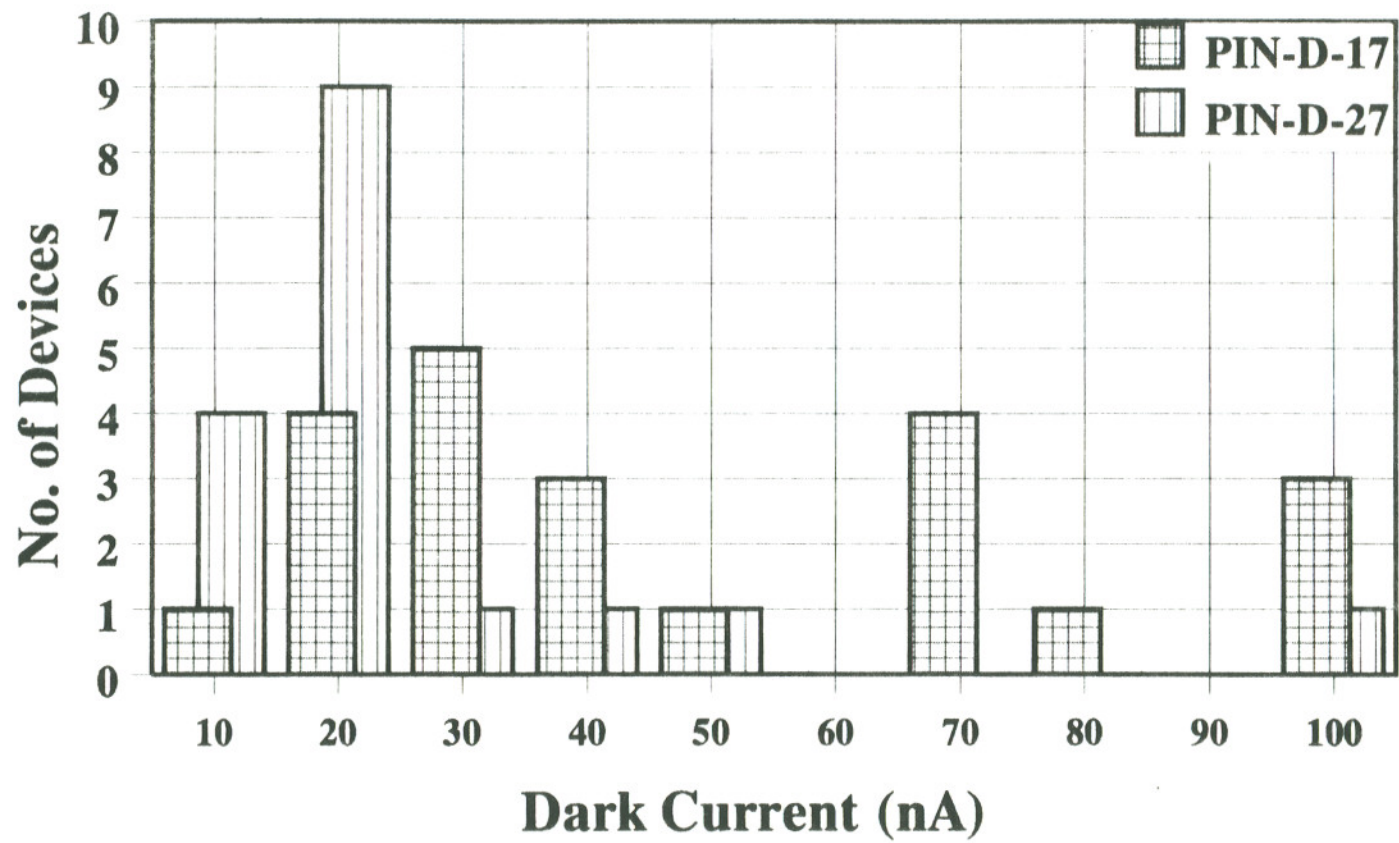


Figure 6.6. Dark current histograms of tile PIN-D measured at 30kV/cm.

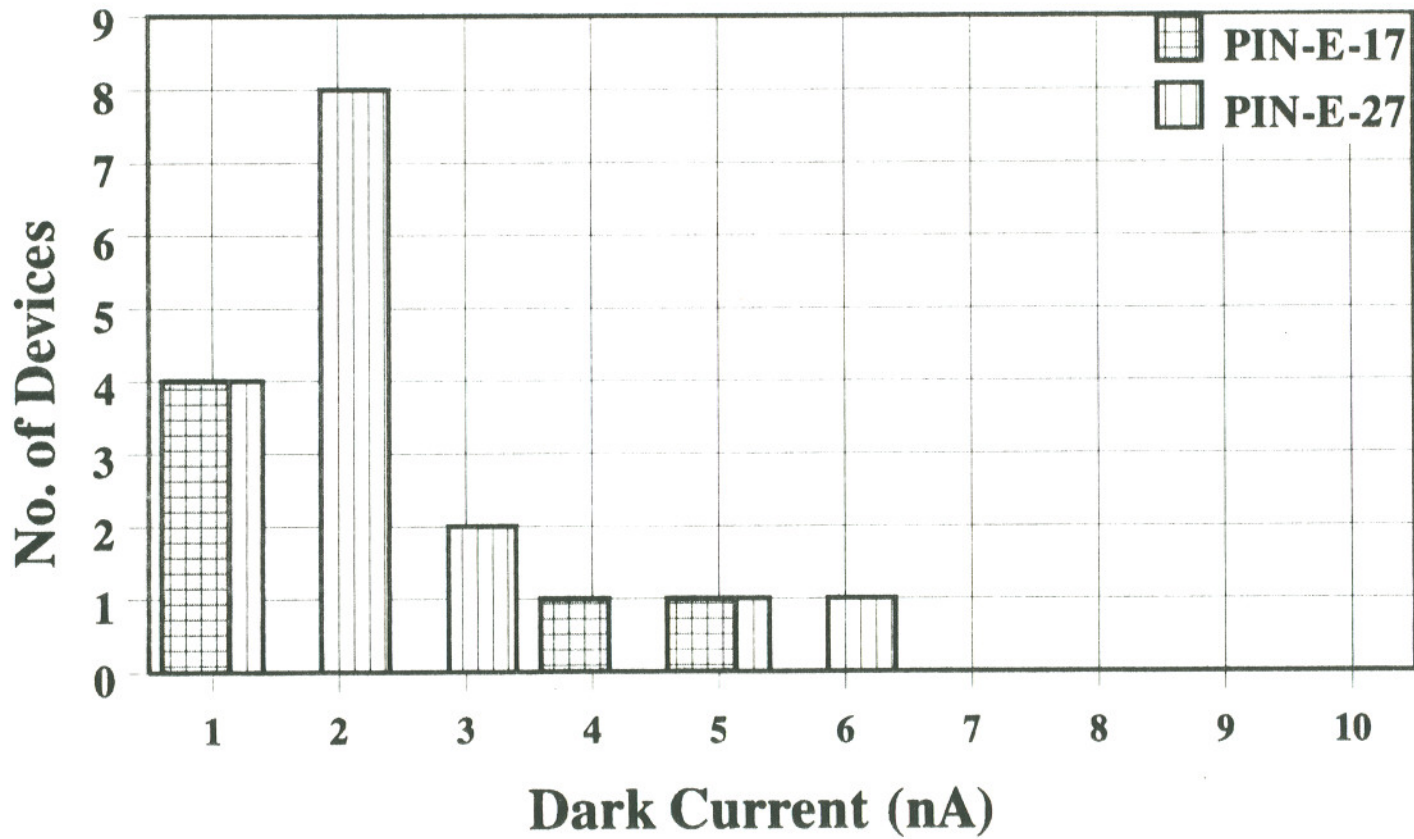


Figure 6.7. Dark current histograms of tile PIN-E measured at 30kV/cm.

determine the InGaAs surface chemistry after various chemical treatments commonly used in InGaAs/InP device processing. This study clearly showed that surface concentration of indium oxide, which is commonly cited as the cause of surface leakage in InGaAs is unchanged by Caro's etch, while the surface atomic concentration of both the arsenic and oxygen increased with this treatment. These results are different from the previous conclusions reported in literature regarding the cause of the reduction in dark current by the passivation of the InGaAs surfaces using Caro's etch. These results will be published separately[89].

6.4 Spectral Response

The InGaAs/InP PIN photodetectors are ideal to be used at both 1300nm and 1550nm optical transmission windows of the optical fibers. The responsivities at both 1300nm and 1550nm have to be taken into account in evaluating the tradeoff between the 3dB bandwidth and quantum efficiency of these devices. The spectral responses of photodetectors with different absorbing layer thicknesses are plotted in figure 6.8. The quantum efficiency surface scans of the fabricated photodetectors with different diameters is also plotted in figures 6.9-6.12 at 1300nm and 1550nm. It is clearly seen from the comparison of spectral responses of PIN-C, PIN-A, and PIN-B in figure 6.8 that the responsivity at 1550nm drops faster than at 1300nm as the thickness of the absorbing layer is reduced from $0.9\mu\text{m}$ to $0.2\mu\text{m}$. The electron-hole generation rate in

the absorbing InGaAs layer is given by equation 6-1 [67].

$$G_E(x) = \Phi_o \alpha e^{-\alpha W} \quad (6-1)$$

where α is the absorption coefficient, W is the absorbing layer thickness, and Φ_o is the incident flux per unit area. For the PIN photodetectors with thin InGaAs absorbing layers (PIN-B) the value of absorption coefficient is the major factor in determining the spectral response. A detailed analysis of responsivity of PIN photodetectors can be found in [67] for linearly varying electric field. To accommodate the discontinuity at the heterojunction the generation rate has to be incorporated into equations 4-28 and 4-29. In comparing the responsivities at 1300nm and 1550nm, the energy distributions of the generated carriers within the energy bands have to be considered. The implications of different carrier distributions that correspond to the same quasi-Fermi level is discussed in detail in reference 68. The difference in the energies of the electrons also have to be considered in the transport calculations. The higher energy electrons generated at 1300nm will have higher probability of scattering into the L valley than at 1550nm for which most of the electrons will be close to the conduction band minima. The conduction band discontinuity and the transfer of electrons to the L valley will affect the transport of electrons across the heterojunction depending on the energy of the electrons. Simulation of the carrier transport in PIN photodetectors will be discussed together with high speed measurements of these devices in the next section.

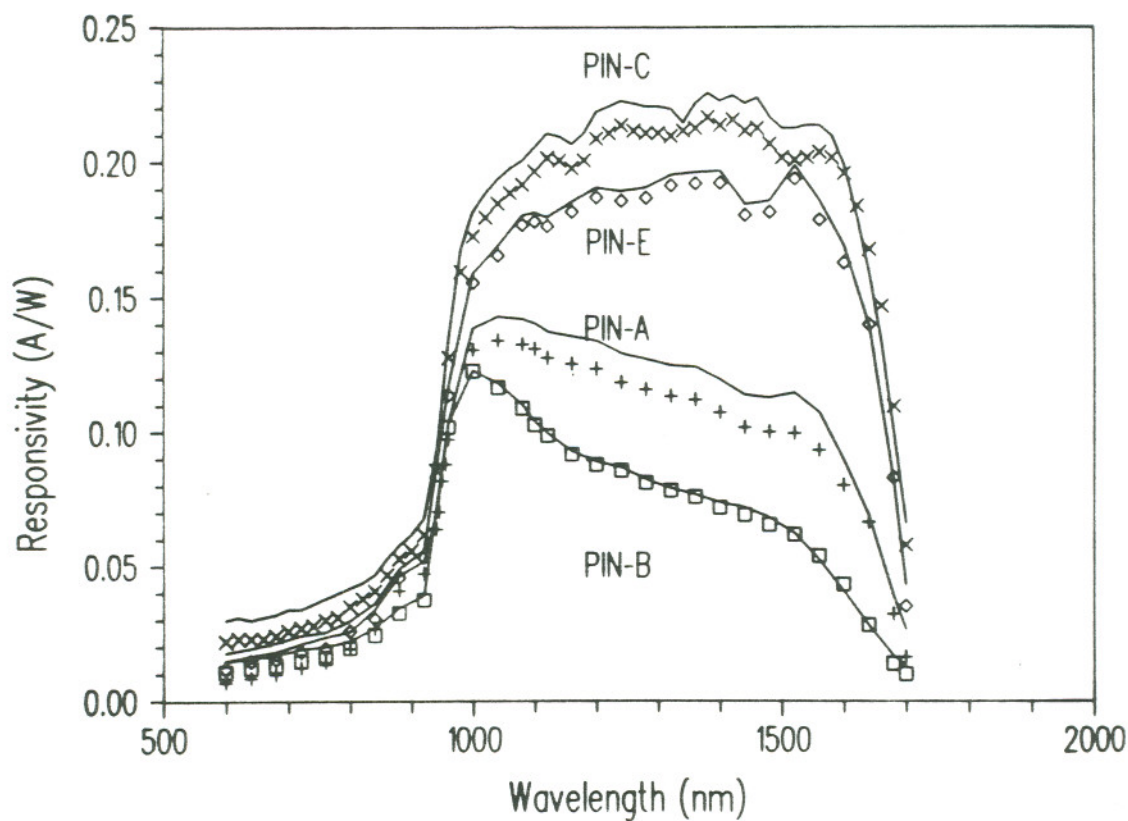


Figure 6.8. External responsivity of the photodiodes with $27\mu\text{m}$ diameters plotted without area correction measured by a $50\mu\text{m}$ core diameter fiber aligned approx. $25\mu\text{m}$ above the devices. The solid lines represent the responsivity at 30kV/cm corresponding to PIN-A,B,C, and E as indicated on the plot. The responsivity at 0V bias is also plotted for PIN-A (+), PIN-B (\square), PIN-C (x), and PIN-E (\diamond).

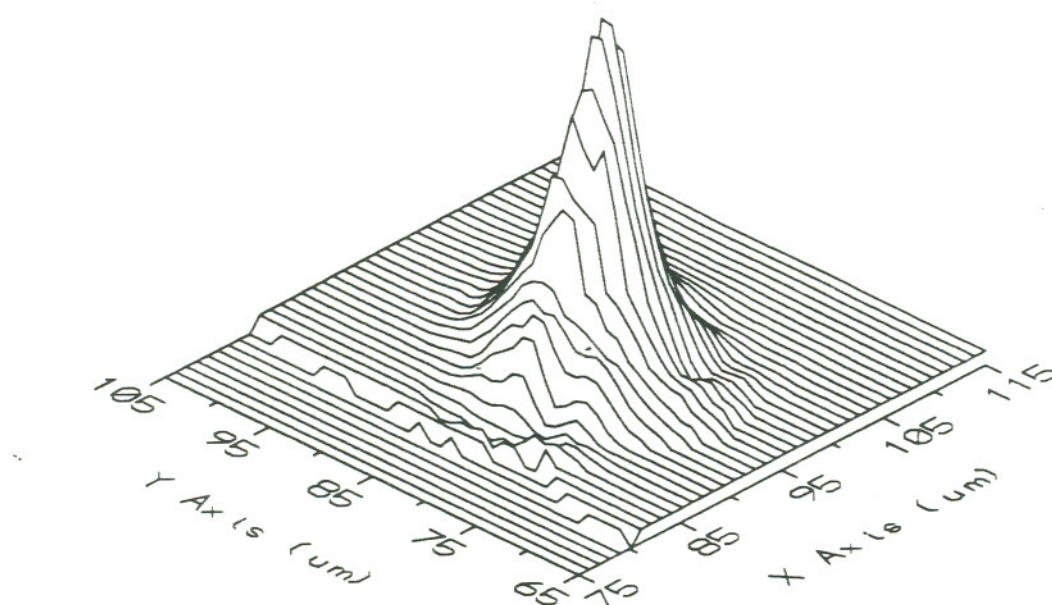


Figure 6.9. Quantum efficiency surface of PIN-C-17 at 1300nm, with 0.9 μm thick InGaAs absorbing layer and device diameter of 17 μm .

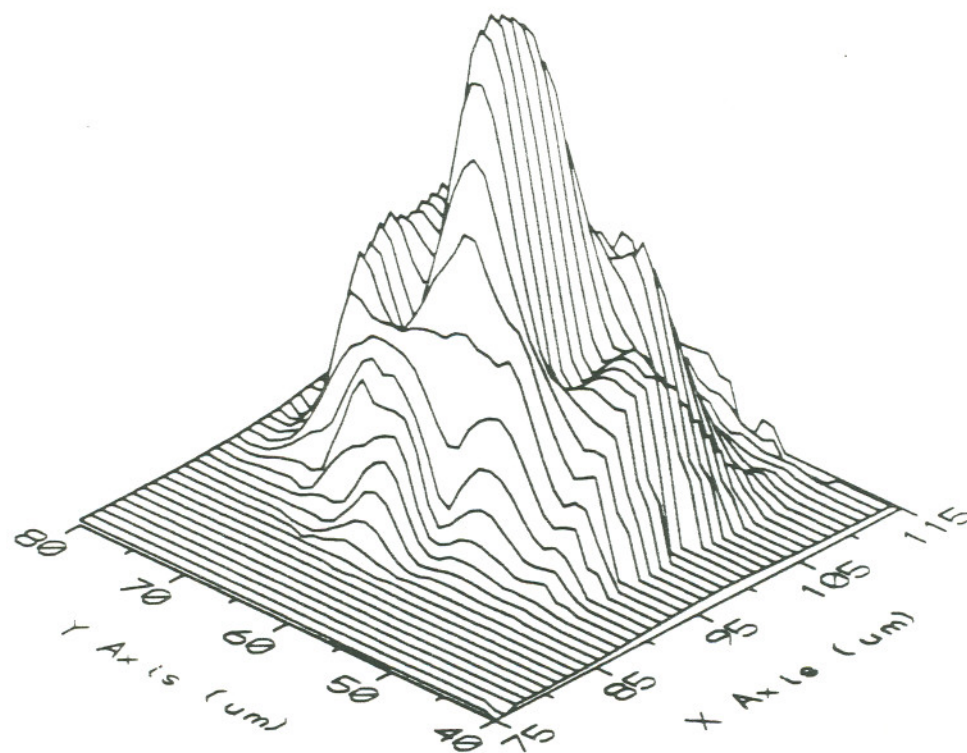


Figure 6.10. Quantum efficiency surface of PIN-C-27 at 1300nm, with 0.9 μm thick InGaAs absorbing layer and device diameter of 27 μm .

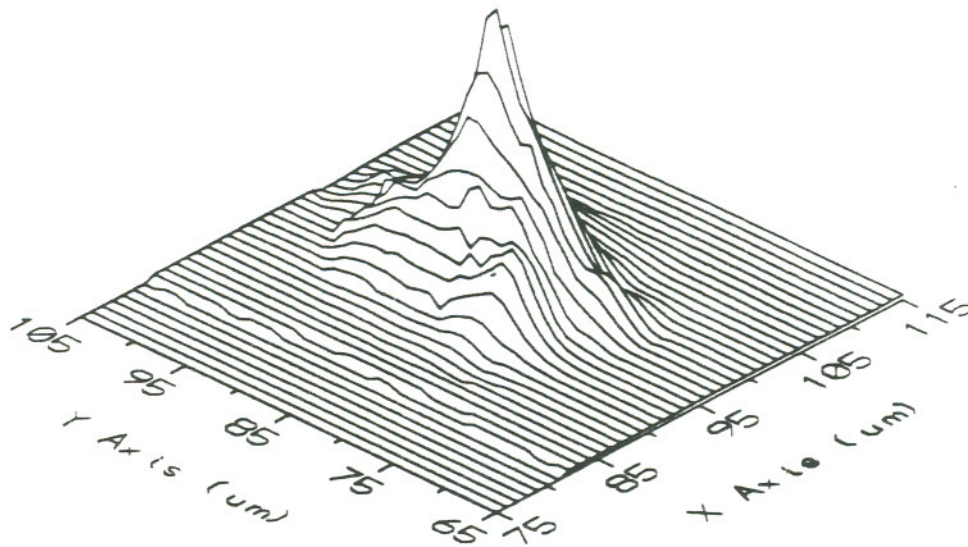


Figure 6.11. Quantum efficiency surface of PIN-C-17 at 1550nm, with 0.9 μm thick InGaAs absorbing layer and device diameter of 17 μm .

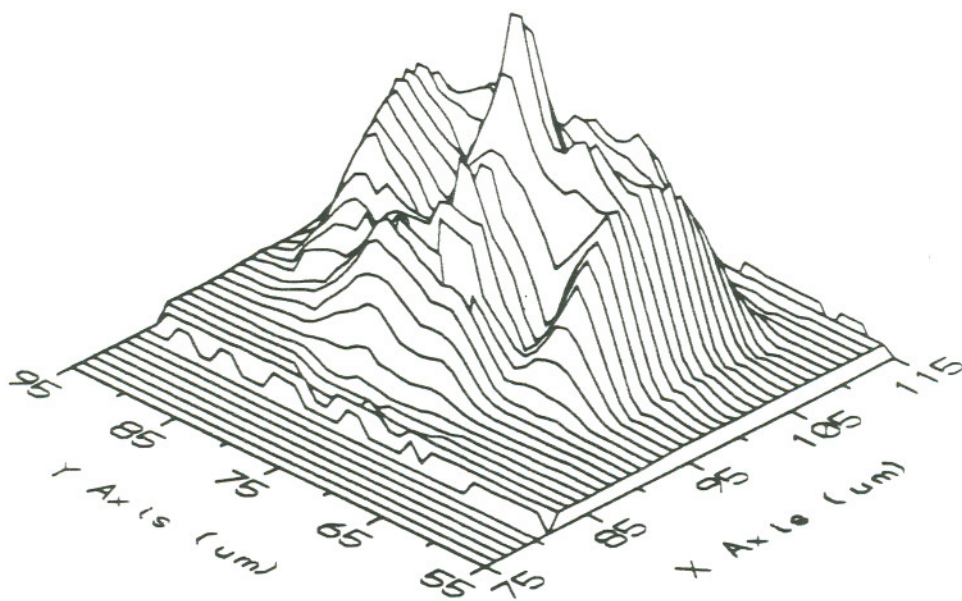


Figure 6.12. Quantum efficiency surface of PIN-C-27 at 1550nm, with 0.9 μm thick InGaAs absorbing layer and device diameter of 27 μm .

The responsivity of double-heterostructure PIN photodetectors have a distinctive absorption spectra defined by the bandgap of the top contact and window layer (in this case InP), and the bandgap of the absorbing layer (InGaAs). In these devices, we have incorporated a very thin (100nm) InGaAs top contact layer to reduce the p^+ contact resistance. This is especially important for devices with thin i layers (PIN-B), since the RC time constant is most significant in these devices. The responsivity of PIN-B at 1550nm could be improved by selectively removing this top p^+ InGaAs layer. For all these devices the responsivity drops sharply at around 940nm corresponding to the bandgap of InP. To improve the responsivity at shorter wavelengths the thickness of the top InP layer could be reduced. This would require high p^+ doping of InP to achieve full depletion in the center of the mesa. The number of dopants that have been successfully used in OMVPE growth of InP is limited and carrier concentration higher than $5 \times 10^{18} \text{cm}^{-3}$ is unlikely. We have used Mg as the p-type dopant, since it has a much lower diffusivity than Zn and a higher saturation level than Cd [90].

The comparison of the responsivities of devices grown with (PIN-C) and without (PIN-E) an undoped InP buffer layer shows a significant difference, as can be seen in figure 6.8. This might be an indication of higher carrier lifetime and longer diffusion length in devices grown with a buffer layer due to improved epilayer quality and reduction in the diffusion of dopants from the substrate during OMVPE growth. This phenomena has been studied in undoped InGaAs layers grown on Fe doped semi-

insulating InP substrates and is discussed in Chapter 3. The comparison of the responsivities measured at zero bias and at 30kV/cm in figure 6.8, indicates a larger difference for devices grown with a buffer (PIN-A and PIN-C). This comparison supports our conclusion that, the incorporation of a thin undoped InP buffer layer underneath the InGaAs absorbing layer results in a lower background impurity concentration and a higher minority carrier lifetime, improving the device performance. We will also show in the next section that a thin undoped buffer layer does not result in degradation in high speed performance of these devices. The fastest impulse response was measured on devices with the InP buffer layer (PIN-A) and no tailing in the impulse response was observed when the device was depleted, indicating no appreciable amount of charge trapping takes place at the interfaces.

The background impurity concentration in the intrinsic InGaAs layer can be estimated from the CV measurements. A first order approximation for the depletion width can be obtained directly from the CV measurements using space-charge approximation. The depletion width of PIN-A and PIN-D is plotted in figure 6.13 as a function of reverse bias, using 1.06pF/cm as the value for the dielectric constant. At zero bias voltage the lower depletion width values of the device grown without the InP buffer layer (PIN-D) can be associated with a higher background concentration.

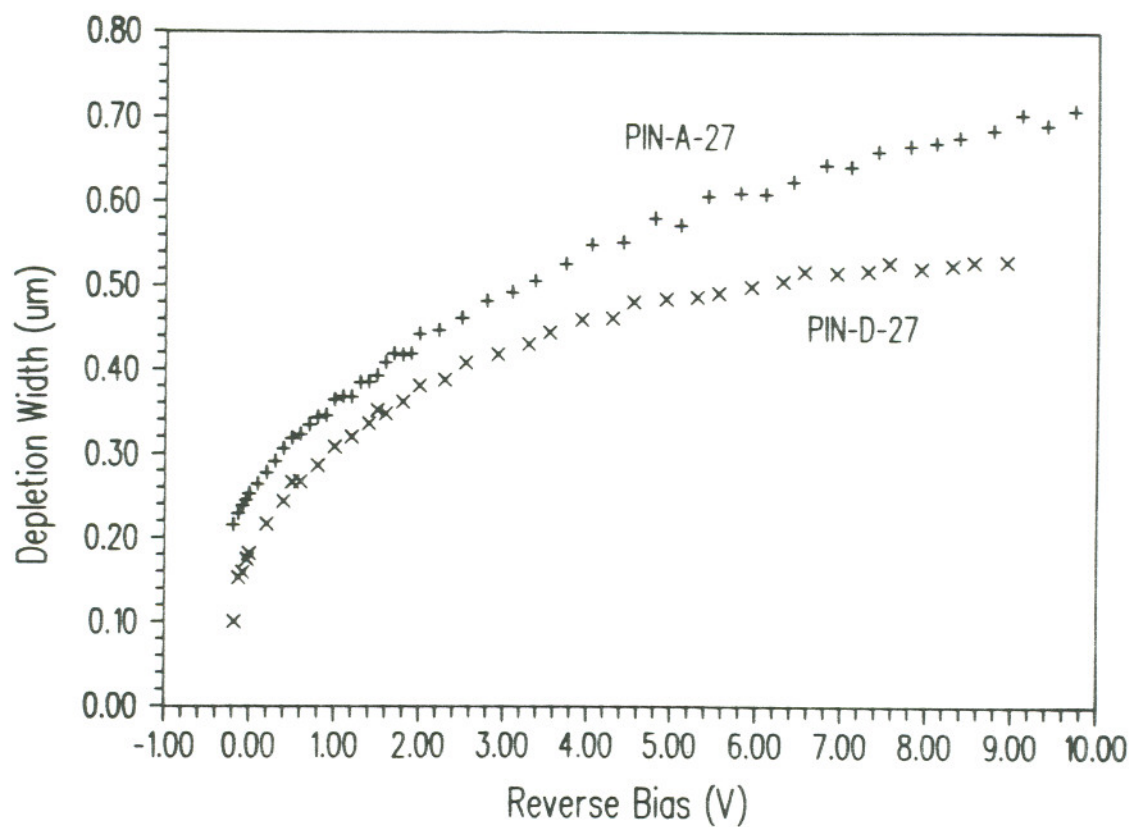


Figure 6.13. Depletion width as a function of applied bias of PIN-A-27(+) and PIN-D-27(x), calculated from the capacitance-voltage measurements.

Although this would explain the higher dark currents and lower responsivities observed in these devices, we would like to point out that the accumulation of electrons at the isotype heterojunction also results in increased value of the measured capacitance. The effect of accumulated charges at the heterojunctions in calculation of the band structure and the depletion width has been discussed in chapter 5.

6.5 High Speed Response

In the design of high speed PIN photodetectors, RC time constant and the transit time across the depleted region are the two basic factors that have to be considered. For a given device diameter of $17\mu\text{m}$, the optimum InGaAs layer thickness can be estimated to be $0.5\mu\text{m}$ [2]. The InGaAs layer thickness of $0.2\mu\text{m}$ was chosen to demonstrate the capacitance limited high speed response and to measure the responsivity for considerations in fabrication of smaller diameter devices. The InGaAs layer thickness of $0.9\mu\text{m}$ was chosen to observe the transit time limited high speed response and to achieve improved responsivity with higher gain-bandwidth product. The $0.9\mu\text{m}$ InGaAs layer thickness is also close to optimum value for devices with $27\mu\text{m}$ diameter. The results of the high speed response measurements of all the fabricated photodetectors are summarized in Table 6.2 together with the responsivities at 1300nm and 1550nm. The estimated value of the FWHM after deconvolution is also given as a first order comparison. A more accurate, time domain deconvolution of the photoresponse from

the measured impulse response is discussed below.

The frequency response of a PIN photodiode has been discussed in the well-known paper of Lucovsky et.al. [91]. Recently, an analytical time domain impulse response function has been formulated which extends the solutions to incorporate the effects of drift, diffusion, recombination, and absorption [92]. In InGaAs/InP PIN photodiodes the diffusion and recombination in the i layer plays an important role at low bias voltages when the i (InGaAs) layer is not fully depleted. The measured impulse responses of the fabricated photodiodes (PIN-A to C) are plotted in figures 6.14-6.16 for three different InGaAs layer thicknesses as a function of applied biases. The role of three major mechanisms that affect the impulse response of PIN photodiodes, namely, the transit time, RC time constant, and the diffusion from the undepleted InGaAs (at low bias voltages) can easily be identified in these figures. The effect of RC time constant is most significant in devices with thin InGaAs layers and large diameters (PIN-B-27), and it can be seen in figure 6.15 that at high applied biases, the response is an exponentially decaying tail. The impulse response of PIN-A and PIN-C at high applied bias voltages are similar except for the width of the pulse, which is wider for PIN-C due to transit time of the carriers through the i layer. The response of both PIN-A and PIN-C at zero bias shows a long tail due to the diffusion of generated carriers in the InGaAs layer. This tail disappears at a bias voltage of 0.75V for PIN-A and 2V for PIN-C, when the InGaAs layer is depleted.

Table 6.2. Summary of responsivity and high speed measurements.* Using a fiber with 50 μm core diameter (No area correction)

Device Run#	As Measured* Responsivity (A/W) { 27 μm diam.} 1300nm 1550nm		t(fwhm) _{meas} ($\pm 0.2\text{ps}$) 17 μm 27 μm		t(fwhm) _{est} ($\pm 1.0\text{ps}$) 17 μm 27 μm	
	PIN-A	0.126	0.110	16.8	18.1	9.5
PIN-D	0.122	0.102	18.3	19.2	11.0	12.5
PIN-B	0.081	0.055	18.7	20.6	11.5	14.5
PIN-C	0.221	0.214	18.2	18.9	11.0	12.0
PIN-E	0.193	0.190	18.1	18.0	11.0	11.0

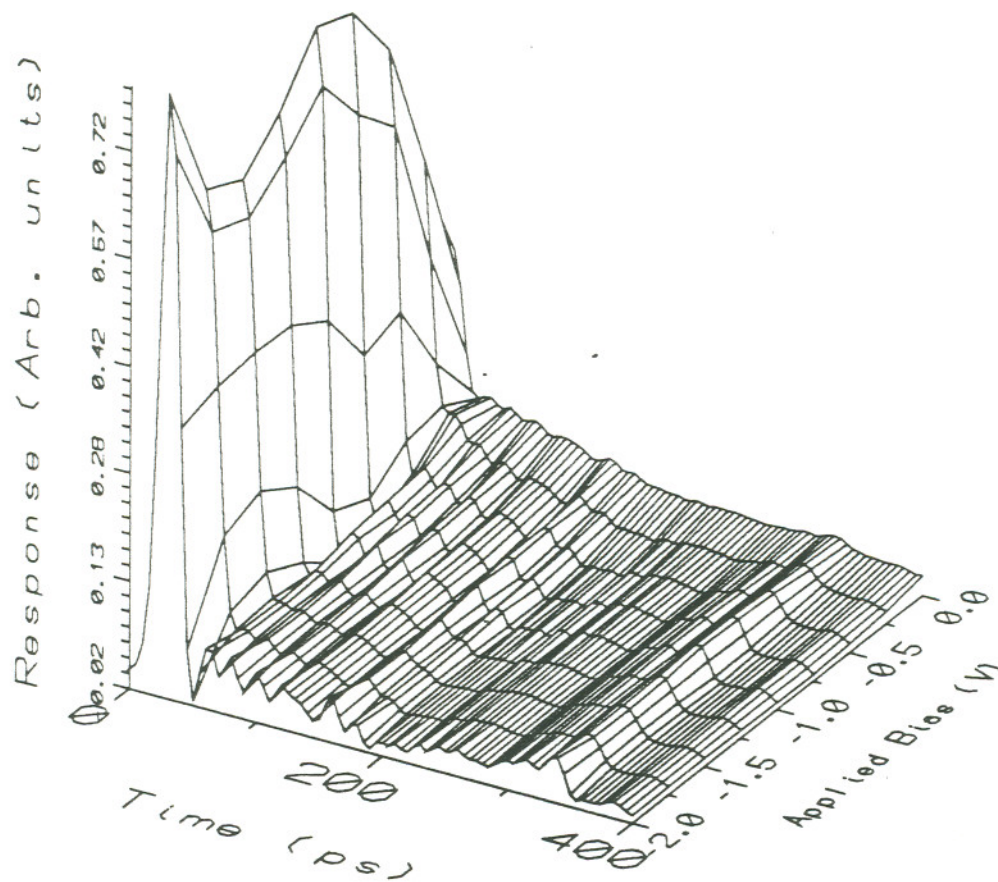


Figure 6.14. Measured response of PIN-A-17 as a function of applied bias. The 3D surfaces are obtained by interpolating the measurements in the direction of applied bias.

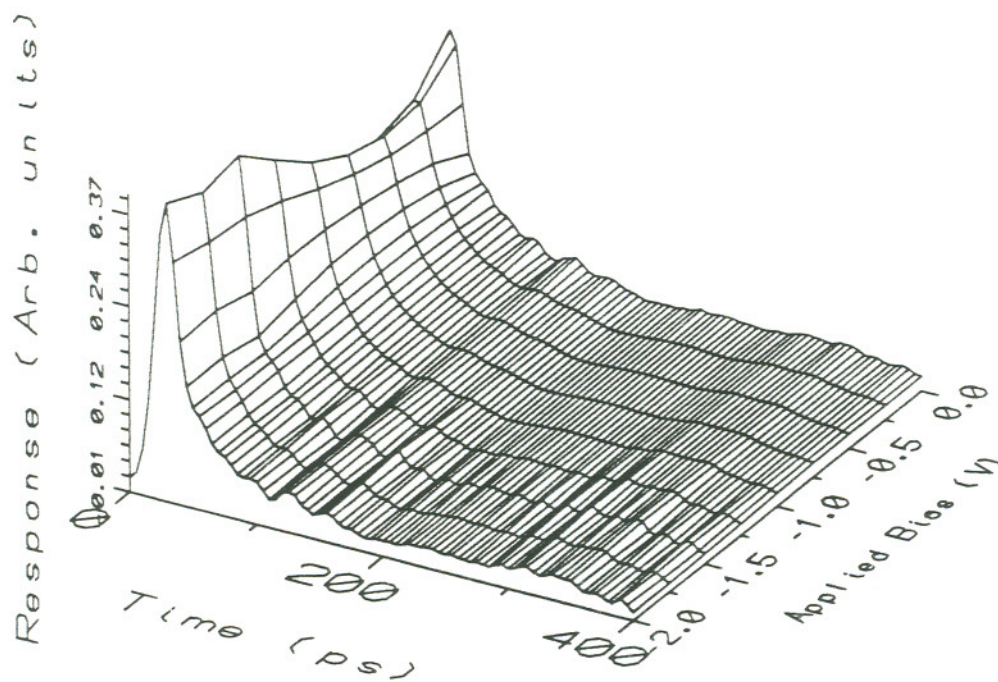


Figure 6.15. Measured response of PIN-B-17 as a function of applied bias. The 3D surfaces are obtained by interpolating the measurements in the direction of applied bias.

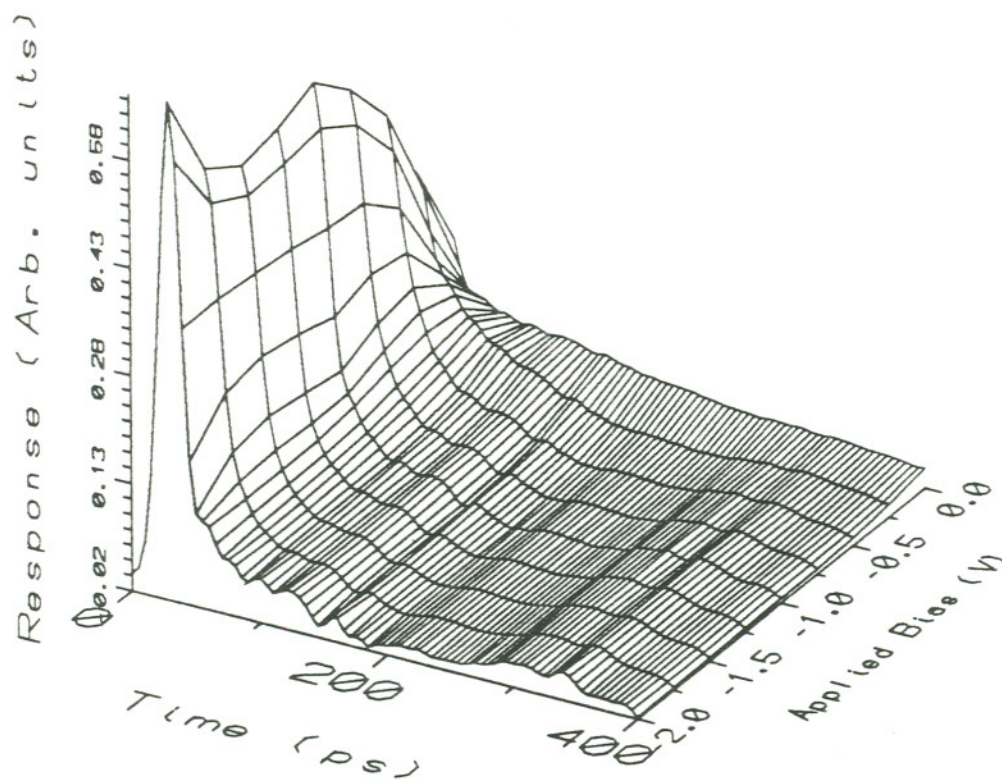


Figure 6.16. Measured response of PIN-C-17 as a function of applied bias. The 3D surfaces are obtained by interpolating the measurements in the direction of applied bias.

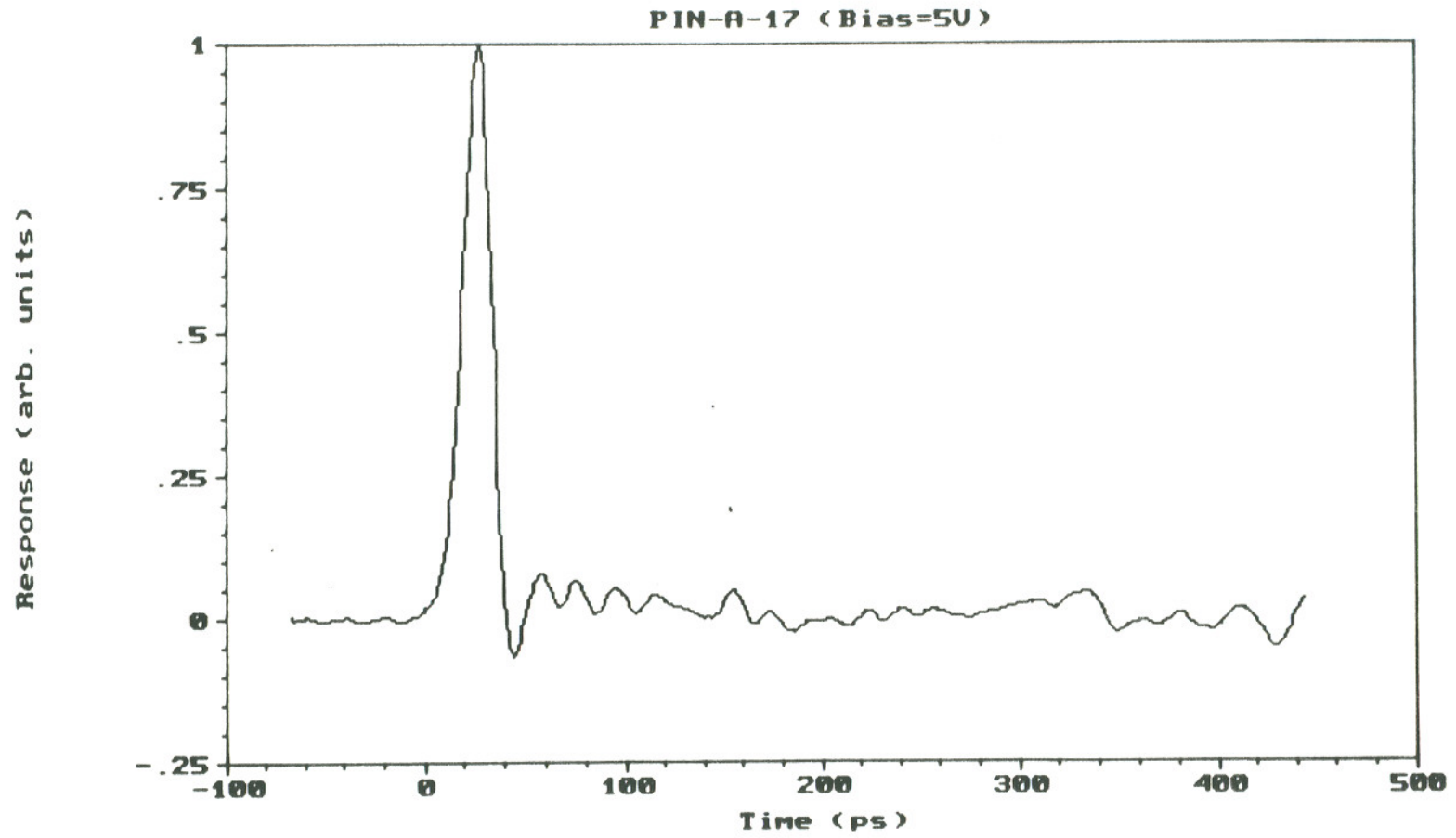


Figure 6.17. Sampling scope trace of the response of PIN-A-17 at -5V applied bias.

The measured response of PIN-A-17 is plotted in figure 6.17 at 5V bias. The absence of a tail indicates that there is no charge trapping at the heterointerfaces. The response of the device to the incident laser pulse was calculated by deconvolving the step response of the measurement setup. The system response is taken as the average of the two responses given in figure 6.2. The error in deconvolution is also calculated by using the two system responses to be the upper and lower limits. Since the measured step response of the measurement setup varied significantly with two different calibration step generators, the deconvolution of the measured photodiode response was calculated as the best estimate of the actual data. We should point out that the actual time domain measurements of these devices with 1ps sampling period has not been previously reported. The noise considerations in these measurements differ from electro-optic sampling [93,94], where correlation of the pulse source and delayed measurement is averaged at low repetition rates. An estimation based approach of deconvolution has already been developed for seismic signal processing and is discussed in reference 95. Following the notation in reference 82 the convolution model can be written as a linear system as given in equation 6.2.

$$\begin{array}{c}
 \left[\begin{array}{c} z(N) \\ z(N-1) \\ \cdot \\ \cdot \\ z(n) \\ \cdot \\ \cdot \\ z(2) \\ z(1) \end{array} \right] = \left[\begin{array}{cccc} u(N-1) & u(N-2) & \cdot & \cdot & u(N-n) \\ u(N-2) & u(N-3) & \cdot & \cdot & u(N-n-1) \\ \cdot & \cdot & \cdot & \cdot & \cdot \\ \cdot & \cdot & \cdot & \cdot & \cdot \\ u(n-1) & u(n-2) & \cdot & \cdot & u(0) \\ \cdot & \cdot & \cdot & \cdot & \cdot \\ \cdot & \cdot & \cdot & \cdot & \cdot \\ u(1) & u(0) & 0 & \cdot & 0 \\ u(0) & 0 & 0 & \cdot & 0 \end{array} \right] \times \left[\begin{array}{c} h(1) \\ h(2) \\ \cdot \\ \cdot \\ \cdot \\ \cdot \\ \cdot \\ \cdot \\ h(n) \end{array} \right] + \left[\begin{array}{c} v(N) \\ v(N-1) \\ \cdot \\ \cdot \\ v(n) \\ \cdot \\ \cdot \\ v(2) \\ v(1) \end{array} \right]
 \end{array}$$

(6-2)

where measured response of the photodiode define $z(1 \rightarrow N)$, the measurement setup response are used in $u(1 \rightarrow N)$, and the coefficients of the impulse response of the diode are given by $h(1 \rightarrow n)$. The additive measurement noise is incorporated into the system by $v(1 \rightarrow N)$. The rank of the system matrix in equation 1 was reduced by singular value decomposition [73,96], and the diode response was calculated using the pseudo inverse of the system matrix obtained using the singular values above the determined noise level. An extensive discussion on the distortion introduced by the rank reduction and other aspects of reduced signal processing can be found in reference 96. The measured and deconvolved response of PIN-A-17 is given in figures 6.18 and 6.19 for applied biases of -5V and 0V respectively. The error bars reflect the indeterminacy in the measurement system response as determined by the two step response measurements

plotted in figure 6.2. The deconvolved signal obtained from the estimated system response is given by the block squares. The scattering of the deconvolved data in figure 6.18 compared to the moving average (solid line) can be attributed to the deconvolution noise. This distortion due to deconvolution is more significant in figure 6.18 compared to 6.19, because the bandwidth of the measured response is close to the estimated measurement system response. We believe that the deconvolved data given in figures 6.18 and 6.19 are accurate representations of the photodiode response to the incident laser pulse with 3.8ps FWHM. A first order calculation can be performed for comparison by considering the transit time of the carriers [91], and the RC time constant using the measured capacitance. This comparison is plotted in figure 6.20 for the response of PIN-A-17 at 5V bias. The agreement between the FWHM of the deconvolved data and the calculated response in figure 6.20 indicate that the response of the fabricated devices are mainly determined by the carrier transport across the InGaAs layer. The drift velocities of electrons and holes are taken to be 7×10^6 cm/s and 5×10^6 cm/s, respectively. The measured capacitance of the device is 100fF at 5V bias. The calculated response is convolved with the laser pulse and plotted in figure 6.20, together with the deconvolved data using the average measurement setup response. The FWHM of the calculation can be adjusted by changing the drift velocity values used in the calculations, however the exponential tail is due to the RC time constant and can not be adjusted as a fitting parameter. The difference in the tail of the response of the

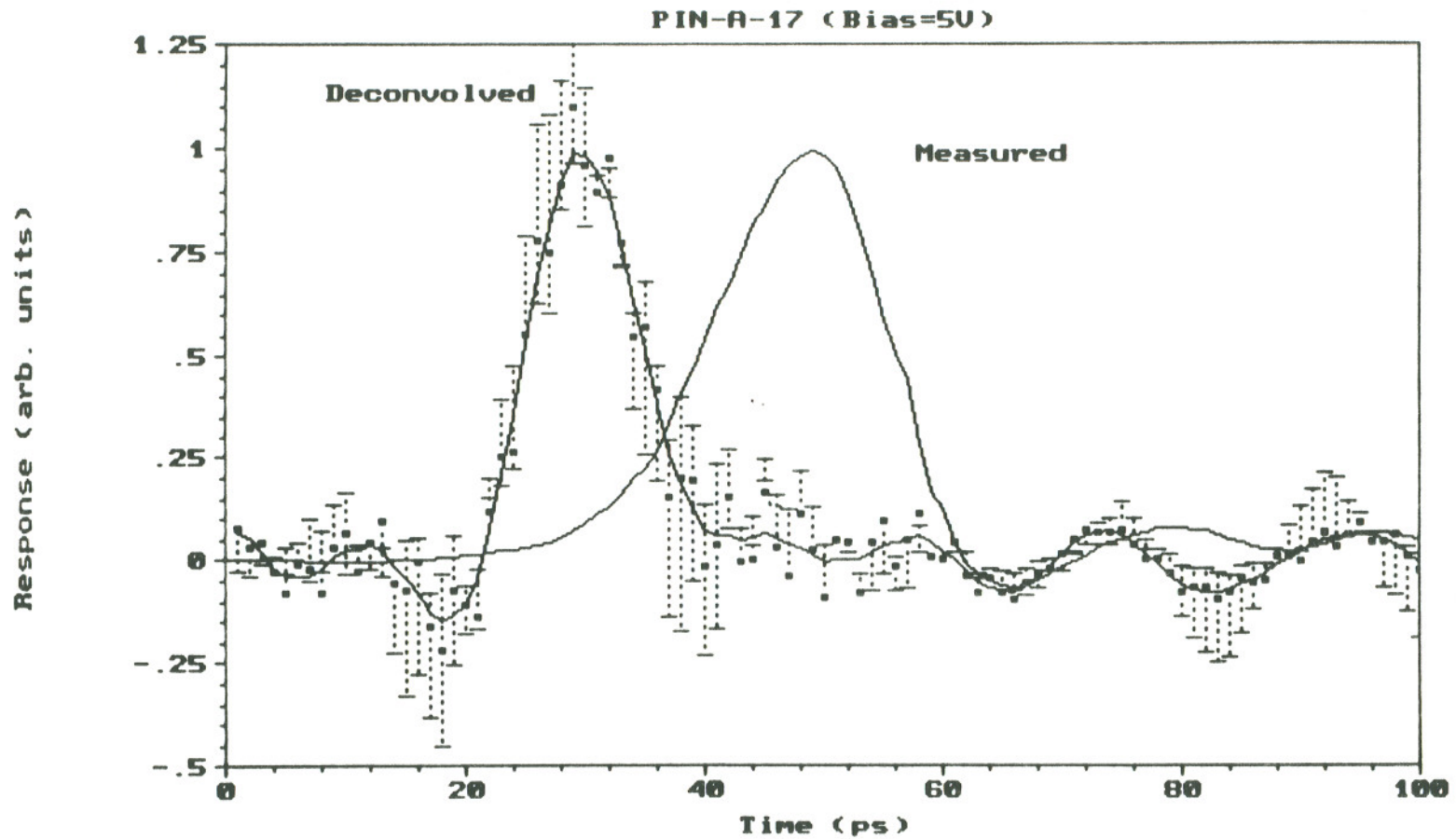


Figure 6.18. Measured and deconvolved response of PIN-A-17 at -5V applied. The measured response is given by the solid line. The deconvolved data is plotted as (■) with the moving average of the points plotted as the line passing through the points. The error bars are obtained by plotting the deconvolved data using the two measured step response of the measurement setup as the upper and lower limits.

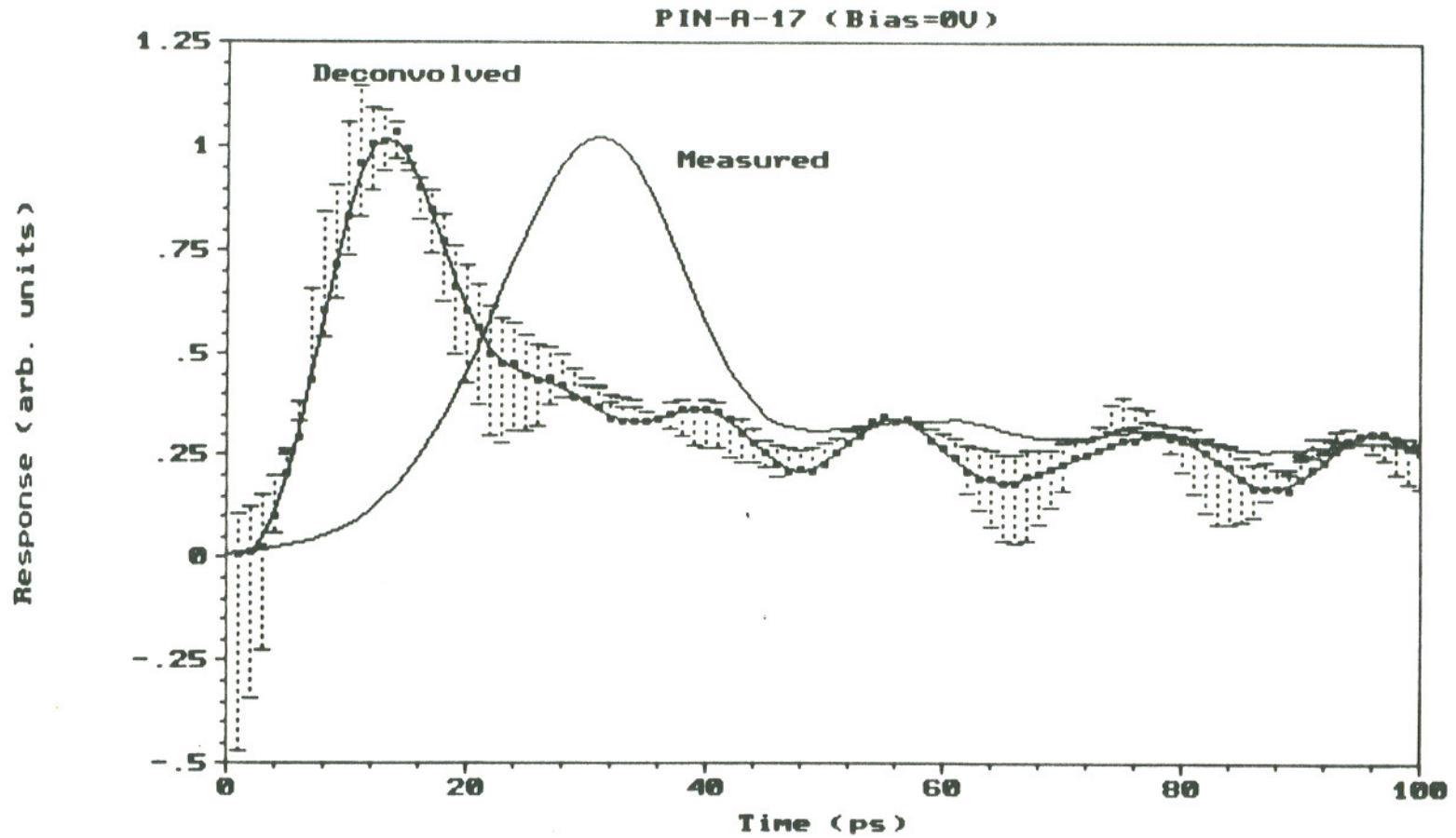


Figure 6.19. Measured and deconvolved response of PIN-A-17 at 0V applied. The measured response is given by the solid line. The deconvolved data is plotted as (■) with the moving average of the points plotted as the line passing through the points. The error bars are obtained by plotting the deconvolved data using the two measured step response of the measurement setup as the upper and lower limits.

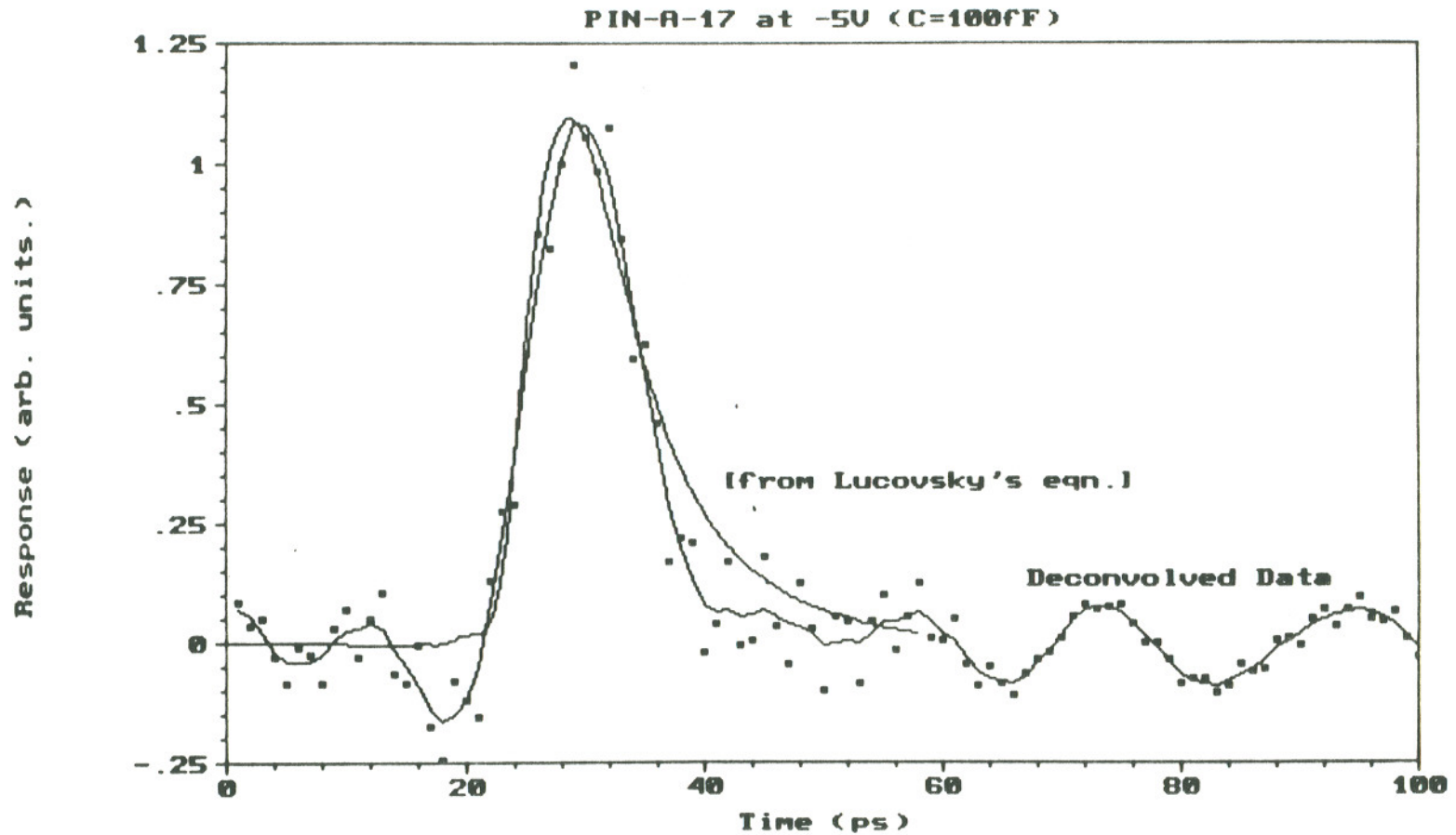


Figure 6.20. Calculated photoresponse of PIN-A-17 at -5V bias to the laser pulse source with 3.8ps FWHM. The deconvolved data plotted as (■) where the moving average is the solid line passing through the points. The response calculated from the transit time and RC time constant considerations is also plotted.

measured and calculated response is mainly due to the assumption of constant electric field and drift velocities in the InGaAs layer. The band calculations of the device as well as the carrier transport simulations indicate that these assumptions are not easily justified at these time scales and electric field strength. The two main reasons for this is the high intervalley scattering in these materials, and accumulation of carriers on the InGaAs side of both the heterojunctions.

A detailed calculation of the photoresponse of these devices should include the intervalley scattering which significantly affects the distribution of the electrons between the energy bands. The occupancy of the three electron bands obtained from the carrier transport simulations is plotted in figure 6.21. The program used in these simulations is a molecular dynamics calculation coupled with Ensemble Monte Carlo (EMC) technique developed by R.P. Joshi et.al. [97]. The calculations indicate that more than 50% of the electrons are transferred to the L valley within the time frame of the measurement. Although an average drift velocity can be used to obtain first order approximations, the implications of the occupancy of the L valley in terms of trapping of the electrons at the heterointerface can only be correctly incorporated by solving the transport equations with the boundary conditions defined by the geometry of the actual device. The absence of any tail in the measured response of PIN-A-17 which has an undoped InP buffer layer at the isotype heterojunction is unexpected if only the transport of electrons in the Γ valley is considered. Device calculations in InGaAs/InP

material system have to incorporate both the valleys in the equations. Work is in progress to simulate the carrier transport in these devices, with the actual device geometry and considering both electrons and holes.

6.6 Conclusion

Front side illuminated InGaAs/InP PIN mesa photodiodes have been fabricated. The device response show no significant tail with deconvolved pulse FWHM of 9.5 ± 1 ps, hence the fabricated photodiodes are suitable for high-speed analog and digital applications. The incorporation of a 100nm thick undoped buffer layer at the isotype heterojunction improves the DC characteristics of the device. The discontinuity of the energy bands have to be considered taking into account both the Γ valley and the L valley for electrons due to high intervalley scattering in InGaAs. The constant drift velocity and constant electric field assumptions have to be used with caution in these time scales and high electric field values. In future work on modelling of these devices a detailed calculation based on the self-consistent solutions of the diode equations and the EMC carrier simulations will be used in studying the bias dependence of the photoresponse in the fabricated devices.

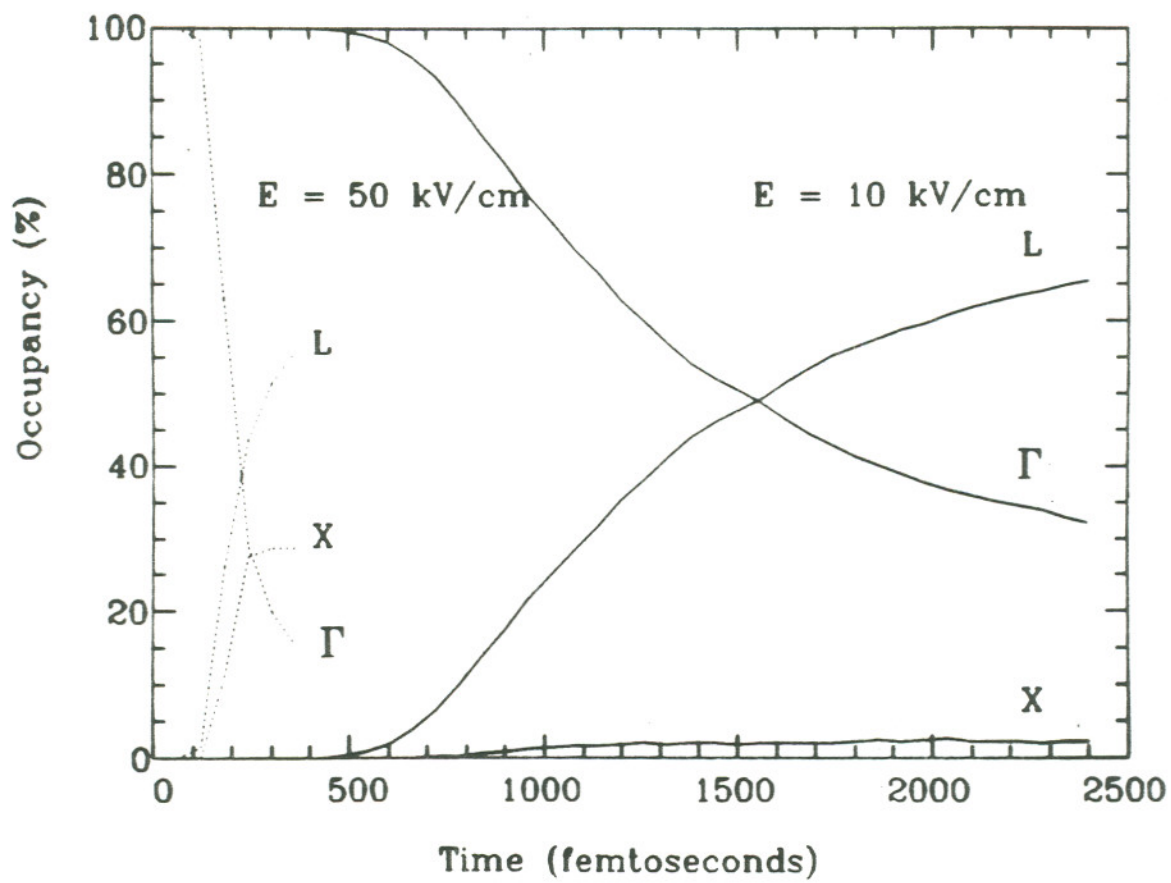


Figure 6.21. Occupancy factors of the conduction band valleys calculated by EMC simulations at an electric field value of 10kV/cm (solid lines), and 50kV/cm (dotted lines)

CHAPTER 7

CONCLUSION

The fabrication of advanced semiconductor devices based on new material systems require coordination of research in different fields of specializations. Each area of research offers unique challenges which require extensive effort in developing characterization techniques and theoretical models. The parameters related to material and device characterization and modelling are obtained based on the discussions generated in each field of research. The development of successful technologies in semiconductor device fabrication and integration depend on establishing the interrelation between the parameters that play significant role in different areas of the overall process. In this dissertation research various issues related to epilayer growth, material characterization, device fabrication, device characterization, and device modelling of InGaAs/InP PIN photodiodes have been studied. In this chapter, two issues that have played very important role in this project will be emphasized. The first one is the use of X-Ray Double Crystal Diffraction (XRDCD) in characterization of materials. The second one is the use of signal processing in analysis of the data and modelling of the device structure at various phases of fabrication.

XRDCD is a non-destructive characterization technique which can be used in various material related studies including ion implantation, lattice-matching in heterojunction devices, and determination of epilayer quality and composition in ternary alloy semiconductors. XRDCD is a valuable tool in technology development and it can be an integral part of the manufacturing process since neither sample preparation, nor vacuum is required for the analysis. However, it has not been established as an integral part of semiconductor research due to difficulties in quantitative analysis of the data. This difficulty is not an inherent part of the technique, and the development of user friendly simulation programs based on dynamical diffraction theory will enable this technique to be incorporated into semiconductor processing. We have used XRDCD rocking curve analysis in solving two major issues related to OMVPE growth. The first one is the determination of composition in $\text{In}_{1-x}\text{Ga}_x\text{As}$ to obtain lattice-matching to InP substrates. This issue has been widely studied and quantitative results are easily obtained. The second one is the determination of interface quality at the InGaAs/InP heterojunction. We were able to optimize gas switching procedure during OMVPE growth and eliminate the high density of defects originating from the top InP/InGaAs interface by qualitative analysis of the XRDCD measurements. This analysis was verified by cross sectional transmission electron microscopy. Once the correlation between the XRDCD measurement and the interface quality was established we were able to determine the quality of the epilayers non-destructively, before the photodiodes

were fabricated.

Simulation programs are already being widely used in the manufacturing and development of silicon based semiconductor devices. The integration of simulation programs into process development mainly depends on establishing strong correlation between the simulated results and actual structures. As the device dimensions are reduced and new material systems are introduced, the assumptions that have been acceptable previously require a critical examination. In the development of InGaAs/InP based integrated circuits two issues that are related electron transport offer a significant challenge in obtaining comprehensive device models. The first one is the effect of heterojunctions on the solution of the semiconductor equations. The second one is the effect of intervalley scattering on the drift velocity of electrons. Monte Carlo simulations of the electron transport have been extensively used in obtaining the drift velocity of the carriers as a function of electric field. In order to incorporate these results into the device models, the boundary conditions and the spatial dependence of the electric field imposed by the actual device geometry have to be used in the simulations. Hence an accurate calculation of the electric field as a function of position is the key issue in obtaining successful device models in heterojunction devices. The formulation of the diode equation in the five dimensional state-space has been discussed in detail in Chapters 4 and 5. The preliminary results are obtained at thermal equilibrium and the formulation is given for general case. Self-consistent solutions

obtained from the state equations for the general case will be an important step in deriving comprehensive device models that incorporate the band discontinuity at the heterojunctions. Although these solutions by themselves will be significant, the band structure and the electric field obtained from these equations have to be used in electron transport simulations (i.e. using Monte Carlo technique) in order to incorporate intervalley scattering at high electric field values. The results obtained in this manner will then have to be analyzed to obtain simplified analytical expressions that can be incorporated into the device models to be used in circuit simulation programs. The development of such circuit simulation programs will be the key issue in the design of complex integrated circuits based on III-V ternary alloys.

REFERENCES

- [1] M. Brain and T.P. Lee, "Optical Receivers for Lightwave Communication Systems," *J. Lightwave Tech.*, vol. LT-3, pp. 1281-1300, December 1985.
- [2] J.E. Bowers, C.A. Burrus, "Ultrawide-Band Long-Wavelength p-i-n Photodetectors," *J. Lightwave Tech.*, vol. LT-5, pp. 1339-1350, October 1987.
- [3] S. Kawanishi, A. Takada, and M. Saruwatari, "Wide-Band Frequency-Response Measurements of Optical Receivers Using Optical Heterodyne Detection," *J. Lightwave Tech.*, vol. 7, pp. 92-98, January 1989.
- [4] J.R. Hayes, A.R. Adams, and P.D. Greene, "Low-field Carrier Mobility," Chp. 8, in *GaInAsP Alloy Semiconductors*, T.P. Pearsall, Eds. NY:John Wiley & Sons 1982.
- [5] R. Van Tuyl, and C. Liechti, "High Speed Integrated Logic with GaAs MESFETs," *IEEE J. Solid State Cir.*, vol. SC-9, pp. 269-279, October 1974.
- [6] J.S. Blakemore, "Semiconducting and Other Major Properties of Gallium Arsenide," *J. Appl. Phys.*, vol. 53, pp. R123-R181, October 1982.
- [7] B.J. Van Zeghbroeck, W. Patrick, J. Halbout, and P. Vettiger, "105-GHz Bandwidth Metal-Semiconductor-Metal Photodiode," *IEEE Electron Device Lett.*, vol. 9, pp.527-529, October 1988.
- [8] M. Klingenstein, J. Kuhl, J. Rosenzweig, C. Moglestue, and A. Axmann, "Transit

- Time Limited Response of GaAs Metal-Semiconductor-Metal Photodiodes", *Appl. Phys. Lett.*, vol. 58, pp. 2503-2505, June 1991.
- [9] M. Ito, O. Wada, K. Nakai, and T. Sakurai, "Monolithic Integration of a Metal-Semiconductor-Metal photodetector and a GaAs preamplifier," *IEEE Electron Device Lett.*, vol. 23, pp. 220-222, 1987.
- [10] K. Kajiyama, Y. Mizushima, and S. Sakata, "Schottky Barrier Measurements on n-In_xGa_{1-x}As diodes," *Appl. Phys. Lett.*, vol. 23, pp. 458, 1973.
- [11] J. Selders, N. Emeis, and H. Beneking, "Schottky-Barriers on p-Type GaInAs," *IEEE Trans. Electron Devices*, vol. ED-32, pp. 605-609, March 1985.
- [12] N. Emeis, H. Schumacher, H. Beneking, "High-Speed GaInAs Schottky Photodetectors," *Electronics Lett.*, vol. 21, pp. 180, February 1985.
- [13] J.B.D. Soole, H. Schumacher, H.P. LeBlanc, R. Bhat, and M.A. Koza, "High-Frequency Performance of InGaAs Metal-Semiconductor-Metal Photodetectors at 1.55 and 1.3 μ m Wavelengths," *Appl. Phys. Lett.*, vol. 55, pp. 729-731, August 1989.
- [14] W.K. Chan, G. Chang, R. Bhat, N.E. Schlotter, and C.K. Nguyen, "High-Speed Ga_{0.47}In_{0.53}As MISIM Photodetectors with Dielectric-Assisted Schottky Barriers," *IEEE Electron Device Lett.*, vol. 10, pp. 417-419, September 1989.
- [15] T.J. Licata, M.T. Schmidt, R.M. Osgood Jr., W.K. Chan, and R. Bhat, "Application of Photodeposited Cd to Schottky Barrier Diode and Transistor Fabrication on InP and In_{0.53}Ga_{0.47}As Substrates," *Appl. Phys. Lett.*, vol. 58, pp. 845-847, February

1991.

[16] R.S. Tucker, A.J. Taylor, C.A. Burrus, G. Eisenstein, and J.M. Wiesenfield, "Coaxially Mounted 67GHz Bandwidth InGaAs PIN Photodiode," *Electr. Lett.*, vol. 22, pp. 917, August 1986.

[17] D.L. Crawford, Y.G. Wey, A. Mar, J.E. Bowers, M.J. Hafich, and G.Y. Robinson, "High Speed InGaAs-InP p-i-n Photodiodes Fabricated on a Semi-Insulating Substrate," *IEEE Photon. Tech. Lett.*, vol. 2, pp. 647-649, September 1990.

[18] Y.G. Wey, D.L. Crawford, K. Giboney, J.E. Bowers, and M.J. Rodwell, P. Silverstre, M.J. Hafich, and G.Y. Robinson, "Ultrafast Graded Double-Heterostructure GaInAs/InP Photodiode," *Appl. Phys. Lett.*, vol. 58, pp. 2156-2158, May 1991.

[19] Y.K. Chen, R.N. Nottenburg, M.B. Panish, R.A. Hamm, and D.A. Humprey, "Subpicosecond InP/InGaAs Heterostructure Bipolar Transistor," *IEEE Electron Dev. Lett.*, vol. 10, pp. 267-269, 1989.

[20] U.K. Mishra, A.S. Brown, S.E. Rosenbaum, C.E. Hooper, M.W. Pierce, M.J. Delaney, S. Vaughn, and K. White, "Microwave Performance of AlInAs-GaInAs HEMT's with 0.2- and 0.1- μm Gate Length", *IEEE Electron Dev. Lett.*, vol. 9, pp. 647-649, 1988.

[21] K.H.G. Duh, P.C. Chao, S.M.J. Liu, P. Ho, M.Y. Kao, and J.M. Ballingall, "A Super Low-Noise 0.1 μm T-Gate InAlAs-InGaAs-InP HEMT", *IEEE Microwave Guided Wave Lett.*, vol. 1, pp. 114-116, May 1991.

- [22] M. Halliwell, "Characterization of Structures Grown By MOVPE Using X-Ray Diffraction," *Prog. Crystal Growth and Charact.*, vol. 19, pp. 249-257, 1989.
- [23] B.K. Tanner and M.J. Hill, "Double Axis X-Ray Diffractometry at Glancing Angles," *J. Phys. D: Appl. Phys.*, vol. 19, pp. L229-L235, 1986.
- [24] C. Ferrari and P. Franzosi, "Investigation of the Interface Grading in III-V Heterostructures by Double-Crystal Diffractometry," *J. Appl. Phys.*, vol. 65, pp. 1544-1549, 1989.
- [25] A.T. Macrander, S.N.G. Chu, K.E. Strege, A.F. Bloemeke, and W.D. Johnston Jr., "Correlation Between Background Carrier Concentration and X-Ray Linewidth for InGaAs/InP Grown by Vapor Phase Epitaxy," *Appl. Phys. Lett.*, vol. 44, pp. 615-617, 1984,
- [26] S. Takagi, "A Dynamical Theory of Diffraction for a Distorted Crystal," *J. Phys. Soc. Japan.*, vol. 26, pp. 1239-1253, 1969.
- [27] A.W. Nelson, P.C. Spurdens, S. Cole, R.H. Moss, S. Wong, M.J. Harding, D.M. Cooper, W.J. Devlin and M.J. Robertson, "The Role of MOVPE in the Manufacture of High Performance InP Based Optoelectronic Devices," *J. Cryst. Growth*, vol. 93, pp. 792-802, 1988.
- [28] R.D. Dupuis, J.C. Campbell and J.R. Velebir, "InGaAs/InP Photodiodes Grown By Metalorganic Chemical Vapor Deposition," *J. Cryst. Growth*, vol. 77, pp. 598-605, 1986.

- [29] M.D. Scott, A.G. Norman and R.R. Bradley, "The Characterization of $\text{Ga}_{1-x}\text{In}_x\text{As}$, $\text{Al}_{1-x}\text{In}_x\text{As}$ and InP Epitaxial Layers Prepared by Metal Organic Chemical Vapour Deposition," *J. Cryst. Growth*, vol. 68, pp. 319-325, 1984.
- [30] S.J. Bass and M.L. Young, "High Quality Epitaxial Indium Phosphide and Indium Alloys Grown Using Trimethylindium and Phosphine in an Atmospheric Pressure Reactor," *J. Cryst. Growth*, vol. 68, pp. 311-318, 1984.
- [31] S.J. Bass, S.J. Barnett, G.T. Brown, N.G. Chew, A.G. Cullis, A.D. Pitt and M.S. Skolnick, "Effect of Growth Temperature on the Optical, Electrical and Crystallographic Properties of Epitaxial Indium Gallium Arsenide Grown by MOCVD in an Atmospheric Pressure Reactor," *J. Cryst. Growth*, vol. 79, pp. 378-385, 1986.
- [32] M. Kamada and H. Ishikawa, "Effects of V/III Ratio on Electronic and Optical Properties of GaInAs Layers Grown by MOCVD," *J. Cryst. Growth*, vol. 94, pp. 849-856, 1989.
- [33] J. Matsui, K. Onabe, T. Kamejima and I. Hayashi, "Lattice Mismatch Study of LPE-Grown InGaPAs on (100)-InP Using X-Ray Double-Crystal Diffraction", *J. Electrochem. Soc.*, vol. 126, pp. 664-667, 1979.
- [34] W.J. Bartels, "Characterization of Thin Layers on Perfect Crystals with a Multipurpose High Resolution X-Ray Diffractometer," *J. Vac. Sci. Technol. B*, vol. 1, pp. 338-345, 1983.
- [35] R.E. Nahory, M.A. Pollack, W.D. Johnston, Jr. and R.L. Barns, "Band gap versus

- composition and Demonstration of Vegard's Law for $\text{In}_{1-x}\text{Ga}_x\text{As}_y\text{P}_{1-y}$ Lattice Matched to InP," *Appl. Phys. Lett.*, vol. 33, pp. 659-661, 1978.
- [36] G.B. Stringfellow, "A Critical Appraisal of Growth Mechanisms in MOVPE," *J. Cryst. Growth*, vol. 68, pp. 111-122, 1984.
- [37] A. Koukitsu and H. Seki, "Thermodynamic Analysis of the MOVPE Growth of Quaternary III-V Alloy Semiconductors," *J. Cryst. Growth*, vol. 76, pp. 233-242, 1986.
- [38] P.D. Agnello and S.K. Ghandhi, "The Composition Dependence of GaInAs Grown by Organometallic Epitaxy," *J. Cryst. Growth*, vol. 97, pp. 551-559, 1989.
- [39] J.C. McClellan, "Parametric Signal Modelling," Chp. 1, in *Advanced Topics in Signal Processing*, eds. J.S. Lim and A.V. Oppenheim, Prentice Hall, NJ 1988.
- [40] J.S. Whiteley and S.K. Ghandhi, "Growth and Characterization of $\text{Ga}_{0.47}\text{In}_{0.53}\text{As}$ Films on InP Substrates Using Triethylgallium, Triethylindium, and Arsine," *J. Electrochem. Soc.*, vol. 130, pp. 1191-1195, 1983.
- [41] K.L. Hess, D.L. Kasemset and P.D. Dapkus, "Growth and Characterization of $\text{Ga}_{1-x}\text{In}_x\text{As}$ by Low Pressure Metalorganic Chemical Vapor Deposition," *J. Electr. Mat.*, vol. 13, pp. 779-798, 1984.
- [42] L. Makowski and M. Glicksman, "Disorder Scattering in Solid Solutions of III-V Semiconducting Compounds," *J. Phys. Chem. Sol.*, vol. 34, pp. 487-492, 1973.
- [43] M. Glicksman, R.E. Enstrom, S.A. Mittleman and J.R. Appert, "Electron

- Mobility in $\text{In}_x\text{Ga}_{1-x}\text{As}$ Alloys," *Phys. Rev. B*, vol. 9, pp. 1621-1626, 1974.
- [44] D.L. Rode, "Low-Field Electron Transport," Chp. 1, in *Semiconductors and Semimetals*, Vol. 10, eds. R.K. Willardson and A.C. Beer, Academic Press, 1975.
- [45] W. Fawcett, A.D. Boardman and S Swain, "Monte Carlo Determination of Electron Transport Properties in Gallium Arsenide," *J. Phys Chem. Solids*, vol. 31, pp. 1963-1990, 1970.
- [46] M.A. Littlejohn, J.R. Hauser and T.H. Glisson, "Velocity-Field Characteristics of $\text{Ga}_{1-x}\text{In}_x\text{P}_{1-y}\text{As}_y$ Quaternary Alloys," *Appl. Phys. Lett.*, vol. 30, pp. 242-244, 1977.
- [47] M.A. Littlejohn, J.R. Hauser, T.H. Glisson, D.K. Ferry and J.W. Harrison, "Alloy Scattering and High Field Transport in Ternary and Quaternary III-V Semiconductors," *Solid-State Electron.*, vol. 21, p. 107-114, 1978.
- [48] H. Ehrenreich, "Screening Effects in Polar Semiconductors," *J. Phys. Chem. Solids*, vol. 8, pp. 130-135, 1959.
- [49] A. Fortini, D. Diguët and J. Lugand, "Analysis of Polar Optical Scattering of Electrons in GaAs," *J. Appl. Phys.*, vol. 41, pp. 3121-3127, 1970.
- [50] H. Brooks, Chp. 3, in *Adv. Electron. Electron Physics*, Vol. 7, pp. 85, 1955.
- [51] L.R. Weisberg, "Anomalous Mobility Effects in Some Semiconductors and Insulators," *J. Appl. Phys.*, vol. 33, pp. 1812-1817, 1962.
- [52] J.D. Zook, "Piezoelectric Scattering in Semiconductors," *Phys. Rev. A*, vol. 136, pp. A869-A878, 1964.

- [53] J. Bardeen and W. Shockley, "Deformation Potentials and Mobilities in Non-Polar Crystals," *Phys. Rev.*, vol. 80, pp. 72-80, 1950.
- [54] C. Erginsoy, "Neutral Impurity Scattering," *Phys. Rev.*, vol. 79, pp. 1013-1014, 1950.
- [55] R.J. Nicholas, J.C. Portal, C. Houlbert, P. Perrier and T.P. Pearsall, "An Experimental Determination of the Effective Masses for $\text{Ga}_x\text{In}_{1-x}\text{As}_y\text{P}_{1-y}$ Alloys Grown on InP," *Appl. Phys. Lett.*, vol. 34, pp. 492-494, 1979.
- [56] J.S. Blakemore, "Solid State Physics," Cambridge University Press, 2nd. Edition, NY 1985.
- [57] K. Eguchi, M. Kushibe, M. Funamizu and Y. Ohba, "Interfacial Charge and Its Effects on Mobility and Carrier Concentration for High-Purity GaInAs Grown by Metalorganic Chemical Vapor Deposition," *Jpn. J. Appl. Phys.*, vol. 29, pp. 1431-1434, 1990.
- [58] M.R. Pinto, C.S. Rafferty, H.R. Yeager, and R.W. Dutton, *PISCES-II Technical Report*, Stanford, 1984.
- [59] D.L. Scharfetter and H.K. Gummel, "Large-Signal Analysis of a Silicon Read Diode Oscillator," *IEEE Trans. Electr. Devices*, vol. ED-16, pp. 64-77, 1969.
- [60] D.L. Heald, P.F. Ordnung, J.G. Skalnik and E.N. Nansen, "Thermodynamic Considerations of p-n Junction Capacitance," *Solid-State Electron.*, vol. 16, pp. 1055-1065, 1973.

- [61] H.K. Gummel and D.L. Scharfetter, "Depletion-Layer Capacitance of p^+n Step Junctions," *J. Appl. Phys.*, vol. 38, pp. 2148-2153, 1967.
- [62] B.R. Chawla and H.K. Gummel, "Transition Region Capacitance of Diffused p-n Junctions," *IEEE Trans. Electr. Devices*, vol. ED-18, pp. 178-195, 1971.
- [63] R.C. Jaeger and F.H. Gaensslen, "Simulation of Impurity Freezeout Through Numerical Solution of Poisson's Equation with Application to MOS Device Behavior," *IEEE Trans. Electr. Devices*, vol. ED-27, pp. 914-920, 1980.
- [64] J.S. Blakemore, "Approximations for the Fermi-Dirac Integrals," *Solid-St. Electron.*, vol. 25, pp. 1067-1076, 1982.
- [65] W. Shockley, "The Theory of p-n Junctions in Semiconductors and p-n Junction Transistors," *Bell System Tech. J.*, vol. 28, pp. 435-489, 1949.
- [66] W. Shockley, "Electrons and Holes in Semiconductors", D. Van Nostrand, Princeton, N.J. 1950.
- [67] S.M. Sze, "Physics of Semiconductor Devices", 2nd. ed., John Wiley & Sons, New York 1981.
- [68] J.S. Blakemore, "Semiconductor Statistics", Dover Edition, New York 1987, [Orig. ed. Pergamon Press, 1962]
- [69] J.D. Jackson, "Classical Electrodynamics", John Wiley & Sons, New York 1962.
- [70] J.W. Slotboom, "The pn-Product in Silicon," *Solid-State Electron*, vol. 20, pp. 279-283, 1977.

- [71] W. Shockley and W.T. Read, "Statistics of the Recombination of Holes and Electrons," *Phys Rev.*, vol. 87, pp. 835-842, 1952; R.N. Hall *Phys Rev.*, vol. 87, p. 387, 1952.
- [72] J.S. Lim and A.V. Oppenheim, "Advanced Topics in Signal Processing", Prentice Hall, New York 1988.
- [73] G.H. Golub, and C. Reinsch, "Singular Value Decomposition and Least Squares Solutions", in *Handbook for Automatic Computation, vol. II*, J.H. Wilkinson and C. Reinsch (editors), Heidelberg: Springer 1971.
- [74] T. Kailath, "Linear Systems", Prentice-Hall, New York 1980.
- [75] L.O. Chua and P.M. Lin, "Computer Aided Analysis of Electronic Circuits", Prentice-Hall, New York 1975.
- [76] L.A. Zadeh and C.A. Desoer, "Linear Systems Theory- A State Space Approach", McGraw Hill, New York, 1967.
- [77] Y. Istefanopulos, "State Variables and Linear Control Systems", Bogazici Univ. Publ., Istanbul, Turkey 1981.
- [78] L.F. Shampine, H.A. Watts, DEPAC-Design of User Oriented Package of ODE Solvers, SAND79-2374, Sandia Laboratories, 1979.
- [79] K. Yokoyama, M. Tomizawa, H. Kanbe, and T. Sudo, "A Numerical Analysis of a Heterostructure InP/InGaAs Photodiode," *IEEE Trans. Electron Devices*, vol. ED-30, pp. 1283-1288, 1983.

- [80] C.D. Lee and S.R. Forrest, "Effects of Lattice Mismatch on $\text{In}_x\text{Ga}_{1-x}\text{As}$ heterojunctions," *Appl. Phys. Lett.*, vol. 57, pp. 469-471, July 1990.
- [81] C. de Boor, "A Practical Guide to Splines", Springer-Verlag, NY 1978.
- [82] J.M. Mendel, "Lessons in Digital Estimation Theory," Prentice-Hall, NJ 1987.
- [83] S. Haykin, "Adaptive Filter Theory", 2nd edition, Prentice-Hall, NJ 1991.
- [84] S. Tabor, MS. Thesis, Portland State University 1991.
- [85] A. Takada, T. Sugie, and M. Saruwatari, "High-Speed Picosecond Optical Pulse Compression from Gain-Switched 1.3 μm Distributed Feedback-Laser Diode (DFB-LD) through Highly Dispersive Single-Mode Fiber," *J. Lightwave Tech.*, vol. LT-5, pp. 1525-1533, October 1987.
- [86] R.T. Hawkins II, M.D. Jones, S.H. Pepper, and J.H. Goll, "Comparison of Fast Photodetector Response Measurements by Optical heterodyne and Pulse Response Techniques," *J. Lightwave Tech.*, vol. LT-9, pp. 1289-1294, October 1991.
- [87] M. Ravel, (Personal Correspondence)
- [88] D.E. Aspnes and H.J. Stocker, "Peroxide Etch Chemistry on $\langle 100 \rangle$ InGaAs," *J. Vac. Sci. Technol.*, vol. 21, pp. 413-416, July 1982.
- [89] H.L. VanNice, D. Jones, T. Dosluoglu, and R.Solanki, "Surface Chemistry of $\text{In}_{0.53}\text{Ga}_{0.47}\text{As}/\text{InP}$ Materials," (unpublished)
- [90] A.W. Nelson, and L.D. Westbrook, "A Study of p-type Dopants For InP Grown by Adduct MOVPE," *J. Cryst. Growth*, vol. 68, pp. 102-110, 1984.

- [91] G. Lucovsky, R.F. Schwarz, and R.B. Emmons, "Transit-Time Considerations in p-i-n Diodes," *J. Appl. Phys.*, vol. 35, pp. 622-628, 1964.
- [92] J.W. Lee and D.M. Kim, "Analytical Time Domain Characterization of p-i-n Photodiodes: Effects of Drift, Diffusion, Recombination, and Absorption," (Personal correspondence, to be published in *J. Appl. Phys.*)
- [93] J.A. Valdmanis and G. Mourou, "Subpicosecond Electrooptic Sampling: Principles and Applications," *IEEE J. Quantum Electron.*, vol. QE-22, pp. 69-78, January 1986.
- [94] B.H. Kolner and D. Bloom, "Electrooptic Sampling in GaAs Integrated Circuits," *IEEE J. Quantum Electron.*, vol. QE-22, pp. 79-93, January 1986.
- [95] J.M. Mendel, "Optimal Seismic Deconvolution: an Estimation Based Approach", Academic Press, NY 1983.
- [96] L.L. Scharf, "The SVD and Reduced-Rank Signal Processing", in *SVD and Signal Processing, II*, ed. R. Vaccaro, Elsevier Sci. Pub., NY 1991.
- [97] R.P. Joshi and D.K. Ferry, "Effect of Multi-ion Screening on the Electron Transport in Doped Semiconductors: A Molecular-Dynamics Analysis," *Phys. Rev. B.*, vol 43, pp. 9734-9739, April 1991.

VITA

The author was born on May 11, 1965 in Ankara, Turkey. He graduated from Ankara Fen Lisesi in 1983 and enrolled in Department of Electrical Engineering at Bogazici University. He received his B.S. degree in Electrical Engineering and B.S. degree in Physics in 1987.

The author came to Oregon Graduate Institute in 1987 and completed all requirements for the Doctor of Philosophy degree in Electrical Engineering in February 1992. During the course of study he has received Tektronix fellowship support. He is leaving to accept a position of process engineer at Tektronix, Inc.

The author has contributed to the following scientific publications:

- [1] T. Dosluoglu and R. Solanki, "Self-consistent Calculations of Carrier Distribution and Energy Bands in InGaAs/InP PIN Diodes," submitted to *Appl. Phys. Lett.*.
- [2] T. Dosluoglu, R. Gudimetla, and R. Solanki, "The Generalized Steady State Diode Equation: The State Equations Approach," submitted to *Solid-State Electronics*.
- [3] T. Dosluoglu and R. Solanki, "The Effect of InP Buffer Layer on the Electron Transport Properties of Epitaxial $\text{In}_{1-x}\text{Ga}_x\text{As}$," *J. Appl. Phys.*, 69, 7327 (1991)
- [4] T. Dosluoglu, U. Sudarsan, and R. Solanki, "Relationship Between Gas Flows and Film Composition in Organometallic Vapor Phase Epitaxy of $\text{In}_{1-x}\text{Ga}_x\text{As}$," *J. Cryst. Growth*, 106, 643 (1990)

- [5] D.M. Kim, T. Dosluoglu, D.E. Whitlow and F. Qian, "Characterization and Simulation of Polysilicon TFT-CMOS for HDTV Display Applications," in Proceedings of International Symposium on Circuits and Systems (ISCAS), Singapore, June 1991.
- [6] U. Sudarsan, T. Dosluoglu, N.W. Cody, and R. Solanki "Selective Heteroepitaxy of GaP on Silicon" *J. Cryst. Growth*, 94, 978 (1989)
- [7] U. Sudarsan, T. Dosluoglu, N.W. Cody, and R. Solanki "Argon Ion and Excimer Laser Induced Epitaxy of GaP," in Laser and Particle Beam Chemical Processes, eds. A.W. Johnson, T.W. Sigmon, and G.L. Loper (North Holland, New York)
- [8] U. Sudarsan, N.W. Cody, T. Dosluoglu, and R. Solanki "Ultraviolet Laser-Induced Low Temperature Epitaxy of GaP," *Appl. Phys. Lett.*, 55, 738 (1989)
- [9] U. Sudarsan, N.W. Cody, T. Dosluoglu, and R. Solanki "Low Temperature Photon-Assisted Epitaxy of III-V Semiconductors," *Appl. Phys. A*, 50, 325 (1990)